## Title
Analysis of complex graded-dielectric structures for dispersion compensation in high frequency signal propagation in microstrip circuits



**Author**
DiBene II, Joseph Theodore

**Publication Date**
2006

Peer reviewed|Thesis/dissertation

UNIVERSITY OF CALIFORNIA, SAN DIEGO

# Analysis of Complex Graded-Dielectric Structures for Dispersion Compensation in High Frequency Signal Propagation in Microstrip Circuits

A dissertation submitted in partial satisfaction of the
requirements for the degree
Doctor of Philosophy

in

Electrical Engineering (Applied Physics)

by

Joseph Theodore DiBene II

Committee in charge:

Professor Kevin B. Quest, Chair
Professor Costas Pozrikidis
Professor Barnaby Rickett
Professor Robert E. Skelton
Professor Paul Yu

2006

The dissertation of Joseph Theodore DiBene II is approved, and it is acceptable in quality and form for publication on microfilm:

Chair

University of California, San Diego

2006

To My Wife and Son

*If a man does not keep pace with his companions, perhaps it is because he hears a different drummer. Let him step to the music which he hears, however measured or far away.*

—Thoreau

TABLE OF CONTENTS

LIST OF FIGURES

LIST OF TABLES

## ACKNOWLEDGEMENTS

I have been extremely fortunate and honored by the help and support of many people, to whom I owe far more gratitude than I can possibly express here. I could not begin to name all of those who have helped me over the years but my thanks to you all nonetheless. This thesis began as a simple idea which I expressed to my now thesis advisor Dr. Kevin Quest who thankfully encouraged me to pursue it to its conclusion. Without his support and direction over these many years I could never have completed this journey. And of course to my advisory committee for their time and brilliance. To the people who believed in me and helped me to start this journey. Dr. Lothar (Bud) Hoeft, Dr. James L. Drewniak, Dr. Clayton R. Paul, and Dr. Keith P. Muller. A very special thanks to my good friend and mentor Dr. James L. Knighten whom tolerated me over these many years. And to my *other* mentor David H. Hartke to whom I have learned so much from. To Joseph S. Riel my good friend for teaching me to persevere. Of course, this all would not be possible without the support of my family. To my mother and father for being there. But most of all, I want to thank my wife and son for their incredible tolerance and love which has allowed me to continue when I honestly thought at times I could not. It is for them that this thesis is mostly dedicated to. Your gift of patience has been my salvation. Thank you.

# VITA

| | |
|---|---|
| 1960 | Born, San Jose, California |
| 1975-1982 | Journeyman Machinist, Santa Barbara, CA |
| 1984 | Associates Degree, Santa Barbara City College |
| 1986 | Motor Repair Technician, Buena Tool Corporation, Santa Barbara, CA |
| 1988 | B.S. Electrical Engineering University of California, Santa Barbara, CA |
| 1988-1998 | System Architect and Design Engineer, NCR Corporation, San Diego, CA |
| 2002 | M.S. Electrical Engineering University of California San Diego |
| 1998-2004 | Chief Technology Officer, INCEP Technologies, San Diego, CA |
| 2004-present | Principal Engineer and Senior Silicon Architect, Intel Corporation, Dupont, WA |
| 2006 | Ph. D., Electrical Engineering University of California San Diego |

# PUBLICATIONS

*Analysis of Dispersion Control Method for Ultra High Speed Transmission Lines for Digital Communications*, J. T. DiBene II, K. B. Quest, and J. L. Knighten, To appear in 2006 IEEE Electromagnetic Compatibility Symposium

*Limitations in Ultra-High Speed Serial Communications 20 Gb/s and Beyond - Across Common PWB Microstrip Circuits*, J. T. DiBene II, K. B. Quest, and J. L. Knighten, IMAPs Advanced Technology Workshop on High Speed Interconnects, October 2004

*Common-Mode Current Harmonics on Differential Pair Cable Shields Operating in a Regime as High as 2.125 Gb/s*, J. L. Knighten, N. W. Smith, J. T. DiBene II, and L. O. Hoeft, 2001 IEEE Symposium on Electromagnetic Compatibility, Montreal, Canada, August 2001

*Dependence of EMI Common-Mode Current Currents on Delay Skew Imbalance in High Speed Differential Transmission Lines*, J. L. Knighten, N. W. Smith, J. T. DiBene II, and L. O. Hoeft, 2nd Annual IMAPS Advanced Technical Workshop, Austin, TX, January, 2000

*EMI Common-Mode Current Current Dependence on Delay Skew Imbalance in High Speed Differential Pair Transmission Lines Operating at 1 Gigabit/second Data Rates*, J. L. Knighten, N. W. Smith, J. T. DiBene II, and L. O. Hoeft, 2000 International Symposium on Quality Electronic Design, San Jose, CA, March 2000

*Discrete Wire Technology for High Speed Circuits*, J. T. DiBene II, A. Orlandi, and E. Stefanko, and L. O. Hoeft, Compliance Engineering Magazine

*Experimental Analysis of Common-Mode Currents on Fibre Channel Cable Shields due to Skew Imbalance of Differential Signals Operating at 1.0625 Gb/s*, J. L. Knighten, N. W. Smith, J. T. DiBene II, and L. O. Hoeft, 1999 IEEE International Symposium on Electromagnetic Compatibility, Seattle, WA, August 1999, pp. 195-200

*Signal Induced EMI in Fibre Channel Cable-Connector Assemblies*, J. L. Knighten, N. W. Smith, J. T. DiBene II, and L. O. Hoeft, 1999 IEEE International Symposium on Electromagnetic Compatibility, Seattle, WA, August 1999, pp. 201-205

*Vent Design Optimization to Meet Cooling and EMI Requirements*, D. G. Wang, J. T. DiBene II, P. K. Muller, and J. L. Knighten, 1999 International Systems Packaging Symposium, San Diego, CA, January 1999, pp. 24-29

*Charge Density Distributions and Associated Potential Distribution on a Shielded Twisted Four-Wire Transmission Line*, C. James and J. T. DiBene II, 1998 IEEE International Symposium on Electromagnetic Compatibility, Denver, CO, August 1998, pp. 1156-1160

*Spectral Analysis of Common-Mode Currents on Fibre-Channel Shields due to Skew Imbalance of Differential Signals Operating at 1.0625 Gb/s*, L. O. Hoeft, J. L. Knighten, J. T. DiBene II, and M. W. Fogg, 1998 IEEE International Symposium on Electromagnetic Compatibility, Denver, CO, August 1998, pp. 527-531

*Intelligent Fault Tolerant, High Power Distributed Power System for Massive Parallel Processing Computers*, J. Burns, J. Riel, and J. T. DiBene II APEC IEEE 1994 Proceedings

*Integrating Engineering and Manufacturing*, J. T. DiBene II and M. Robinson, 1991 NCR Journal, Vol. 5, No. 2 APEC

## CONFERENCE PRESENTATIONS

*Fundamentals in Signal Integrity - Introduction to I/O Structures*, J. T. DiBene II, J. L. Drewniak, and G. Sele, Tutorial - to be given at - 2006 IEEE International Symposium on Electromagnetic Compatibility, Portland OR, August 2006

*Fundamentals in Signal Integrity - SPICE Modeling for High Speed Applications*, J. T. DiBene II, J. L. Drewniak, and G. Sele, Tutorial - to be given at - 2006 IEEE International Symposium on Electromagnetic Compatibility, Portland OR, August 2006

*Fundamentals in Signal Integrity - IBIS Modeling*, G. Sele, J. T. DiBene II, and J. L. Drewniak, Tutorial - to be given at - 2006 IEEE International Symposium on Electromagnetic Compatibility, Portland OR, August 2006

*Fundamentals in Signal Integrity - SPICE and IBIS Modeling*, J. T. DiBene II, J. L. Drewniak, and G. Sele, Tutorial - 2005 IEEE International Symposium on Electromagnetic Compatibility, Chicago IL, August 2005

*Fundamentals in Signal Integrity - SPICE and IBIS Modeling*, J. T. DiBene II, J. L. Drewniak, and G. Sele, Tutorial - 2004 IEEE International Symposium on Electromagnetic Compatibility, Santa Clara CA, August 2004

*Server Power System Trends, Architecture, Technologies, and Issues for Advanced Computing Systems Moving Towards 2010*, J. T. DiBene II and T. V. Aldridge IMAP's Advanced Technology Workshop on High Speed Interconnect, EMC and Power Aspects of System Packaging for High Performance Computing, Telecom and Semiconductor Capital Equipment, October 2004

*High Performance, Low Inductance Interconnects*, J. T. DiBene II, APEC Miami FL, February 2003

*High Performance, Low Inductance Interconnects - Part II*, D. Wood and J. T. DiBene II, APEC Miami FL, February 2003

*No Title*, D. Wood and J. T. DiBene II, Fall IBM Power Systems Conference, Minneapolis MN, September 2002

*Power and Thermal Solutions for High Density McKinley System Packaging*, J. T. DiBene II, Fall 2001 Intel Developers Forum, August 2001

*System Interconnection and Power Delivery - Server Track*, J. T. DiBene II, Spring 2001 Intel Developers Forum, February 2001

*Fundamentals in Signal Integrity and EMC for High Speed Cable Modeling*, J. T. DiBene II, Seminar @ Tensolite Corporation, St. Augustine FL, August 1997

PATENTS

*Method and apparatus for providing power to a microprocessor with integrated thermal and EMI management*, J. T. DiBene II and D. H. Hartke, US Patent #6,947,293 September, 2005

*Ultra-low impedance power interconnection system for electronic packages*, J. T. DiBene II, D. H. Hartke, C. E. Hoge, and E. Derian, US Patent #6,847,529 January, 2005

*Right-angle power interconnect electronic package assembly*,D. H. Hartke and J. T. DiBene II, US Patent #6,845,013 January, 2005

*Integrated power delivery and cooling system for high power microprocessors*,D. H. Hartke, J. T. DiBene II, E. Derian, and J. M. Broder, US Patent #6,801,431 October, 2004

*Integrated magnetic buck converter with magnetically coupled synchronously rectified MOSFET gate drive*, P. Harris and J. T. DiBene II, US Patent #6,754,086 June, 2004

*Integrated power delivery and flex circuit interconnection for high density power circuits for integrated circuits and systems*, D. H. Hartke and J. T. DiBene II, US Patent #6,741,480 May, 2004

*Vortex heatsink for low pressure drop and high heat flux and power integrated circuits and systems*, J. T. DiBene II and F. Raizadeh, US Patent #6,698,511 March, 2004

*Separable power delivery connector*, E. Derian, J. T. DiBene II, and D. H. Hartke, US Patent #6,623,279 September, 2003

*Apparatus for delivering power to high performance electronic assemblies*, J. T. DiBene II, D. H. Hartke, C. E. Hoge, E. Derian, J. M. Broder, J. Br. San Andres, and J.S. Riel, US Patent #6,618,218 September, 2003

*High speed and density circular pin connector for board-to-board interconnection systems*, J. T. DiBene II, US Patent #6,609,914 August, 2003

*Ultra-low impedance power interconnection system for electronic packages*, J. T. DiBene II, D. H. Hartke, C. E. Hoge, and E. Derian, US Patent #6,556,455 April, 2003

*Vapor chamber with integrated pin array*, J. T. DiBene II and F. Raizadeh, US Patent #6,490,160 December, 2002

*Method and apparatus for thermal and mechanical management of a power regulator module and microprocessor in contact with a thermally conducting plate*, J. T. DiBene II and D. H. Hartke, US Patent #6,452,804 September, 2002

*Method and apparatus for providing power to a microprocessor with integrated thermal and EMI management*, J. T. DiBene II, D. H. Hartke, J. H. Kaskade, and C. E. Hoge, US Patent #6,452,113 September, 2002

*Imbedded die-scale interconnect for ultra-high speed digital communications*, J. T. DiBene II, P. K. Muller, and I. M. Robinson, US Patent #6,429,386 August, 2002

*Integrated venting, EMI shield and heatsink component for electronic equipment enclosures*, G. Wang, P. K. Muller, J. K. Knighten, and J. T. DiBene II, US Patent #6,401,805 June, 2002

*Inter-circuit encapsulated packaging for power delivery*, J. T. DiBene II and D. H. Hartke, US Patent #6,356,448 March, 2002

*Inter-circuit encapsulated packaging*, J. T. DiBene II and D. H. Hartke, US Patent #6,304,450 October, 2001

*Centralized cooling interconnect for electronic packages*, J. T. DiBene II, G. Wang, and P. K. Muller, US Patent #6,243,269 June, 2001

*Imbedded PCB AC coupling capacitors for high data rate signal transfer*, J. T. DiBene II, US Patent #5,972,231 October, 1999

*ECL pulse amplitude modulated encoder driver circuit*, D. H. Hartke and J. T. DiBene II, US Patent #5,969,579 October, 1999

*High pressure jackscrew connector*, J. T. DiBene II, US Patent #5,785,449 July, 1998

*Cable connector locking arrangement*, J. T. DiBene II, W. F. Roosa, and W. W. Porter, US Patent #5,044,975 September, 1991

ABSTRACT OF THE DISSERTATION

**Analysis of Complex Graded-Dielectric Structures for Dispersion Compensation in High Frequency Signal Propagation in Microstrip Circuits**


by

Joseph Theodore DiBene II

Doctor of Philosophy in Electrical Engineering (Applied Physics)

University of California San Diego, 2006

Professor Kevin B. Quest, Chair



Dispersion on microstrip circuits is a limitation for transmitting many high speed signals. There are numerous concepts and methods which attempt to deal with dispersion in both passive and active manners. This dissertation focuses on a particular method which *grades* the dielectric in a particular fashion in an attempt to move the dispersive characteristics upward in frequency. The thesis focuses on the problem statement, method for analysis, some numerical results, and discusses possible future methods for advancing the research.

# Chapter 1

# Introduction

## 1.1 Preliminaries

The objective of this research is to determine if step-grading the dielectric in a microstrip structure in a fashion will compensate for the inherent dispersive properties of the microstrip itself. In preparation for the formulation of the method and analysis some background on microstrips is given. This chapter introduces the microstrip structure and its inherent properties. First, a brief background of microstrips is given and their uses. This section also goes into research on developing the closed-form formulae which aided in designing microstrips; particularly for microwave applications. Next, the microstrip dispersion problem is introduced and the background for the dissertation is presented. A discussion of how the problem was bounded for issues such as attenuation and bandwidth is also dealt with. The last section deals with modeling the problem at hand and an overview of the numerical method and in particular how a given modeling approach was chosen.

## 1.2 The Step-Graded Microstrip

Figure 1.2 shows the concept that will be analyzed and explained within this dissertation. A step-graded microstrip is a microstrip where the dielectric region changes as a function of the $x$ dimension.[1] Research into this area has found that a thorough study of this structure for dispersion control appears to be unique. Additionally, through modeling and analysis it will be determined that it is possible to change the dispersive characteristics by changing the permittivity values within each region as shown in Figure 1.2. Chapter 2 discusses the formulation of the method for numerically modeling and the mathematics behind the numerical approach. Chapter 3 then discusses the results and analyzes some select step-graded microstrip structures. Chapter 4 then discusses possible future research and methods for constructing a physical demonstration vehicle that could experimentally validate the analysis.

[1] The Figure shows only changes in the $x$ dimension which is the focus of this research. However, as will be discussed in Chapter 4, other gradient structures are possible.

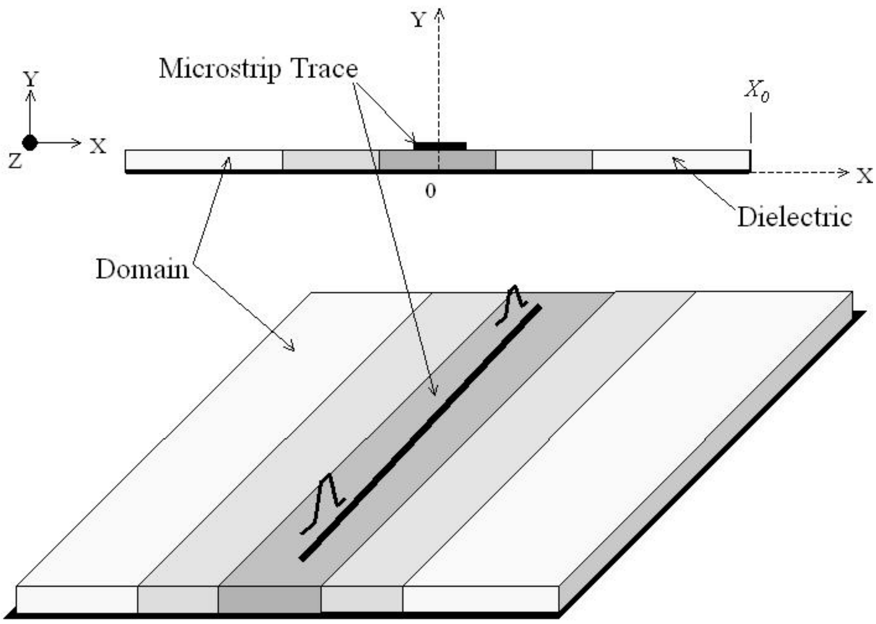


Figure 1.1: Step-graded microstrip illustration. The domains are the dielectric regions which extend into the $z$ dimension and have constant permittivity values $\epsilon_r$ but are typically different from one domain to the next.

## 1.3 Background of Microstrip

Microstrip structures have been around since the 1960's and their uses have increased significantly over the years due to ease in high-volume manufacturing and low cost. The microstrip is basically a waveguide structure (see Figure 1.2) but due to the fields existing in both air and within the dielectric region, the microstrip is intrinsically dispersive.

In the low frequency regime the electromagnetic field patterns look very similar to the *quasi-static* fields for the microstrip at DC. The *z-directed* (see Figure 1.2 again) electromagnetic fields tend to zero amplitude and propagation in the structure is similar to a *TEM* (Transverse Electro-Magnetic) transmission line. The current density distribution on the top and bottom of the strip is essentially uniform and results in fields which are distributed in both the air and dielectric regions. However, as the signal frequencies increase, the fields and the current density distribution on the trace and local ground plane tend to coalesce underneath the strip. This results in the field patterns existing predominately within the dielectric rather than in the air region. The *frequency-dependent* effective permittivity is the *figure of merit* that is used to describe this phenomenon.

During the late 1960's and throughout much of the 1970's and 1980's a significant amount of research was done on characterizing the behavior of the microstrip. Early research was limited due to the lack of computational power and thus much

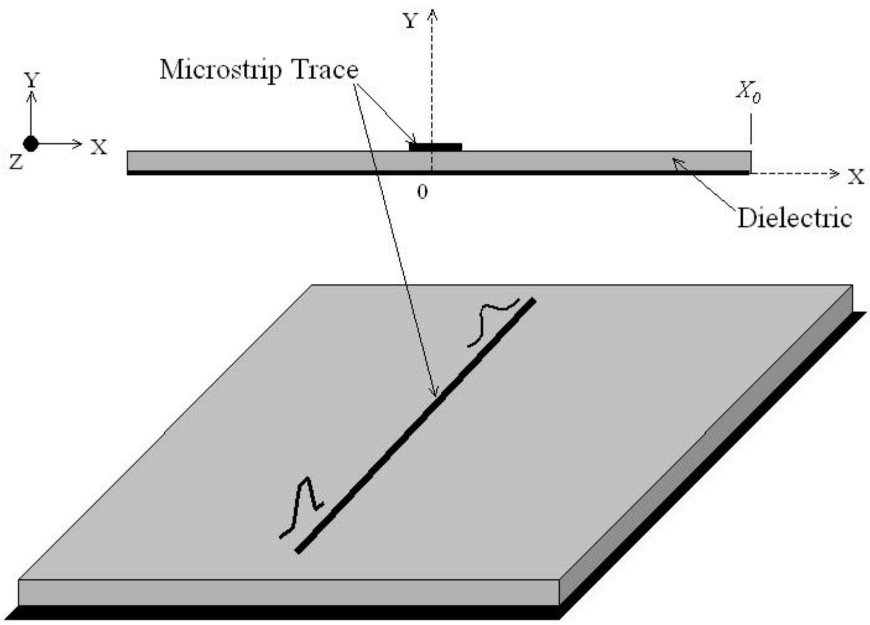


Figure 1.2: Microstrip cross-section and isometric representation.

of the work was based on analysis and experimentation. As such, one of the main goals of many researchers was to determine simple formulae which would accurately describe a microstrips behavior. There was a large thrust to come up with some simple expressions to approximate the effective permitivity of a microstrip given the geometry and dielectric constant of the materials. This was done for prediction of not only the *quasi-static* or DC behavior but also for the frequency dependent behavior. One of the main problems encountered early on was the frequency dependent effects due to dispersion. The figure of merit chosen was the frequency dependent permittivity, $\epsilon_{eff}(f)$. The research during this time resulted in a plethora of different formulae from different researchers who made significant efforts to approximate $\epsilon_{eff}(f)$ behavior in a microstrip. Figure 1.3 shows the basic shape for $\epsilon_{eff}(f)$ that researchers were attempting to accurately predict. The curve has a quasi-static limit in the lower frequency regime which is the *quasi-static permittivity* or $\epsilon_{ef0}$. The higher end of the curve is the asymptotic limit predicted by the fields predominantly existing in the dielectric region. The frequency dependent permittivity $\epsilon_{eff}(f)$ therefore tends towards the dielectric constant value $\epsilon_r$ in the dielectric region. Edwards [10] discusses many of these formulae and their subsequent accuracies including the ones used herein as references.

Researchers such as Getzinger [15] in 1973 were among the first to propose a simple expression based on analysis and experimentation for a given microstrip

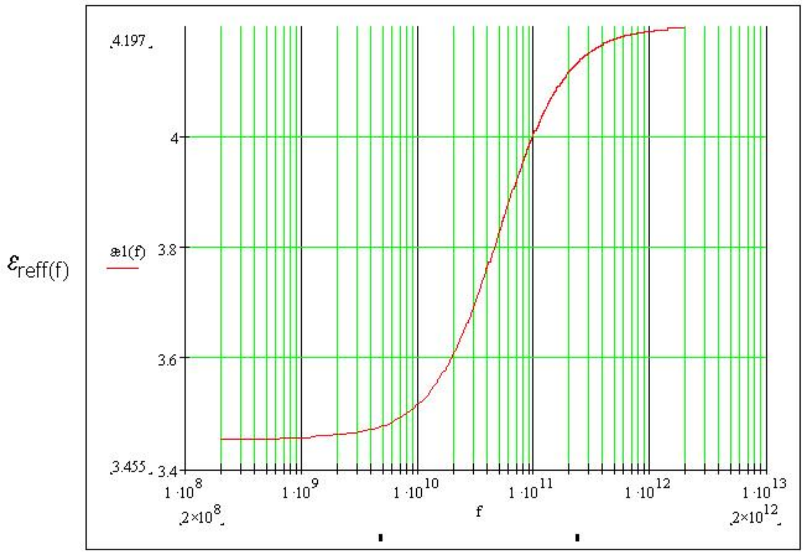


Figure 1.3: Illustration of frequency dependent permittivity $\epsilon_{eff}(f)$ for microstrip structure using closed form calculation.

structure. Later research determined though that his expression was somewhat in-accurate and limited - particularly in the higher frequency regimes. Work by Yamashita [56] and Kobayashi [23] improved upon the formulae to get more accurate characteristics in the dispersive area. However, the formulae still did not accurately predict a microstrips behavior over a wide enough frequency band and the *quasi-static* limit predictions were lacking. However, in the early 1980's Pramanick, et. al, [37] described a very simple method which was intended to predict the microstrip dispersion from a mathematical function perspective and thus the inflection frequency and strip width impacts were major improvements over previously described methods. Prior to this, Edwards & Owens [11] also measured the behavior of a given microstrip structure up to 18 GHz and developed their own expressions based upon their measurements. Pramanick, et. al, showed that their expression compared well with Edwards & Owens experimental results though Pramanick's expression was simpler. Finally, Edwards [10] reported a very accurate, though cumbersome expression by Kirsching & Jansen [21] which accurately predicted the behavior of microstrips up to nearly 100 GHz. This method, along with Yamashita's, is used later in this dissertation for comparison purposes.

## 1.4 The Microstrip Dispersion Problem

Dispersion, in general, is the phenomenon of different frequency components of an electromagnetic wave traveling at different velocities through a given medium. If the components of an electromagnetic wave are allowed to travel at different velocities, such as in a digital communication link with dispersion, the resultant waveform will be distorted and data corruption becomes more probable. Thus, the dispersive affect in a microstrip interconnect may be described as a dispersive filter. Figure 1.4 illustrates the results of sending a digital waveform down a microstrip transmission line that acts like a pure dispersive filter.

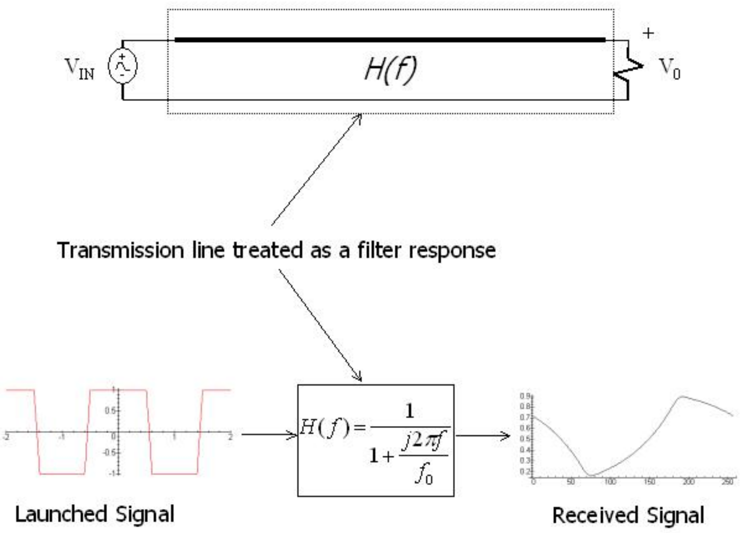


Figure 1.4: Example of how microstrip link behaves as a dispersive filter.

The frequency components which make up the launched digital pulse start out with a predefined alignment. In a non-dispersive and non-lossy medium, the waveform would end up in the same form as the launched wave. However, in a dispersive medium, the waveform becomes distorted due to the components propagating at different phase velocities and arriving at different times as represented by Figure 1.4.

### 1.4.1 Dispersion in Microstrip Communications

There are various methods which have been researched on trying to overcome or help the dispersive problem in microstrips. Some of these include encoding of the signal, wave shaping the signal, changing the properties of the media, or simply lowering the bandwidth per link (e.g. more traces). A detailed overview of the research into these subjects is well beyond the scope of this dissertation but a brief overview is warranted. It should be stated that the method described herein is not intended to supplant or replace any of these techniques but rather the research here is intended to investigate the method of step-grading a dielectric region and its usefulness as a passive dispersion control or dispersive mitigation method.

Many of the solutions today for addressing the dispersion problem in microstrips are silicon based. Active methods that involve equalization, such as described by Ahmad [1] and Leong [28] and high speed filtering are becoming more common (see Pelard [33] and others [49] [53] [25]). The reason is primarily due to cost and ease in implementation. However, for longer link lengths it is often required to model the interconnect sufficiently and then determine if some other method is required. This is because of loss in signal amplitude from the transmitted end of the link to the receiver end. Thus, much research has gone into simply testing and analyzing the high speed problem for multi-gigabit applications ( [51] [17] [57] [3]). Changing the material properties is another way to combat the attenuation and dispersion problem. Techniques such as layering the dielectric in the $y$ dimension as described by Mesa [30] and others have been used to extend the bandwidth of the link. Many of these techniques are similar to the proposed method in that the objective is to either extend out the dispersive behavior or to change the phase-velocity of the signals propagating down the microstrip (Ros [45]) and or by altering the isotropic nature of the dielectric (Velickovic [52]). Although there has been research into solving or improving the dispersion issue for high speed communication links over the past 3 decades, the general conclusion of this thesis has been that there has been limited work done in the area of altering common dielectric materials towards the end of modifying the dispersive behavior of the microstrip in the method as described in this dissertation. The next section discusses some of the system considerations behind bounding the problem.

### 1.4.2 System Considerations

The dispersive behavior of a microstrip in the 5 to 100 GHz frequency range is of particular interest for this research. The reason is that it will be shown in the next few sections that a limiting factor in communications across microstrip structures - such as in printed circuit traces - is the dispersion of the link. For this frequency band the microstrip structure requires some type of dispersion compensation to overcome signal distortion. It is apparent that a discussion of these factors is necessary before delving too deeply into the modeling portion of the research. We will therefore summarize the problem statement and describe the characteristics of the microstrip structure of interest to help in focusing the research.

Distortion of a signal transmitted across a microstrip (at these frequencies) is caused by both dispersion and attenuation. How dispersion may effect a particular signal has been previously discussed. Attenuation is affected by the materials, signal speed, and geometry in the microstrip. Moreover, since the affects of attenuation are significant it is best that a brief analysis of these effects be given prior to embarking on a detailed analysis of dispersion. This will aid in bounding the problem. [2]

To understand how dispersion affects a microstrip structure it is best to start with an example application with dispersion. Once the application is determined

[2]Signal attenuation and its effects within a microstrip line will not be a main focus of this research - that is beyond the scope this dissertation. The focus of this research is purely on changing and modeling dispersion in microstrip structures

the microstrip structure may be analyzed. As a starting point, we choose a digital application. For a digital signal we will need to address how far and at what frequencies (i.e. what bandwidth) it may propagate across a practical microstrip before it is undetectable due to the effects of dispersion and attenuation (i.e. signal distortion).

An example of such an application is a high data rate serial bus (40 Gb/s or greater) on a printed circuit board which is similar to the technology described in the references in section 1.4.1. Such an interconnect is limited by attenuation and dispersion from the geometry and materials of the microstrip structure (as well as other constraints).

Today, large numbers of parallel signals in a bus are transmitted between device packages on a printed circuit board. The parallel traces connecting to the packages limit the bus speeds due to timing issues (skew) and crosstalk effects between the transmission lines. The advantage of a serial bus over a parallel bus is that it requires less pins on the device package. A serial data bus could mitigate much of the signal density problem, though the signal data rates would have to be much higher than some silicon driver and receiver technology supports today. Nonetheless, such an application could be viable in the future.

In the design of a practical application one must consider many system effects. Shown in Table 1.1 are some system effects which are typical in the design of a digital communication link.

Table 1.1: Typical system considerations in the design of a high-speed communication link.

| System Effects | Parameters |
|---|---|
| device considerations | voltages, switching speeds, data conversion |
| device package | inductance, capacitance, resistance |
| transmission line | length, width, dielectric constant, impedance |

For a high speed serial digital communication link many parameters must be considered to maintain the efficacy of the data being transmitted. An example of a serial data application would be a parallel to serial and or serial to parallel (SERDES) data buss converter. Input signals come into one side of an integrated circuit in a parallel fashion, are conditioned, and are then sent out the other side through the transmission path in a serial data format – at very high data rates and signal frequencies. A SERDES multiplexes a large number of slower signals (such as in a micro-processor parallel bus) into a high speed serial data path and transmits the data from one device to another across a PCB (printed circuit board). Today, a microprocessor parallel bus may transmit and receive data at over 5 Gb/s. To transmit data across a serial bus in the next 5 to 10 years may require data rates 8 to 10 times this speed — say 40 Gb/s or higher. Gallium Arsenide (GaAs) as well as heterojunction bipolar transistor (HBT) devices are able to switch at speeds capable of supporting such data rates. Though some devices may transmit data close to this bandwidth, the question will be can the interconnects between them support the bandwidth.

To answer that question we first must determine the boundaries of a launched and received pulse from a given driver/receiver combination. We will assume a fictitious pair of devices since a 40 Gb/s SERDES does not practically exist. However, based upon current information [54] we may *project* what the pertinent characteristics of the driver/receiver pair would be. We know that due to the very high frequency of switching (and power consumption) that a practical device is limited in the amplitude of the voltage pulse it can drive. A reasonable peak signal pulse is 0.5V. Conversely, due to noise rejection capabilities and signal distortion at these frequencies, a receiver has limitations on the pulse amplitude of the signal it can detect. A reasonable minimum received amplitude is 75 mVpp. Thus, using these numbers we can estimate the limits of attenuation of the signal as it propagates from driver to receiver (excluding any insertion losses due to parasitics in the path). Given the information above we can estimate limitations of the transmission link. Thus, with these constraints, the signal attenuation should not exceed,

$$\alpha_{dB} = 20 \log \frac{V_o}{V_{in}} = 20 \log \frac{0.075}{0.5} = -16.5dB \tag{1.1}$$

To simplify the discussion we assume that $\alpha_{dB}$ is the maximum attenuation of the *fundamental* frequency component of the pulse (the first harmonic). Nothing is assumed as to the pulse-width distortion at this time or other system level effects. The above information gives sufficient data to aid in the characterization of a particular microstrip problem. We now address the question how far we would like the data to traverse across the medium. A reasonably long length across a printed circuit board should be 10 to 16 inches. We will assume 12 inches for this analysis which is a reasonable average number. This now gives us enough information to design a microstrip structure for the analysis to be studied.

#### 1.4.2.1 Trace Characteristics

Practical trace geometries typically range anywhere from 4 to 50 mils with the impedances of the traces ranging from 25 to 100 Ω. Trace thicknesses typically do not exceed 2 oz. (.0028 inches) for more accurate control of trace widths during the etching process [19]. Additionally, common fiberglass core thicknesses range from 2 to 60 mils [3] depending upon the impedance requirements [19]. Using a *quasi-static* approximation we can estimate the impedance of a given structure.[4] Some typical values are shown in Table 1.2.

An additional note on the trace thickness is warranted here. Since the ratio of trace to dielectric thickness is fairly low (1.4 : 8) it is often valid to assume a zero thickness conductor in the analysis. The frequencies of interest dictate the

[3] 1 mil = .001 inches

[4] The validity of the approximation will depend entirely on the limits of the quasi-TEM approximation for the frequencies involved. The data comes from a Mathcad program which uses formulae from T.C. Edwards book [10, Chapter 4]

Table 1.2: Common Trace Characteristics

| Trace Width (mils) | Dielectric Thickness (mils) | Impedance ($\Omega$) |
|---|---|---|
| 32 | 6 | 24 |
| 21 | 8 | 40 |
| 15 | 8 | 49 |
| 8.5 | 8 | 65 |
| 6 | 8 | 75 |
| 4 | 12 | 100 |

resistive losses will be solely due to skin-effect. The skin effect thickness at 20 GHz is less than 0.02 mils as compared with 8 mils to the dielectric thickness which makes it essentially a zero thickness conductor. Additionally, the height off the dielectric surface is small which allows us to assume an in-plane conductor for the trace. Thus, many numerical analyses of microstrip structures assume a zero thickness conductor for the trace to simplify the overall analysis. Anomalies such as surface roughness of the traces [10, eqn 4.56] in the bonding layer also affect the attenuation. However, ignoring these effects initially will also simplify the analysis.

Given the *system* attenuation bounds previously discussed and some practical limits in the trace itself, we can determine a reasonable microstrip construction to analyze. A brief of analysis of attenuation and dispersive characteristics for a particular configuration now follows.

#### 1.4.2.2 Attenuation

Specifying the attenuation of the microstrip interconnect is important to bound the problem. From the previous discussion the fundamental frequency component of the signal may not decay more than 16.5 dB from its original amplitude. The other harmonics (primarily frequency components 2 thru 5) will have greater attenuation but we may assume that the pulse width of the the signal is predominately due to the fundamental harmonic [22]. We can examine the attenuation characteristics of the microstrip using the formula in Ramo [43, eqn 8.6(12)] and data from Gardiol [14] with a simple Mathcad program. Figure 1.5 shows the loss characteristics for a 12" long, 30 $\Omega$ transmission line. This trace construction was chosen because of its low loss characteristics. The impedance of 30 $\Omega$ is close to the lower limit of what a practical driver can drive. Note that the dielectric losses dominate the conductor losses at the higher frequencies. The total attenuation (purple trace) shows that at near 23 GHz the maximum attenuation is 16.5 dB. This means that the fundamental frequency component of the pulse may be transmitted at slightly higher than 20 GHz. This translates to a greater than 40 Gb/s data rate. Thus, assuming the dispersive properties may be mitigated as suggested, this data rate appears achievable.

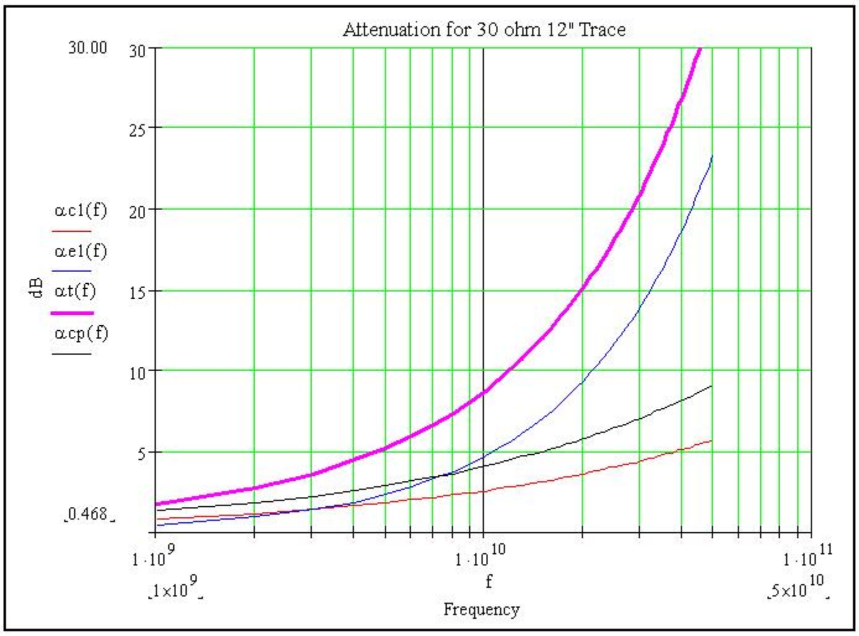


Figure 1.5: Loss characteristics of the microstrip for a 30 ohm, 12" long trace w=32, d=8 mils, where $\alpha_{c1}$ is the conductor loss, $\alpha_{cp}$ conductor loss including surface roughness, $\alpha_{e1}$ is the dielectric loss, and $\alpha_t$ the total loss.

#### 1.4.2.3 Dispersion

Given the geometry of the trace described above we now determine at what frequency should we begin to consider dispersive effects. In other words, at what frequency does the quasi-TEM approximation break down for the microstrip construction considered thus far? According to Ramo [43, eqn 8.6(11)] the frequency at which one considers the *frequency-dependent effective* dielectric constant $\epsilon_{\mathit{eff}}(f)$ is determined from the equation

$$f_{max} = \frac{21 \times 10^6}{(w + 2d)\sqrt{\epsilon_r + 1}} = \frac{(21 \times 10^6)(39.4)}{10^{-3}(32 + 2 \times 8)\sqrt{4.2 + 1}} = 7.56GHz \tag{1.2}$$

Where $w$ is the trace width, $d$ is dielectric thickness and $\epsilon_r$ is the substrate dielectric constant. This means that dispersion becomes significant for frequencies above 7.56 GHz. The frequency-dependent effective dielectric constant for the microstrip may be found from Ramo [43, eqn 8.6(9)]. An interesting exercise is to compare the *quasi-static* effective dielectric constant $\epsilon_{\mathit{ef0}}$ with the frequency-dependent effective dielectric constant $\epsilon_{\mathit{eff}}(f)$. This is shown for three trace configurations in Table 1.3.

The data shows that by increasing the impedance (decreasing trace width) the *effective* dielectric constant increases. Figure 1.6 shows that dispersion begins to occur at lower frequencies as the ratio $w/d$ increases for a fixed dielectric constant $\epsilon_r$.

We may determine, as an example, the phase shift in a 10 GHz pulse transmit-

Table 1.3: Comparison of static and frequency dependent dielectric constants for different impedances $Z_0$ and $w/d$ ratio's in microstrip transmission line structures with constant dielectric and heights $d$. ($d$ is held constant, $\Delta$=%difference, $\epsilon_{eff}(f)$ @ 10 GHz)

| Impedance | $w/d$ | $\epsilon_{ef0}$ | $\epsilon_{eff}$ (f) | $\Delta$ |
|---|---|---|---|---|
| 30 Ω | 3.94 | 3.455 | 3.517 | 1.76 |
| 50 Ω | 1.88 | 3.253 | 3.281 | 0.853 |
| 65 Ω | 1.13 | 3.096 | 3.107 | 0.353 |

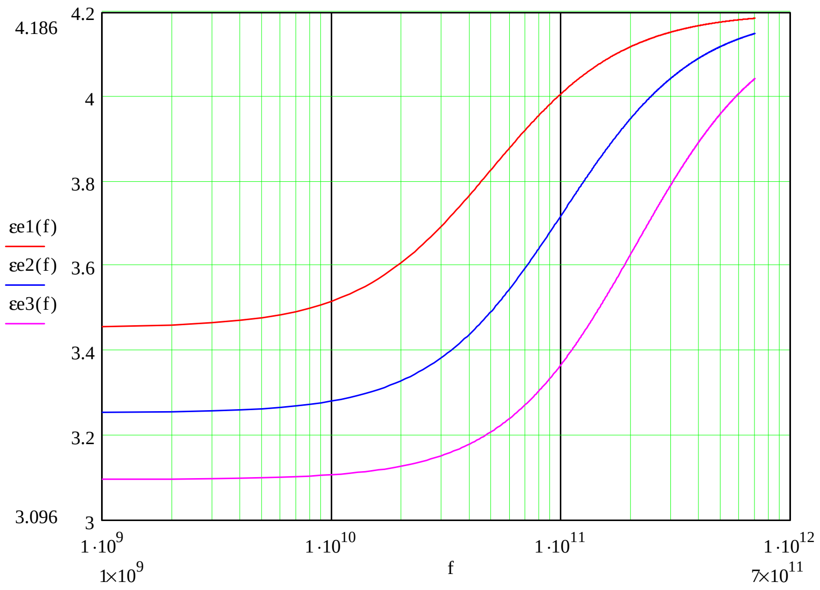


Figure 1.6: Effective dielectric constant for impedance values of 30, 50, and 60 Ω.

ted at a lower frequency across a 12” microstrip transmission line using a quasi-static approximation for the effective dielectric constant. The wavelength of the pulse is found from

$$\lambda = \frac{v}{f} = \frac{1}{f\sqrt{\mu\,\epsilon_{eff}(f)}} = \frac{39.4}{10^{10}\sqrt{4\pi \times 10^{-7} \times (8.854 \times 10^{-12} \times 3.517)}} = 0.629” \tag{1.3}$$

Thus, a 10 GHz signal will go through 19=12/$\lambda$ wavelengths when propagating down the microstrip circuit. The amount of phase shift relative to a *quasi-static* pulse is approximately 60 degrees at this frequency, or $12(\lambda_1 - \lambda_2) \times 2\pi$, where $\lambda_1$ is the wavelength of the signal thru the medium at 10 GHz and $\lambda_2$ is the wavelength of the signal in the *quasi-static* regime. Thus, significant dispersion would be evident at frequencies greater than 10 GHz for this microstrip construction. Therefore, a method for controlling dispersion would be necessary for an error-free communication path.

#### 1.4.2.4 Frequency Range

The frequency range of interest is almost known now from the previous discussion and analysis. Based upon equation 1.2 we know that dispersion becomes an issue at approximately 7.5 GHz. Our objective is to plot the wavenumber, $k_z$, as a function of frequency. Thus, a good starting point for the analysis is around 2 GHz. The high end of the frequency curve is related to the maximum significant frequency component of the propagated digital pulse. A target data rate of 40 Gb/s maximum was estimated in a previous section which translates to a fundamental pulse frequency of 20 GHz. If we assume a significant presence of the 3rd harmonic only, in addition to the first, a frequency of 60 GHz or greater is needed to ensure we capture the effects on the pulse itself. Thus, we may assume a frequency bandwidth of 80 GHz is sufficient for modeling. This range bounds the problem space for the simulations.

#### 1.4.2.5 Modeling Parameters

A summary of the modeling parameters for the microstrip trace are shown in Table 1.4. These are used as a baseline for understanding the boundaries of the problem. Additional constraints are needed for modeling the structure. These include: an understanding of the PDE governing the problem; their boundary and initial conditions; a numerically method for solving the PDE's (such as FDTD or FEM), etc. These will be discussed in detail in the adjoining sections and chapters.

### 1.4.3 Analytical Domain

The next step in the process is to determine the analytical domain for analyzing the problem and then determine a method. The end objective will be to determine a method which will allow us to model a step-graded structure and determine the

Table 1.4: Starting parameters for microstrip circuit model.

| Characteristic | Parameter | Units |
|---|---|---|
| Electrical length | 12 | inches |
| Trace Width | 32 | mils |
| Trace Thickness | 1.4 | mils |
| Trace Impedance | 30 | Ω |
| Launched Signal type | Digital | trapezoidal |
| Signal Frequency Range | 2-80 | GHz |
| Dielectric Constant | 4.2 | dimensionless |
| Maximum Fundamental Signal Attenuation | 16.5 | dB |

behavior relative to a *non step-graded* or *standard* microstrip. For this problem we consider the analytical domain to consist of a two-dimensional region, the geometry of the microstrip structure, and the characteristics of the material properties within the structure. These elements will be detailed in the following sections.

#### 1.4.3.1 Parameters for Analytical Domain

We can determine the parameters of the problem by first exploring a three-dimensional region (we will later determine that a two-dimensional model will suffice) for the model and through examining the signal components in the frequency band of interest. We have already estimated the lowest frequency component (2 GHz) that we wish to propagate into the waveguide 1.4. We can now estimate the wavelength $\lambda_0$ from knowledge of the *quasi-static* effective dielectric constant $\epsilon_{ef0}$

and the lowest frequency component $f$,

$$\lambda_0 = \frac{v_p}{f} = \frac{1}{f\sqrt{\mu\epsilon_0\epsilon_{ef0}}} = \frac{1}{2\times 10^9\sqrt{(4\pi\times 10^{-7})(8.854\times 10^{-12})(3.455)}} = 8.06cm \tag{1.4}$$

This is the longest wavelength of the signal that we may need to consider. We also need the boundaries of the region to be large enough so that we can accurately predict the behavior of the microstrip. However, if the computational domain is too large the computer time spent getting a solution may be too costly. Numerical analysis in [6, section 8.8] showed that comparatively accurate results may be achieved between an open and closed microstrip structure if the cross sectional dimensions of the computational domain were taken to be 10 times greater than the conductor strip width. However, because we are trying to determine the effects of dispersion from a *graded* dielectric structure we may need a slightly larger region. This is due to the effects on dispersion from field concentrations in the outer regions of the dielectric - particularly for lower frequencies or the *quasi-static* frequency domain. Thus, since 2 GHz is in the *quasi-static* frequency band we may assume [initially] that the boundary need not extend more than two wavelengths, or 16 cm - this is a very conservative estimate. [5]

Additionally, since the domain is symmetric, it is possible to only analyze half

[5] A more accurate method to determine the size of the solution space is to perform an error analysis iteratively on the solution itself and determine an acceptable accuracy. However, this approach is time consuming and not necessary to prove out the viability of the dispersion compensation approach at this time. Thus, using an estimate is more expedient.

of the structure to simplify the computational effort. Figure 1.7 illustrates the two-dimensional cross-section of the computational domain of interest.

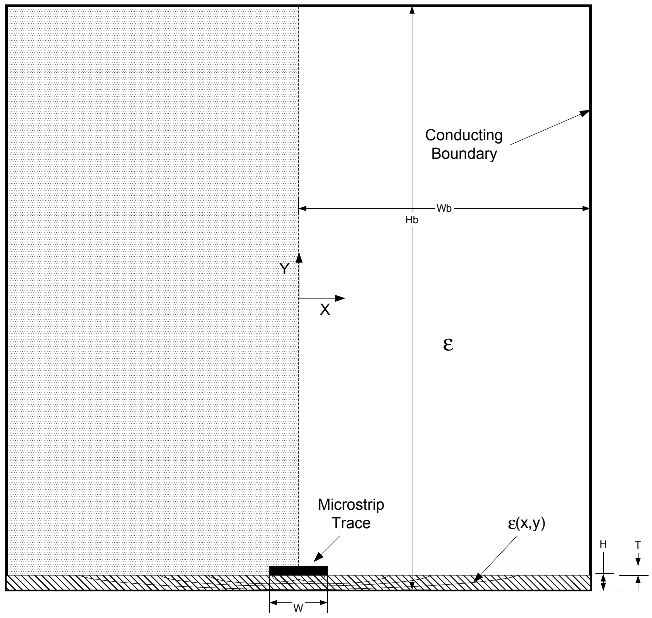


Figure 1.7: Cross Section of Computational Domain Space.

The non-shaded region the Figure 1.7 is half of the area of the waveguide which may be used as the analytical domain of interest.[6] The corresponding dimensions for the parameters of the microstrip structure shown in Figure 1.7 are additionally given in Table 1.5. These parameters were determined from the analysis in the previous sections. The maximum length of the waveguide, in the $z$ direction, is found from an estimate of the lowest frequency component of interest. All

[6]Using half the domain space is computationally more efficient. However, it was later determined that identification of *eigen-modes* was much easier when the entire two-dimensional space was analyzed and the results plotted.

dimensions are in centimeters.

Table 1.5: Dimensions of Microstrip shown in Figure 1.7

| Parameter | Metric (cm) |
|---|---|
| Wb | 16 |
| Hb | 8 |
| W | .08 |
| H | .02 |
| T | .004 |

## 1.5 Modeling the Microstrip Structure

The next step is to determine the appropriate numerical modeling approach. To begin with, the microstrip structure is inherently dispersive and does not support pure *TM* or *TE* modes. However, if the conducting strip is not present in the waveguide, the structure will support *LSE* or *LSM* modes (longitudinal section electric or magnetic). However, when the metallic strip is inserted into the waveguide again, currents flowing in both the $x$ and $z$ directions tend to couple both the *LSE* and *LSM* modes so that the final mode is *hybrid* [10]. This coupling means that both $z-directed$ electric and magnetic fields are always present for a given mode and need to be considered in the mathematical setup and method for solving the problem.

Today, it is less difficult to use numerical modeling to predict the dispersive characteristics of most microstrip structures due to the availability of cheap computing power and sophisticated modeling tools. The figure of merit is still the *frequency-dependent* effective permitivity $\epsilon_{\mathit{eff}}(f)$. However, the open nature of the microstrip makes modeling the boundaries difficult. Thus, most researches model the microstrip in a *boxed* or shielded configuration which approximates the open structure. Nonetheless, this is only an approximation to the actual structure and there are some accuracy considerations when analyzing the structure numerically in this way.

Since we may find the wave number $k_z$ as a function of frequency $f$ - $k_z = 2\pi f\sqrt{\mu\epsilon_{\mathit{eff}}(f)}$ - (which is somewhat easier than solving for $\epsilon_{\mathit{eff}}(f)$ directly due to the mathematical formulation in the numerical method) we could assume to propagate only single harmonic waves, one at a time, into the waveguide. The $FDTD$ or *Finite Difference Time Domain* method is well suited for this numerical task. Using this method, we can determine the wavenumber using single harmonic waves and truncate the length of the waveguide in the $z$-direction while propagating waves into the three-dimensional structure. For a given wavenumber $k_z$ we may wait for the signal to settle and then extract the frequency component through performing a *Fast Fourier Transform* (FFT) on the time-harmonic waveform. We may then iterate through ten periods of the signal which should be adequate for the waveform to settle. This would correspond to an electrical length of $10\lambda_0 = 80.6$ $cm$. Additionally, we may adjust the length of the waveguide for every frequency component to achieve the desired plot. However, this is just one of many possible methods to solving the problem at hand and as we will see there are limits and issues to each method.

There were a number of numerical methods investigated for analyzing the microstrip problem. The initial research focused on using the FDTD method. This is a very straight forward and easily programmable general modeling method for many electromagnetic problems (Sullivan [50]). In fact, some code was initially written in Matlab and some basic problems were solved using this method at the beginning of the research. Wharton [55] used the FDTD method to determine the dominant $EH_0$ mode in a microstrip in 1972. For a simple structure and low frequency regime this appeared adequate and compared reasonably well with measurements. However, one of fundamental problems are the sharp edges and resulting *infinite* fields around the microstrip trace. FDTD is typically based upon a uniform gridding structure and the convergence of the code and accuracy of the solution in the large gradient regions around the corners of the strip is often a problem with many microstrip structures. Railton, et. al, [38] [40] [41] [39] did a significant amount of research into extending the FDTD method to solve this problem. By adjusting the grid region size around the strip area and adding an 'adjustment' factor to the equations Railton achieved good results modeling the microstrip behavior. However, for more complex regions and multiple boundaries and multiple sharp corners, this method has limitations as well. The main reason is that creating multiple grid regions makes programming very cumbersome and the number of iterations increases dramatically with the grid size. The other issue is the stability of the solution and convergence. The solution may become unstable and not converge depending upon the acceptable error in the solution. One method that was proposed by J.Lee, et. al, [27] was to use non-orthogonal gridding in the FDTD grid. This has the advantage of allowing the grid to form around the complex boundaries and reduce the problem due to the large fields and gradients on these boundaries. This is an alternative to using a very fine mesh throughout the entire region which often results in an inordinate amount computation time for the code. Unfortunately, the method appears to suffer from convergence issues as pointed out by the authors themselves and other researchers. Moreover, it is much more complex to code than the basic FDTD method. Brankovic, et. al, [8] used a graded-mesh along with a stability factor to help in the convergence problem. This method, though still somewhat complex, did start to address the convergence and stability of the solution space using FDTD. However, the solution was still intended to be in the frequency domain space and additional coding would be necessary to solve yield solutions from the time-domain. This was also a consideration when evaluating the method.

Another issue investigated with FDTD was the boundary problem. If the problem is to emulate a true microstrip, then there is no boundary and the fields exist in infinite space. Modeling such a problem directly is impractical (if not impossible). Thus, many methods have been developed to solve this problem. Railton, et. al, [42] used an *absorbing boundary condition* or *ABC* using the FDTD method to force the fields to decay outside of the analytical domain region. Similar work in this area was done by Fang [12], Mur [31], Betz [7], and others. After analysis and research into the differences [6] into modeling a boxed structure with metallic boundaries versas one with a metallic boundary it was decided for this thesis that using a larger metallic region for the domain space would be adequate for the accuracy required.

Another numerical method that was investigated was the conformal mapping method. Conformal mapping techniques have been used in conjunction with FDTD to solve many waveguide and microstrip problems in the past [20] [32] [26]. The advantage of conformal mapping is the ability to take a complex grid space and map it into another space for ease in computation. The new mapped space can be programmed using orthogonal grids and results in the corners of the grid also being orthogonal. The advantage is similar to the non-orthogonal gridding approach by Lee [27] but with a much simpler programming methodology. Unfortunately, accuracy around the strip is still a problem due to the need for finer mesh density. This brought up another issue which was the need to create some type of grid structure in all the approaches. Though quite feasible, this adds a significant amount of time to the code development for the problem.

The approach that was eventually used was the *Finite Element Method.* There were, to be sure, many appropriate reasons for settling on this approach over others that were investigated. First, the literature is replete in using FEM for modeling waveguide and microstrip problems ([16],[2],[5],[18] as examples). Second, triangular mesh generation thru Delauny [46] and other mesh growth algorithm's are well known and available. Thus, the need to create an additional mesh generation code is unlikely. Third, the FEM approach does not suffer from the convergence issues as much as other approaches since the mesh density is typically adjusted from the geometric corners and fine grain objects outwardly, thus allowing for finer mesh sizes where the fields are most dense and coarser meshes in areas where gradients in the field solution is less. We may also assume for solving this type of problem a sinusoidal variation of the wave in both the $z$ direction and in time. This allows us to use a *2D* code to solve, in essence, a three-dimensional problem. The *Finite Element Method* was also chosen for this task rather than the others due to the complexity of the dielectric construction [47]. Additionally, though other methods such as FDTD are much more simple, they require a much larger number of mesh points when using a uniform grid structure than the FEM and thus the use of FEM for this problem reduces computational time significantly.

As previously stated, one of the initial issues was that the microstrip is similar to a dielectric waveguide in that the final solution is *hybrid*. Thus, any modeling method would need to address this issue up front. Since the finite element method is based upon variational methods, the equations to be solved are uni-functional in that only a single scalar may be solved for. Csendes [9] proposed an approach to using FEM to solving waveguide problems which solved for both the $E$ and $H$ fields directly in an eigenvalue matrix equation. This method also had the advantage of solving a structure with multiple complex domains. Though Csendes likely did not envision his method for this use, its adaptation to the more complex problem herein was elegant. Chapter 2 discusses usage of Csendes's method and the overall formulation of the numerical and mathematical method in greater detail.

# Chapter 2

# Formulation of Method for Graded-Dielectric Structures

## 2.1 Preliminaries

This chapter deals with the construction of the numerical method used to model the step-graded dielectric structure. As discussed in some detail in the previous chapter the finite element method was determined to be the method of choice for various reasons. Some of the factors leading to this decision were the complexity of the geometry, the adaptability of the method, and the ease in incorporating the methodology into a common tool space. The objective of this chapter will be to outline the mathematical algorithm and numerical method, illustrate the method through analysis of different structures - such as a shielded microstrip structure. Next a discussion of code development and changes to the method which were made in order to make it usable for step-graded structures. Finally, the issues surrounding the approach, such as accuracy and convergence will be discussed.

## 2.2 Formulation of Method and Analysis

The formulation of the problem will be to use the finite element method to numerically solve for the wavenumber $k_z$ as a function of frequency [1](see Figure 1.7). From $k_z$, we may solve for the frequency dependent permitivity $\epsilon_{eff}(f)$ which will be our *figure of merit* for determining the efficacy of the dispersive compensation approach. The problem is made more complex by the fact that the dielectric region is *inhomogeneous* which complicates the mathematics and numerical method over simpler waveguide geometries and constructions. The formulation of the problem consists of (1) deriving the proper PDE which describes the problem, (2) constructing the functional from the given PDE and the boundary elements of the problem, and (3) discretizing the functional and generating the resulting matrix equations to be solved numerically. The following mathematical formulation will be used for solving some basic waveguide structures in addition to both standard

[1]This is true for the waveguide problems where it is more conducive to compare solutions using the wavenumber $k_z$ than other parameters. For the microstrip problems, it is more practical to examine the frequency dependent permitivity $\epsilon_{eff}(f)$.

and *step-graded* microstrip problems.

### 2.2.1 Variational Expression & Matrix Formulation

For the given microstrip problem (in this case, a loss free medium), it can be assumed that the geometry is independent of $z$ (e.g. infinite in this direction). It follows that the problem can effectively be reduced from 3-D to 2-D which would substantially reduce computing and programming time. If the field components are above cutoff then the wave vector $k_z$ is real. With the previous assumptions (that the electromagnetic wave is sinusoidal in both time and in the z-direction) we can solve the boundary value problem in two dimensions rather than three. The reason is that for a given frequency the fields are stationary and the sources of the waves are at infinity while the length of the waveguide itself is infinite [48, Chapter 3]. Mathematically this means we can divide out the complex exponential term $e^{-j(k_z z-\omega t)}$. Physically, this means - in the traverse direction - that we have *standing-waves* in this structure and that for a given frequency and position along the $z$-axis the electromagnetic field patterns will be the same.

If there is no variation in $\epsilon$ in any of the dielectric regions then we are left with the *homogeneous* Helmholtz wave equations.

$$\nabla^2\vec{\mathbf{E}} - {k_d}^2\vec{\mathbf{E}} = 0 \tag{2.1}$$

$$\nabla^2\vec{\mathbf{H}} - {k_d}^2\vec{\mathbf{H}} = 0 \tag{2.2}$$

where $k_d$ is the propagation constant within the domain of interest. Equations 2.1 and 2.2 must be solved simultaneously to determine the fields for the inhomogeneous waveguides.

The generation of the functional for equations 2.1 and 2.2 may be determined by following the method found in [9] and solving for the wave vector $k_z$ along with the $z$-directed electric and magnetic fields in the previous two *homogeneous* wave equations. Given the previous assumptions, we generate the source-free Maxwell scalar equations,

$$\frac{\partial E_z}{\partial y} = -jk_z E_y - j\omega\mu H_x \tag{2.3}$$

$$\frac{\partial E_z}{\partial x} = -jk_z E_x + j\omega\mu H_y \tag{2.4}$$

$$j\omega\mu H_z = \frac{\partial E_x}{\partial y} - \frac{\partial E_y}{\partial x} \tag{2.5}$$

$$\frac{\partial H_z}{\partial y} = j\omega\epsilon E_x - jk_z H_y \tag{2.6}$$

$$\frac{\partial H_z}{\partial x} = -jk_z H_x - j\omega\epsilon E_y \tag{2.7}$$

$$j\omega\epsilon E_z = \frac{\partial H_y}{\partial x} - \frac{\partial H_x}{\partial y} \tag{2.8}$$

From the equations above, if $E_z$ and $H_z$ are known, then the other field quantities can be derived. For example, if $E_z$ and $H_z$ are known from equations 2.3 and 2.7 then $H_x$ and $E_y$ may be deduced. The behavior of the fields at the dielectric-air and boundary interfaces may be found from solving these equations. Using equations 2.3 and 2.7, and equations 2.6 and 2.4 we can represent the normal field terms $H_x$ and $E_x$ in terms of the other field quantities at all points,

$$\frac{\epsilon}{k^2}\frac{\partial E_z}{\partial y} = \frac{k_z}{\omega k^2}\frac{\partial H_z}{\partial x} - \frac{j}{\omega}H_x \tag{2.9}$$

$$\frac{\mu}{k^2}\frac{\partial H_z}{\partial y} = -\frac{k_z}{\omega k^2}\frac{\partial E_z}{\partial x} + \frac{j}{\omega}E_x \tag{2.10}$$

The fields at the boundaries of the waveguide may be determined by using equations 2.3 through 2.8 to yield $H_y$ and $E_y$ in terms of the other field quantities as well,

$$\frac{\epsilon}{k^2}\frac{\partial E_z}{\partial x} = -\frac{k_z}{\omega k^2}\frac{\partial H_z}{\partial y} + \frac{j}{\omega}H_y \tag{2.11}$$

$$\frac{\mu}{k^2}\frac{\partial H_z}{\partial x} = \frac{k_z}{\omega k^2}\frac{\partial E_z}{\partial y} - \frac{j}{\omega}E_y \tag{2.12}$$

where $k^2 = \omega^2\epsilon\mu - {k_z}^2 = {k_d}^2 - {k_z}^2$. We wish to write the previous equations 2.9 thru 2.12 in terms of a matrix equation so that later we can substitute it into the equation for the functional. This will allow us to simplify the functional relation itself. If we let $\psi = (E_z, H_z)^T$, where $T$ is the transpose of the vector for $E_z$ and $H_z$, then we may reduce equations 2.9 and 2.10 and equations 2.11 and 2.12 to two matrix pair equations.

$$\frac{1}{k^2}M\frac{\partial \psi}{\partial y} = \frac{k_z}{\omega k^2}J\frac{\partial \psi}{\partial x} - \frac{j}{\omega}J\xi_x \tag{2.13}$$

$$\frac{1}{k^2}M\frac{\partial \psi}{\partial x} = -\frac{k_z}{\omega k^2}J\frac{\partial \psi}{\partial y} + \frac{j}{\omega}J\xi_y \tag{2.14}$$

where

$$\psi = \begin{bmatrix} E_z \\ H_z \end{bmatrix}, \quad \xi = \begin{bmatrix} E_\tau \\ H_\tau \end{bmatrix}, \quad M = \begin{bmatrix} \epsilon & 0 \\ 0 & \mu \end{bmatrix}, \quad J = \begin{bmatrix} 0 & 1 \\ -1 & 0 \end{bmatrix} \tag{2.15}$$

and where $\xi_{x,y}$ is the tangential component of the fields at the metallic walls and $\tau$ is the tangential direction of the fields to the boundary. Equations 2.13 and 2.14 are now simply equations 2.9 thru 2.12 represented in terms of vectors $\psi$ and $\xi$. It is preferable to write the previous two equations in terms of one matrix equation representing the path around the boundary. To do this we may examine Figure 2.1 which illustrates the relationship between the three orthogonal vector components.

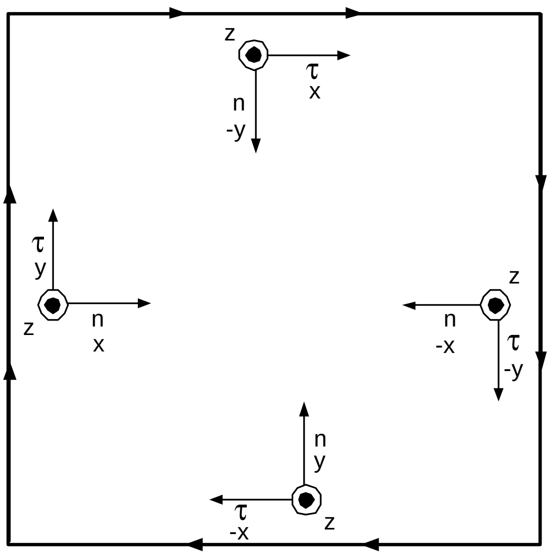


Figure 2.1: Vector directions around the path of integration.

Because we have assumed that propagation is in the positive $z$ direction – as shown out of the paper – the normal vector components to $z$, $x$ and $y$, must be consistent with that direction when the cross product of two vectors, the normal component to the interfaces and the z-directed vectors respectively, are taken during the *curl* operation in the previous Maxwell equations. Thus, beginning from the lower right-hand corner and moving *clockwise* along the bottom boundary surface we note that the normal component is in the positive $y$ direction and the tangential component is in the negative $x$ direction. This results in the cross product $\vec{y} \times \vec{z} = -\vec{x}$ which is consistent with equation 2.13 [2]. On the left-hand wall we note that the normal component is now in the positive $x$ direction and that tangential component is in the positive $y$ direction. This results in the cross product $\vec{x} \times \vec{z} = \vec{x}$ which is consistent with equation 2.14. By following the path around the boundary loop we may now write the two matrix equations 2.13 and 2.14 in terms of one matrix equation assuming $\vec{n}$ and $\vec{\tau}$ are the normal and tangential vector directions to the interfaces (respectively). This is shown in equation 2.16.

$$\frac{1}{k^2} M \frac{\partial \psi}{\partial n} = -\frac{k_z}{\omega k^2} J \frac{\partial \psi}{\partial \tau} + \frac{j}{\omega} J \xi \tag{2.16}$$

This is essentially the result obtained by Csendes and Silvester [9, page 2, equation 7]. Following their method, we can derive the functional for the inhomogeneous microstrip case. We wish to solve the PDE of the form,

$$M(\frac{1}{k^2} \nabla^2 \psi + \psi) = 0 \tag{2.17}$$

where $\nabla^2$ is the $x, y$ gradient operator squared. Note that we have multiplied each equation for $E_z$ and $H_z$ by the constants $\epsilon$ and $\mu$ respectively. This allows us to simplify the equations when making substitutions later on in the derivation.

[2] note that we have defined a left-hand coordinate system here

Using a method similar to that in Sadiku [47], we generate the functional for the homogeneous domain we are interested in. Note there are actually 2 *matrix* PDE's that are defined in 2.17; one where $\epsilon$ is the value in the air region and one where it is the value in the dielectric region. If $\psi$ is the true solution then the functional $F(\phi)$ is stationary when $\phi$ equals the true solution $\psi$,

$$F(\phi) = \frac{1}{k^2}\int_r \phi^T M \nabla^2 \phi dr + \int_r \phi^T M \phi dr \tag{2.18}$$

where $\phi^T$ is the transpose of the stationary solution $\phi$. Integrating by parts the first term on the right of 2.18 yields,

$$\begin{aligned} F(\phi) = -\frac{1}{k^2}\int_r \nabla\phi^T M \cdot \nabla\phi dr + \\ \frac{1}{k^2}\oint_\tau \phi^T M \frac{\partial\phi}{\partial n} d\tau + \int_r \phi^T M \phi dr \end{aligned} \tag{2.19}$$

where $r$ is the area of the region over which the integration is to take place, in this case, the $x$ and $y$ region previously defined in Chapter 1 for the domain space. Substituting the right side of equation 2.16 into the second term of equation 2.19 above yields,

$$\begin{aligned} F(\phi) = -\frac{1}{k^2}\int_r \nabla\phi^T M \cdot \nabla\phi dr - \frac{k_z}{\omega k^2}\oint_\tau \phi^T J \frac{\partial\phi}{\partial\tau} d\tau + \\ \frac{j}{\omega}\oint_\tau \phi^T J \xi d\tau + \int_r \phi^T M \phi dr \end{aligned} \tag{2.20}$$

According to [9], the third integral on the right of equation 2.20 vanishes due to the tangential electric fields vanishing at the walls of the waveguide and due to the continuity of the fields at the internal boundaries of the union of the homogeneous regions. We may see this by expanding this integral in terms of the individual $E_z$ and $H_z$ components as in equation 2.21.

$$\frac{j}{\omega}\oint_{\tau}\phi^T J\xi d\tau = \frac{j}{\omega}\oint_{\tau}\left(E_z H_\tau - E_\tau H_z\right) d\tau \tag{2.21}$$

The current waveguide structure has 3 *Dirichlet* boundaries on the top, bottom and right-hand sides, and one *Neumann* boundary down the axis of the microstrip. The top and bottom boundaries have tangential $E_z$ and $E_x$ fields equal to zero. Thus, since $\tau$ represents the line path of the tangential component of the boundary in question, the integrand of the integral in equation 2.21 is zero for these boundaries. The right-hand boundary has tangential $E_z$ and $E_y$ fields going to zero and again, for this integral the integrand and integral is zero. For the internal boundaries along the dielectric-air interface (or dielectric-dielectric interface between domains), the tangential fields are continuous across the boundary and thus, since the path is traversed twice, in opposite directions when each region is integrated upon in equation 2.21, when the boundary conditions are applied to each domain (e.g. between the two regions) the contributions from each integral cancel and thus again the integral is zero. For fields at lines of symmetry, $H_\tau$ and $H_z$ are zero and thus the integral is zero as well.

Conversely, we may expand the second integral on the right-hand side of equation 2.20.

$$\frac{k_z}{\omega k^2}\oint_\tau \phi^T J\frac{\partial\phi}{\partial\tau}d\tau = \frac{k_z}{\omega\left(\omega^2\mu\epsilon_d - k_z^2\right)}\oint_\tau\left(H_z\frac{\partial E_z}{\partial\tau} - E_z\frac{\partial H_z}{\partial\tau}\right)d\tau \tag{2.22}$$

Similar to the previous analysis for equation 2.21, the *Dirichlet* boundaries go to zero as well. However, as can be seen in equation 2.22, between two regions of different permittivity the integral is non-zero. Thus, equation 2.22 contains the boundary information for the region of interest.

Though computational time is increased, it was decided to integrate over the entire domain rather than half of the domain. This allows for viewing the fields more readily and for locking onto the proper eigenvalue. Thus, after eliminating this term from equation 2.20 and using Stoke's Theorem on the second term (e.g. changing the line integral into a surface integral) we get,

$$F(\phi) = -\frac{1}{k^2}\int_r \nabla\phi^T M\cdot\nabla\phi dr -$$
$$\frac{k_z}{\omega k^2}\int_r(\nabla\phi^T J\times\nabla\phi)\cdot\hat{z}dr + \int_r \phi^T M\phi dr \tag{2.23}$$

This is the functional that we now need to discretize. Note that the boundary conditions at the dielectric-air and dielectric-dielectric interfaces which are contained in the second integral on the right-hand side of equation 2.23 are more complex than the Dirichlet boundaries and require special consideration in the setup of the problem. However, changing to a surface integral simplifies the code development somewhat for the boundary integral; this will be discussed in subsequent sections.

### 2.2.2 Discretization: The Raleigh-Ritz Method

Following along the method in [9] we now discretize the functional in equation 2.23. We will assume for each triangle element $m$ that the solution is in the form of a first order linear function, i.e.

$$\psi^m(E_z, H_z) = a + bx + cy \tag{2.24}$$

where a, b, and c are coefficients to be determined. Higher order terms may be used to approximate the solution within an element [44] but results obtained on similar structures [2] has shown that this is not necessary to obtain very accurate results. Thus, assuming the linear approximation for the solution within each element, the total solution takes on the form

$$\psi_1 = E_z = \sum_{i=1}^{n} e_i \alpha_i(x, y), \quad \psi_2 = H_z = \sum_{i=1}^{n} h_i \alpha_i(x, y) \tag{2.25}$$

where $e_i, h_i$ are the field solutions at the nodes of each finite element, $\alpha_i$ are the element *shaping functions* derived from solving equation 2.24 for the coefficients for $n$ nodes, and where again $\psi = [E_z, H_z]^T$. We now substitute the equations in 2.25 into equation 2.23. We first expand the first term on the right hand side of equation 2.23 and substitute in equations 2.25.

$$
\begin{aligned}
-\frac{1}{k^2}\int_r \nabla\phi^T M\cdot\nabla\phi dr &= -\frac{1}{k^2}\int_r \left(\epsilon\left(\nabla E_z\right)^2+\mu\left(\nabla H_z\right)^2\right)dr \\
&= -\int_r \left[\sum_{i=1}^{n} e_i\nabla\alpha_i \sum_{j=1}^{n} e_j\nabla\alpha_j\frac{\epsilon_d}{k^2}\right] + \\
&\qquad \left[\sum_{i=1}^{n} h_i\nabla\alpha_i \sum_{j=1}^{n} h_j\nabla\alpha_j\frac{\mu_d}{k^2}\right] dr \\
&= -\sum_{i=1}^{n}\sum_{j=1}^{n}\int_r \nabla\alpha_i\nabla\alpha_j dr\frac{e_ie_j\epsilon_d}{k^2} \\
&\quad -\sum_{i=1}^{n}\sum_{j=1}^{n}\int_r \nabla\alpha_i\nabla\alpha_j dr\frac{h_ih_j\mu_d}{k^2} \\
&= -\sum_{i=1}^{n}\sum_{j=1}^{n} S_{ij}\frac{e_ie_j\epsilon_d}{k^2} - \sum_{i=1}^{n}\sum_{j=1}^{n} S_{ij}\frac{h_ih_j\mu_d}{k^2}
\end{aligned}
\tag{2.26}
$$

where $S_{ij}$ is the integral under the summation. The elements $h$ and $e$ are to be determined and the last integral in equation 2.26 is to be computed. We now expand and substitute in for the second term on the right side of equation 2.23 and simplify.

$$
\begin{aligned}
\frac{k_z}{\omega k^2}\oint_\tau \phi^T J\frac{\partial\phi}{\partial\tau}d\tau &= \frac{k_z}{\omega k^2}\oint_\tau \left[-H_z\frac{\partial E_z}{\partial\tau}+E_z\frac{\partial H_z}{\partial\tau}\right]d\tau \\
&= \sum_{i=1}^{n}\sum_{j=1}^{n}\oint_\tau \left[\alpha_i\frac{\partial\alpha_j}{\partial\tau}-\alpha_j\frac{\partial\alpha_i}{\partial\tau}\right]d\tau\frac{e_ih_jk_z}{\omega k^2} \\
&= \sum_{i=1}^{n}\sum_{j=1}^{n} U_{ij}\frac{e_ih_jk_z}{\omega k^2}
\end{aligned}
\tag{2.27}
$$

where $U_{ij}$ is the integral under the summation. We note that the elements in the summation in equation 2.27 are coupled. The terms on the internal boundaries of $\tau$, the boundary path, will force any coupling in the matrix formulation which will result in coupling between the fields. Finally, we substitute in for the last integral of equation 2.26 and simplify.

$$\begin{aligned}\int_r \phi^T M \cdot \phi dr &= \int_r \left(\epsilon E_z^2 + \mu H_z^2\right) dr \\ &= \sum_{i=1}^{n}\sum_{j=1}^{n}\left[\int_r \alpha_i \alpha_j dr\right] e_i e_j \epsilon_d \\ &+ \sum_{i=1}^{n}\sum_{j=1}^{n}\left[\int_r \alpha_i \alpha_j dr\right] h_i h_j \mu_d \\ &= \sum_{i=1}^{n}\sum_{j=1}^{n} T_{ij} e_i e_j \epsilon_d + \sum_{i=1}^{n}\sum_{j=1}^{n} T_{ij} h_i h_j \mu_d \end{aligned} \tag{2.28}$$

where $T_{ij}$ is the integral under the summation terms. We now combine all the elements from 2.26, 2.27, and 2.28 and note that the functional in equation 2.23 is stationary at the true solution. Thus, using the *Raleigh-Ritz* method we wish to find the minimum of the functional $\frac{\partial F(\phi)}{\partial u} = 0$. Thus, we get two sets of $2n$ equations in terms of $h_i$ and $e_i$.

$$\begin{aligned}F(\phi) = -\sum_{i=1}^{n}\sum_{j=1}^{n} S_{ij}\frac{e_i e_j \epsilon_d}{k^2} - \sum_{i=1}^{n}\sum_{j=1}^{n} S_{ij}\frac{h_i h_j \mu_d}{k^2} - \\ \sum_{i=1}^{n}\sum_{j=1}^{n} U_{ij}\frac{e_i h_j k_z}{\omega k^2} + \sum_{i=1}^{n}\sum_{j=1}^{n} T_{ij} e_i e_j \epsilon_d + \sum_{i=1}^{n}\sum_{j=1}^{n} T_{ij} h_i h_j \mu_d\end{aligned} \tag{2.29}$$

The functional is stationary when we take the partial with respect to the coefficients $u_k$ where $u_k = [e_k, h_k]^T$ [3], or

[3] We note the unfortunate use of the index term $k$ with the corresponding wavevector notation $k$ in the formulation. It should be clear the the wavevector is not indexed in any fashion unlike the field and integral matrices $S, U, T$ which are in the summations.

$$\frac{\partial F(\phi)}{\partial u_k} = 0 \tag{2.30}$$

If we differentiate with respect to the coefficients $u_k$, we end up with the following two matrix equations where the first has been differentiated with respect to $e_k$ and the second with respect to $h_k$.

$$-\sum_{j=1}^{n} S_{kj}\frac{e_j\epsilon_d}{k^2} - \sum_{j=1}^{n} U_{kj}\frac{h_j k_z}{2\omega k^2} = -\sum_{j=1}^{n} T_{kj}e_j\epsilon_d, \quad \forall k \tag{2.31}$$

$$-\sum_{j=1}^{n} S_{kj}\frac{h_j\mu_d}{k^2} + \sum_{j=1}^{n} U_{kj}\frac{e_j k_z}{2\omega k^2} = -\sum_{j=1}^{n} T_{kj}h_j\mu_d, \quad \forall k \tag{2.32}$$

where both equations 2.31 and 2.32 may be written in terms of one equation,

$$\sum_j \frac{1}{\mu_d\epsilon_d - \frac{1}{v_p{}^2}} \begin{bmatrix} \epsilon_d S_{kj} & \frac{1}{2v_p}U_{kj} \\ \frac{-1}{2v_p}U_{kj} & \mu_d S_{kj} \end{bmatrix} \begin{bmatrix} e_j \\ h_j \end{bmatrix} = \omega^2 \sum_j \begin{bmatrix} \epsilon_d T_{kj} & 0 \\ 0 & \mu_d T_{kj} \end{bmatrix} \begin{bmatrix} e_j \\ h_j \end{bmatrix}, \quad \forall k \tag{2.33}$$

And where we have made the substitution $k_z = \frac{\omega}{v_p}$. Equation 2.33 is now in the form of an *eigenvalue* equation

$$\hat{\mathbf{A}}\vec{u} = \lambda\hat{\mathbf{B}}\vec{u} \tag{2.34}$$

with

$$\hat{\mathbf{A}} = \sum_j \frac{1}{\mu_d\epsilon_d - \frac{1}{v_p{}^2}} \begin{bmatrix} \epsilon_d S_{kj} & \frac{1}{2v_p}U_{kj} \\ \frac{-1}{2v_p}U_{kj} & \mu_d S_{kj} \end{bmatrix}, \hat{\mathbf{B}} = \sum_j \begin{bmatrix} \epsilon_d T_{kj} & 0 \\ 0 & \mu_d T_{kj} \end{bmatrix}, \vec{u} = \begin{bmatrix} e_j \\ h_j \end{bmatrix} \tag{2.35}$$

and where the eigenvalues, $\lambda = \omega^2$. Additionally, for a given value of $v_p$ and the corresponding material properties of the *domain* where the fields exist, the eigenvalues $\omega^2$ may be solved for along with the field values. Appendix A.1 gives an initial value for the velocity of propagation $v_p$ for the *quasi-static* approximation. This may be used to initially compute, or compare, the first eigenvector at the first frequency. Consequently, the wave vector $k_z$ may be easily computed from $k_z = \frac{\omega}{v_p}$. The *frequency dependent* permitivity $\epsilon_{eff}(f)$ may now be determined from knowledge of the frequency $f$ and the wave vector $k_z$ for analyzing the microstrip structures.

#### 2.2.2.1 Computation of Integrals for Finite Elements

The integrals to be computed were given in equations 2.26, 2.27, and 2.28 and are shown below.

$$S_{ij} = \int_r \nabla\alpha_i \nabla\alpha_j dr \tag{2.36}$$

$$U_{ij} = \oint_\tau \left[\alpha_i \frac{\partial\alpha_j}{\partial\tau} - \alpha_j \frac{\partial\alpha_i}{\partial\tau}\right] d\tau \tag{2.37}$$

$$T_{ij} = \int_r \alpha_i \alpha_j dr \tag{2.38}$$

The first and third integrals have already been solved for in Sadiku [47, Chapter 6] with the results of that analysis repeated here in brief. The solution to the first integral $S_{ij}$ becomes,

$$S_{ij} = \int_r \nabla\alpha_i \nabla\alpha_j dr = \frac{1}{4A}\left(P_i P_j - Q_i Q_j\right) \tag{2.39}$$

where $i, j$ are the nodes corresponding to a particular *triangular* element $e$ and the variables on the right-hand side of equation 2.39 are defined as follows,

$$P_1 = (y_2 - y_3), P_2 = (y_3 - y_1), P_3 = (y_1 - y_2) \tag{2.40}$$

$$Q_1 = (x_3 - x_2), Q_2 = (x_1 - x_3), Q_3 = (x_2 - x_1) \tag{2.41}$$

$$A = \frac{1}{2}(P_2 Q_3 - P_3 Q_2) \tag{2.42}$$

The subscripts in 2.42 correspond to local nodes $k'$ of element $e$ where $k' = 1, 2, 3$. The solution to the third integral is,

$$T_{ij} = \int_r \alpha_i \alpha_j dr = \begin{cases} \frac{A}{12}, i \neq j \\ \frac{A}{6}, i = j \end{cases} \tag{2.43}$$

The second integral on boundary equation 2.37 remains to be computed. Csendes [9] initially computed a line integral here likely because of the reduction in computational time which was necessary with the limited computing resources of the time. However, because the other integrals are over the entire region it was more expeditious and elegant for programming purposes to compute the second term on the right hand side of equation 2.23 as an area integral also and solve it over the entire region as well. Expanding this integral from equation 2.23 in terms of $E_z$ and $H_z$ yields the following,

$$\int_r (\nabla\phi^T J \times \nabla\phi) \cdot \hat{z} dr = 2\int_r \left( \frac{\partial E_z}{\partial x}\frac{\partial H_z}{\partial y} - \frac{\partial H_z}{\partial x}\frac{\partial E_z}{\partial y} \right) dr \tag{2.44}$$

We may now substitute in for the discretized elements from equation 2.25. After some simplification and re-arrangement of the integrand components we get the following result

$$\int_r \left( \frac{\partial E_z}{\partial x}\frac{\partial H_z}{\partial y} - \frac{\partial H_z}{\partial x}\frac{\partial E_z}{\partial y} \right) dr = \sum_{i=1}^{n}\sum_{j=1}^{n} e_i h_j \int_r \left( \frac{\partial \alpha_i}{\partial x}\frac{\partial \alpha_j}{\partial y} - \frac{\partial \alpha_j}{\partial x}\frac{\partial \alpha_i}{\partial y} \right) dr \quad (2.45)$$

where we may now replace the boundary integral term $U_{ij}$ in equation 2.27 with

$$\sum_{i=1}^{n}\sum_{j=1}^{n} 2W_{ij}\frac{e_i h_j k_z}{\omega k^2} \quad (2.46)$$

where

$$W_{ij} = \int_r \left( \frac{\partial \alpha_i}{\partial x}\frac{\partial \alpha_j}{\partial y} - \frac{\partial \alpha_j}{\partial x}\frac{\partial \alpha_i}{\partial y} \right) dr \quad (2.47)$$

This integral in equation 2.47 is the last integral that must be computed prior to assemblage of the matrices for solving the eigenvalue problem. The integral is readily computed using Sadiku [47] which yields

$$W_{ij}^e = \frac{1}{4A}\left[ (P_i Q_j) - (P_j Q_i) \right] \quad (2.48)$$

where $W_{ij}^e$ is the value of the matrix for element $e$ and where $i, j$ are the local numbering of the nodes within that element. Thus, the final form of the eigenvalue problem that must be solved is shown in equation 2.49.

$$\sum_j \frac{1}{\mu_d \epsilon_d - \frac{1}{{v_p}^2}} \begin{bmatrix} \epsilon_d S_{kj} & \frac{1}{v_p} W_{kj} \\ \frac{-1}{v_p} W_{kj} & \mu_d S_{kj} \end{bmatrix} \begin{bmatrix} e_j \\ h_j \end{bmatrix} = \omega^2 \sum_j \begin{bmatrix} \epsilon_d T_{kj} & 0 \\ 0 & \mu_d T_{kj} \end{bmatrix} \begin{bmatrix} e_j \\ h_j \end{bmatrix}, \quad \forall k \quad (2.49)$$

note the factor 2 is no longer in the denominator of the off-diagonal matrix terms. This due to the result of computing the $W$ element matrix for the boundary integral. The other note that should be mentioned is that there is now a negative sign in the lower left $W_{kj}$ matrix. This is due to differentiating with respect to $h_k$ in the second matrix equation which results in an index for the $W$ matrix that is reversed, or $W_{jk}$. However, from the definition in equation 2.44, we know that $W_{jk} = -W_{kj}$ which gives the desired result.

### 2.2.3 Solving the Eigenvalue Equation

The eigenvalue equation shown in equation 2.49 may be solved a number of ways. Fortunately, Matlab has an eigenvalue solver that is quite efficient and solves these types of problems quickly and accurately. However, a brief discussion of the method is still warranted.

We wish to solve the eigenvalue problem of the form $\hat{\mathbf{A}}\vec{u} = \lambda\hat{\mathbf{B}}\vec{u}$ as shown in equation 2.34. In this case, $\omega^2$ are the *eigenvalues* in the problem (or $k^2$) are the frequencies in which a particular mode propagates in a waveguide or microstrip structure. The *eigenvectors* here are the field distributions of z-directed electric and magnetic fields. The first $n$ elements of the $2n$ size vector $\vec{u}$ correspond to the field distribution for $e_z$ and second set of $n$ elements correspond to $h_z$.

To solve for the eigenvalues and eigenvectors the Matlab subroutine assumes that the matrix $\mathbf{B}$ is *symmetric* and *positive-definite*. Because the matrix $\mathbf{B}$ is automatically symmetric, due to the fact it is constructed from two matrices $T$ and the *zero* matrix, we need only check for *positive-definiteness*. The matrix $T$

is *positive-definite* by the fact that each element inside of $T$ is constructed from the area of each triangle in the mesh. Thus, since $T$ is *positive-definite*, $\mathbf{B}$ will be also. Thus, a Cholesky factorization [35] may be done on the matrix to simplify and accelerate the computations.

## 2.3 Adaptations for Numerical Analysis

As previously stated, the basis for the algorithm used in the numerical analysis for this thesis was previously developed by Csendes [9] and Ahmed [2]. Their method basically used a matrix formulation to couple the electric and magnetic fields in the diagonal blocks of the eigenvalue matrix equation and solved for the *z-directed* $E$ and $H$ fields. However, it is unlikely that either author envisioned the future use for their method as described herein and thus a number of changes were necessary in order to adapt the method towards solving step-graded microstrip problems. These differences will now be outlined.

The list below illustrates the main changes;

1. Discretization of boundary value surface integral rather than line integral.

2. Analysis of equations for internal dielectric boundary solutions.

3. Adaptation of discretization of FEM structure from *weak formulation* to Rayliegh-Ritz.

4. Generation of modular FEM code structure for solving multi-region step-graded problems.

5. Solution module for Dirichilet boundary conditions.

6. Visualization module for extraction of other field quantities.

7. Generation of static code for verification of *quasi-static* limit.

The first necessary change was in discretizing the boundary value surface integral. The code assembly routines were all written in Matlab language and though this is slightly simpler than Fortran or C the complexity of coding for solving generic electromagnetic problems capable of handling complex structures like the step-graded problem was still quite large. Thus, it was decided to keep the module solutions similar for partial re-use and ease in debugging. Thus, instead of discretizing a line integral for the boundary matrix, using Stokes theorem, a surface integral was generated. This integral is shown again in equation 2.50 for completeness and is a repeat from one equations in section 2.2.1. The actual discretizing equations were also not described by either Csendes nor Ahmed and a method used by Sadiku [47] was adopted for this in all of the code development.

$$\int_r (\nabla\phi^T J \times \nabla\phi) \cdot \hat{z} dr \tag{2.50}$$

The second change was to analyze the boundary value equations for the numerical method chosen. This was shown in section 2.2.1 and Figure 2.1 visually. Though

Csendes discussed the boundary conditions in his papers he did not show the methodology or rationale behind it. The coupled matrix equation meant that during the *curl* operations for Maxwell's equations that all of the field conditions needed to be consistent. This had to be true for the boundary conditions as well. However, the problems Csendes analyzed did not have any *x-direction* dielectric boundaries internal to the solution space whereas the step-graded structure did. Thus, all of the field solutions needed to be analyzed and the equations kept consistent in order to solve the problem at hand. This was mainly an issue for the abutment of dielectric regions across the base of the microstrip structure. It was determined after this exercise in *vector* notation that the variational equation was self-consistent for the internal boundary conditions as described in section 2.2.1.

Both Ahmed and Csendes used the Rayleigh-Ritz method to discretize their variational equations. However, the Matlab PDE Toolbox internally was created with modules that used the *weak* formulation or *Galerkin's* method. Thus, the assemblage of the matrices was slightly different than what the authors likely used. The structure of the *point* and *triangle* matrices required a specific mapping between the call functions in the code and the matrix formulation. It was not known what mesh generation routine the authors used (and subsequent mesh output) but it appeared that the triangles were uniform and thus this made their creation and mapping to the code more deterministic. The PDE Toolbox uses a *Delauny* algorithm to generate the mesh structure where the triangle size and position is non-deterministic. This results in mesh matrices which require a more in-depth decoding to extract the proper solution for the discretized field equations on a triangle by triangle basis. For example, triangle 25 may be associated with triangle 348 which meant that the algorithm would need a pointer relationship between them in order to make sure the adjacent positions were mathematically calculated properly at the edges of the triangles.

The fourth item was in creating a modular set of code for the step-graded problem. One continuous program would have been possible but likely very complex. Thus, the code was broken up into *modules* for simplicity. Neither Ahmed nor Csendes ever discuss the code development in any detail in their papers. Moreover, since Matlab was not invented at this time [4] it would impossible for them predict the nuances of the code that would be required to solve more complex problems. The numerical code was broken up into *modules* based upon the assemblage routines for the matrix elements. A main *call* module was used to solve the main equations and generate the eigenvalue solutions. The details of this are given in the next section. However, 7 main routines were generated to solve the step-graded microstrip problem. The code was written to be very flexible in that virtually an unlimited number of dielectric domains may be generated in the solution space and the structure solved for. This is why the code was used designed to

[4] Matlab was invented in the late 1970's by Cleve Moler of the University of New Mexico

solve very simple waveguide structures as well as complex microstrip structures as well. Originally, each module was debugged and tested with simpler structures and then the results verified with known problems (see appendix B.1). This resulted in a very generic numerical code with wide usage.

Though the authors must have had a method for applying *Dirichilet* boundary conditions this was not discussed. A module was created using the method outlined in Reddy [44] and applied after the matrices were assembled. This routine was verified on simpler waveguide problems as well.

The sixth task was to create a routine to visualize the output. Though Matlab has many plotting routines the input to such routines needed to be compatible. A plotting routine was created which solved for all of electromagnetic fields from $E_z$ and $H_z$ the solution scalar values in the problem. This allowed one to easily determine the correct field configurations as well as identify the proper eigenvalue solutions to the problem for the $EH_0$ mode in the step-graded problems.

Finally, a static code module was developed to verify the *quasi-static* limit of the code. Both Csendes and Ahmed pointed out that accuracy and convergence issues are evident in the solution near this limit due to the field solutions going to zero and eventually becoming complex for some modes. Thus, to validate the results in this regime it was necessary to create a static code that predicted this limit within some accuracy. This was difficult because of the varying mesh densities and the correlation of the results to the frequency based solution. However, reasonable results were achieved from this code and it was used as a good check on the larger frequency dependent code.

It was clear that neither Csendes nor Ahmed describe solving complex microstrip structures. In fact, the literature at the time was mainly focused on coming up with numerical solutions to in-homogeneous waveguides which is much simpler than a step-graded microstrip. Only Csendes briefly described a microstrip like application in one of his papers where the solution was previously known [9]. Moreover, most of the solutions were for very simple structures which were geared towards computational efficiency rather than accuracy and complexity and thus the mesh density was quite low. For this reason, highly symmetrical structures were used. This lead to problems where only half or a quarter of the solution space was solved for. Though their methods were efficient, for complex problems - such as the step-graded microstrip structure - the method required the fairly substantial adaptation in order to be used for the more complex problem at hand. The next section discusses some additional details in the construction of the code for the step-graded problem.

## 2.4 Construction of Program

As discussed previously, *Matlab* was the environment used for program development and simulations. This choice was made to expedite the process. Because of its advanced plotting routines and *PDE Toolbox* (for solving partial differential equations), the method was very adaptable to solving the step-graded microstrip problem. The *PDE Toolbox* has a mesh generation program that allows for porting of the mesh matrices to the Matlab environment to be called by various codes for manipulation. The procedure in the developing the code was to create a set of subroutines that compiled the key matrices in the FEM structure which would then be called from a main program which solved the eigenvalue problem. Once the code was created, the procedure for getting results follows the flow chart in Figure 2.2.

The inputs to the main program were the phase velocity ($v_p$), the effective permitivity ($\epsilon_{eff}(f)$), the permitivity constant of the dielectric domains ($\epsilon_r(d)$), an estimate for the eigen solver for the frequency of interest (feigs), and the number of eigenvalues around the estimated frequency (numeigs). The output from the program is a set of frequencies corresponding to a given $\epsilon_{eff}(f)$. The eigenvalues of the problem were actually the frequency components of the problem. The columns in the resulting solution were the eigenvectors which were the associated z-directed electric and magnetic fields for that eigen-frequency. Thus, once the eigenvalue was

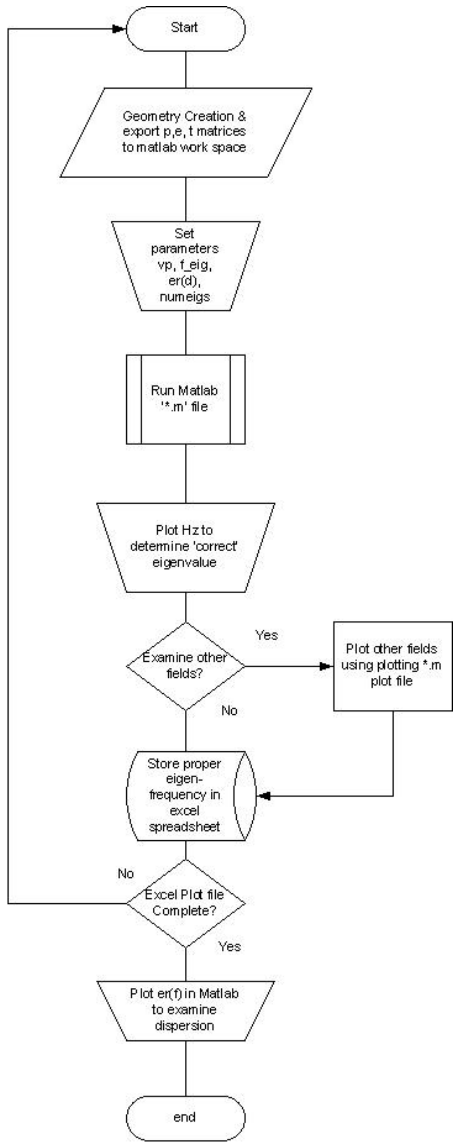


Figure 2.2: Flow chart of the procedure for determg the eigenvalues of the problem from the FEM code.

found, plotting of the associated fields was straightforward. Determination of the 'correct' eigenvalues was made challenging due to the need to examine each z-directed field associated with a given eigenvalue. The correct eigenvalue was one that resulted in the field pattern for the $EH_0$ mode for the microstrip structure. The determination of this mode is discussed in the next section. However, since there is no literature or data on a step-graded structure and its associated modes, the challenge was to determine field patterns which resembled the $EH_0$ mode for a standard microstrip. This is also discussed in subsequent sections.

### 2.4.1 Dimensional and Material Considerations

As discussed in section 1.4.3.1, the dimensions used for the analysis of the microstrip problem were much larger then the actual structure (approximately 10 times larger than conventional microstrips). This was done (at the time) mostly to increase the mesh size relative to the given analytical domain for computational efficiency. This also has the effect of changing the frequency band of the results during simulation which must be accounted for in the analysis. It is true, however, that the domain could have been shrunk to match the more *realistic* dimensions for the microstrip without loss in the relative scaling for the frequency band (e.g. the band would not be shifted downward due to the longer wavelengths). However, the dimensions, and thus variables and coefficients, in the code were scaled in centimeters and that convention was kept throughout - though it may now be considered an arbitrary choice. Additionally, as explained in Chapter 1 the impedance was set at approximately 30 ohms in the *quasi-static* regime for *practical* purposes. However, this value too was deviated somewhat to illustrate the possible effects that grading the dielectric would have on the dispersion of the microstrip structure. By increasing the static permittivity constant $\epsilon_r$ from around 4 to 12 a larger dispersive effect could be realized. A larger permittivity provides for a more pronounced dispersive effect and is indicative of higher permittivity material substrates such as Alumina. However, this again could have been done with plotting functions without loss in generality and could also be considered an arbitrary choice at this point. The larger permitivity also tends to shift the frequency band downward for $\epsilon_{eff}(f)$ due to a longer wavelength and slower phase velocity for the signal. As discussed previously the frequency band of interest is primarily the *x-band* for microwave propagation. For a practical application of the method, this is likely to be in the 5 to 40 Ghz range. From examination of the dispersion properties of the microstrip, this is effectively the region below the inflection point of the $\epsilon_{eff}(f)$ vs. frequency curve. Thus, for any given dispersion curve, we need only focus on this region of the curve to determine the effects on dispersion.

As the frequencies increase beyond this inflection point, other modes begin to couple [34] which then distort the signal and thus negate the usefulness of the method. Typically, these modes have cutoff frequencies which are higher than the inflection frequency for the fundamental mode but this is not always the case. Using Edwards [10] we may compute the frequency in which the lowest order mode (in this case the lowest order TM mode wave is the one of interest [10]) starts to couple into the microstrip structure for the dimensions of interest.

$$f_{c[TM_1]} \cong \frac{75}{h\sqrt{\epsilon_r - 1}} = 5.65GHz \tag{2.51}$$

This was computed for the enlarged structure that we have chosen for the analysis which is above the inflection frequency for most of the structures we are interested in. For a practical implementation of the microstrip structure this value is slightly greater than 100 Ghz. Thus, modal coupling for this approach should not be a concern for the introduction of this dispersion compensation methodology.

The boundary conditions for the analytical domain were chosen to be metallic rather than continuous. This again was done for computational efficiency. If the domain size is chosen large enough [6] relative to the microstrip dimensions themselves (approximately 10-20 times larger than the strip width), then the results will yield relatively accurate results as compared to an open microstrip structure. The microstrip structure is also symmetric about the axis and thus for analysis only half the domain need be used. However, identification of the proper eigen-modes requires plotting the fields across the entire domain in many cases. Thus, it was decided to analyze the full domain space rather than half of it for this reason. The dimensions used for the analytical domain are shown in table 2.1.

Table 2.1: Dimensions of Analytical Domain for Microstrip Structure (all dimensions in centimeters).

| Trace Width | Trace Thickness | Dielectric Thickness | Box Width/Height |
|---|---|---|---|
| 1.6 | 0.08 | 0.4 | 16/8 |

The mesh generation for the analytical region is also an important consideration in the development of the solution. The mesh size is variable and also impacts the accuracy of the solution especially in regions where the field intensities are high. Mesh generation and accuracy therefrom is discussed in subsequent sections.

### 2.4.2 Considerations in Tool Usage and Code Development

#### 2.4.2.1 Mesh Generation

To solve the PDE's using the finite element method, requires a mesh be created in the geometrical analytical space. Rather than develop a home-grown mesh generator, the one provided by Matlab's PDE Toolbox was used. The PDE Toolbox mesh generator uses an adaptive *Delaunay* algorithm to create the mesh structure [46]. Near corners and small geometries where the fields are typically highest, the algorithm creates larger numbers of smaller meshes for accuracy. The mesh generator also is programmable to the number of meshes that may be required for the problem. This allows for greater accuracy and ease in programmability as will be seen in subsequent sections.

The main limitation with the mesh generator is that maintaining a constant mesh density and number across different structures of the same size (as in changing the domain sizes in a step-graded microstrip) is not possible. This is because the mesh grows outward from the domain boundaries and if the physical size of the domain changes in any way, the mesh construction for that domain - and thus the overall structure is changed. This causes difficulty when one wishes to analyze one structure versus another and then make very close comparisons between them. The reason being is that the accuracy of the solution is also dependent upon the mesh density and size and thus it is difficult to make comparisons of $\epsilon_{eff}(f)$ from one construction to another. This limitation was mostly overcome by making minor adjustments to the mesh between constructions to get better approximations and reduce the overall error as much as possible. In the end, this did not appear to be a significantly limiting factor in the research.

#### 2.4.2.2 Considerations for Boundary Conditions

The previous and fore coming analyses have assumed *Dirichilet* or *essential* boundary conditions. Because the boundary conditions assumed that the boundaries were homogeneous as well (in this case the strip and the rectangular boundary was assumed to be at *ground* potential) these boundary conditions were applied after the assembly of the coefficient matrices by *zeroing* out the diagonal elements on one side of the eigenvalue equation. As described in [36], this is done by replacing the columns and rows associated with the boundary 'nodes' with zero's as illustrated in the matrix 2.52 below.

$$\begin{bmatrix} C_{11} & C_{12} & .. & 0 & .. & C_{1n} \\ C_{21} & C_{22} & .. & 0 & .. & C_{2n} \\ \vdots & .. & .. & \vdots & .. & \vdots \\ 0 & 0 & .. & 0 & .. & 0 \\ \vdots & .. & .. & \vdots & .. & \vdots \\ C_{(n-1)1} & .. & .. & 0 & .. & C_{(n-1)n} \\ C_{n1} & .. & .. & 0 & .. & C_{nn} \end{bmatrix} \tag{2.52}$$

The row is replaced with zeros because by replacing the corresponding diagonal element with zero yields a linear dependent equation and thus by zeroing out that row the redundancy is removed. In the eigenvalue equation, one of the matrices must be *symmetric positive-definite* which requires the diagonal entries to not be zero. Therefore, the diagonal entries on the right side of the eigenvalue equation have been assigned the value of '1'. A Matlab subroutine was written which replaced the appropriate entries and was called as a function by the main routine. For the microstrip structures where two scalar fields $E_z, H_z$ are simultaneously solved for, only the tangential $E$ fields are set to zero in the matrix equations.

## 2.5 Validation

This section discusses the validation of the method introduced in the previous sections. Most of the examples are based upon a standard microstrip as a baseline since there is a plethora of information and data available on this structure. The validation of the code and the method entails examination of the following aspects of the solution space.

- Identification of the proper *eigen-frequencies* for the $EH_0$ mode
- Comparative analysis between microstrip *structures*
- Convergence and accuracy of solution

As discussed in Chapter 1 the geometry of the microstrip that was analyzed to determine the efficacy of the approach was based upon practical engineering constraints as known at this time. However, for modeling purposes, the geometry and dielectric constant, were changed to better show the method. Specifically, the relative sizes of the microstrip and dielectric region (height) were enlarged relative to the shield boundaries to better aid in analysis of the problem and to increase the convergence time of the code by reducing the number of meshes in the structure. From previous analyses which were discussed in some detail in Balanis [6], it was determined that these changes would not affect the accuracy of the results as long as the ratio of the shielded boundary dimensions to strip width were a factor of 10 or greater.

As an initial check the efficacy of the method and programs developed for the step-graded dielectric problem, some simple waveguides were analyzed using the FEM Matlab based code developed herein. The results (see Appendix A), showed that the code was quite accurate for solving these simple structures. These preliminary analyses helped instill confidence that the investigation of the microstrip structure would yield similar certainty in the results obtained. Thus, the basic microstrip structure was chosen to be the basis of the efficacy of the code for the analysis of the step-graded microstrip discussed in Chapter 3.

### 2.5.1 Identification of Eigen-modes

Because of the number of eigenvalues which present themselves in the numerical analysis it is important to be able to focus on the eigenvalues and eigenvectors (the *z-directed* fields in this case) which represent the mode which is of most interest to this research. That being, the fundamental mode of the microstrip, $EH_0$. This mode is characterized by having a zero cutoff. However, since the fields are *hybrid*, being a combination of longitudinal section electric and magnetic fields ($LSE$ and $LSM$), which couple along the strip, the fields are also complex as compared with the fields that were presented in previous sections without the metal conductor strip present. Thus, it is important that the proper field patterns be identified in order to ensure the correct and accurate plotting of $\epsilon_{eff}(f)$ as a function of frequency.

The fundamental $EH_0$ should result in field patterns which are consistent with the quasi-static mode for the microstrip. Thus, a brief theoretical examination of the static fields gives us an understanding of the $EH_0$ fields for this mode. Figure 2.3 shows pictorially what the $X$ and $Y$ magnetic fields should look like around the dielectric-air and strip region of the microstrip for the static case. If propagation is into the page in the $Z$ direction then the magnetic fields should follow the path on the ellipses as shown. On the *left-hand* side of the strip the magnetic field $H_y$ is positive and reaches a relative maximum near the microstrip left edge. As one moves toward the center of the strip $H_y$ decreases and crosses through zero at the center of the strip. $H_y$ hits a relative minimum near the *right-hand* edge of the strip. Thus, $H_y$ is *anti-symmetric* about the axis of the strip as shown on the magnitude plot. On the other hand, $H_x$ hits a relative maximum around the left and right-hand sides of the strip and is *symmetric* about the strip. Obviously, there is no $Z$ directed field in the static or quasi-static case.

Analysis of the fundamental $EH_0$ mode for microstrips has been an important research topic even prior to 1970. In 1972 R.P. Wharton [55] analyzed the dominate mode for a similar boxed microstrip structure using the finite difference method.

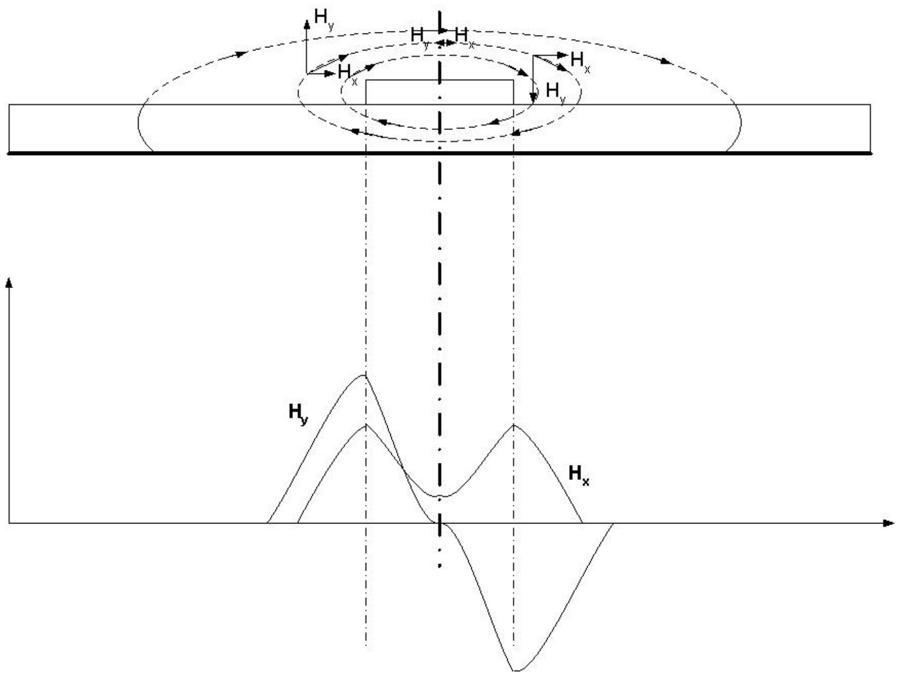


Figure 2.3: Pictorial representation of the $X$ and $Y$ fields for the static case to aid in identifying the fundamental $EH_0$ mode fields.

His main objective was to identify the correct $x$-$y$ directed fields for the lowest order mode and to verify the analysis thru experimentation.

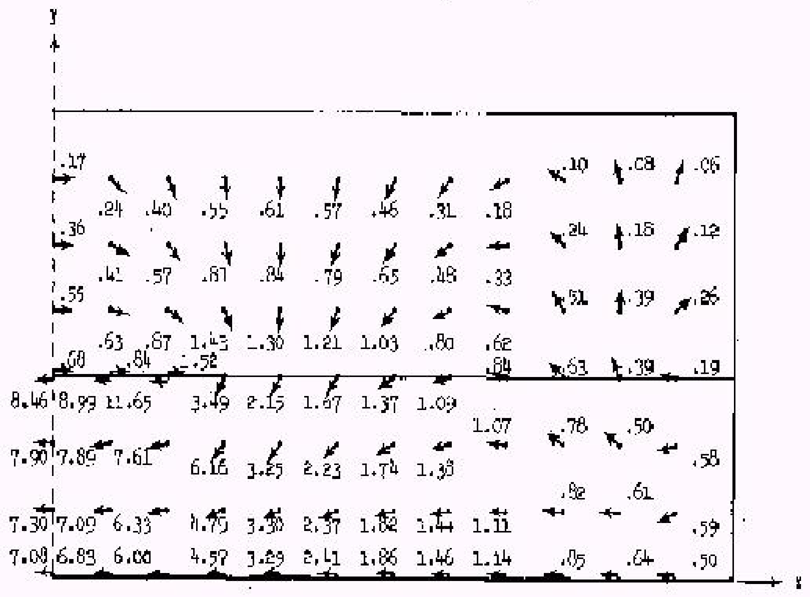

Fig. 3. Transverse magnetic field distribution of the dominant microstrip mode on the 0.055-in alumina substrate at 10.63 GHz.

Figure 2.4: Wharton's [55] results of the transverse magnetic fields for a microstrip structure with alumina as the substrate and a width to height ratio of 2 for the microstrip structure.

Figure 2.4 shows Wharton's results for the *transverse* $H_x$ and $H_y$ magnetic fields for a microstrip structure with a dielectric region permittivity of $\epsilon_r = 9.5$. Note the relative directions of the magnetic field plots (e.g. the *flow* direction of the arrows). Also note that only a portion of the region is plotted due to the symmetry of the

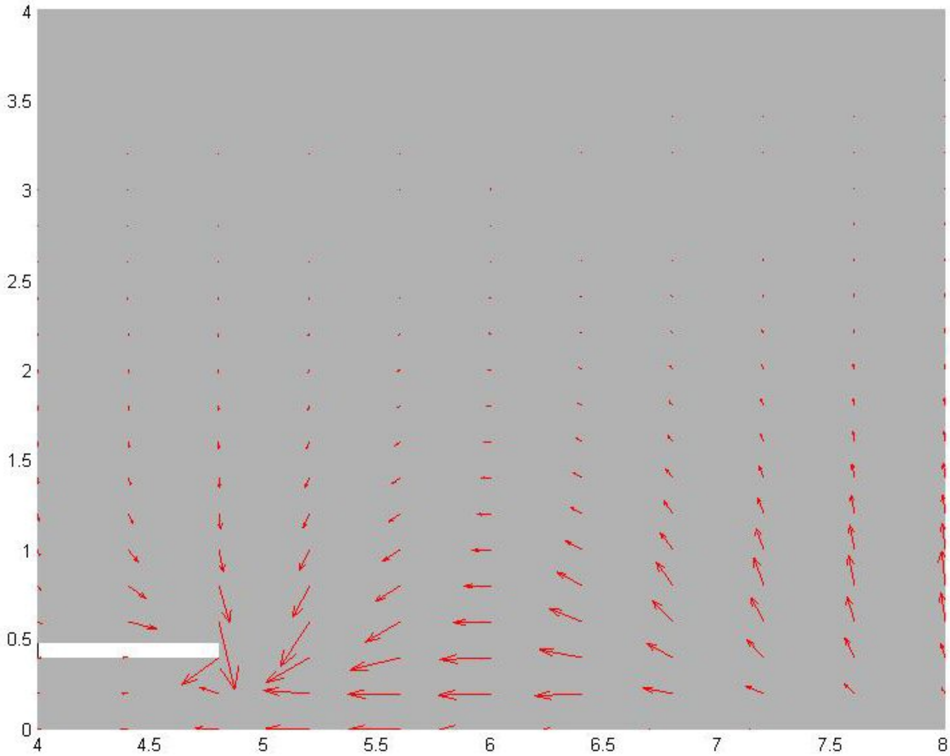


Figure 2.5: Quiver plot of xy-directed magnetic fields for right side of small 'boxed' microstrip structure using 507 meshs, vp=0.95e8, f=2.07 Ghz.

problem (half of the microstrip trace egresses out into the plot region from the middle left). As stated, the microstrip trace has essentially zero thickness which was the assumption in Wharton's analysis. Figure 2.5 shows a similar plot using the finite element code developed herein for a similar microstrip structure. The geometries, permittivity, and frequency are slightly different (particularly the size of the 'box' region which is larger in the case of Wharton's analysis) but the modes of the two structures are the same. The microstrip trace for the case study herein has a finite strip thickness that can contribute to some of the differences in the fields for the plot as well. Note the similarity in the direction and concentration of the vector field plots. The *flow* of the fields and the direction of the arrows in the relative regions - such as near the end of the strip - in each case are very similar. Only near the right boundary of the structure do the arrows appear to diverge. This is believed to be due to the larger size of the region analyzed by Wharton (e.g. larger number of wavelengths in region due to relatively larger 'box' size).

More revealing are the relative magnitudes of the fields along the dielectric-air interface. Figure 2.6, as reported by Wharton, shows the magnetic fields for the structure reported in [55] for the right half side of the microstrip structure. Figure 2.7 shows the fields for the structure analyzed within this report which were created using a plot subroutine developed for plotting the electromagnetic microstrip field patterns. Figure 2.7 shows the magnetic field intensities along the

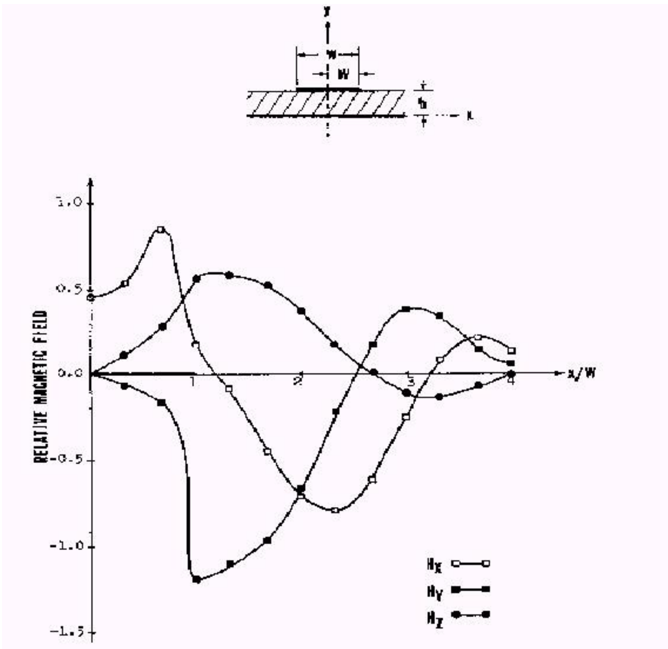


Figure 2.6: Relative magnitudes of the magnetic fields along dielectric-air interface of RHS of microstrip structure as reported by R.P. Wharton [55].

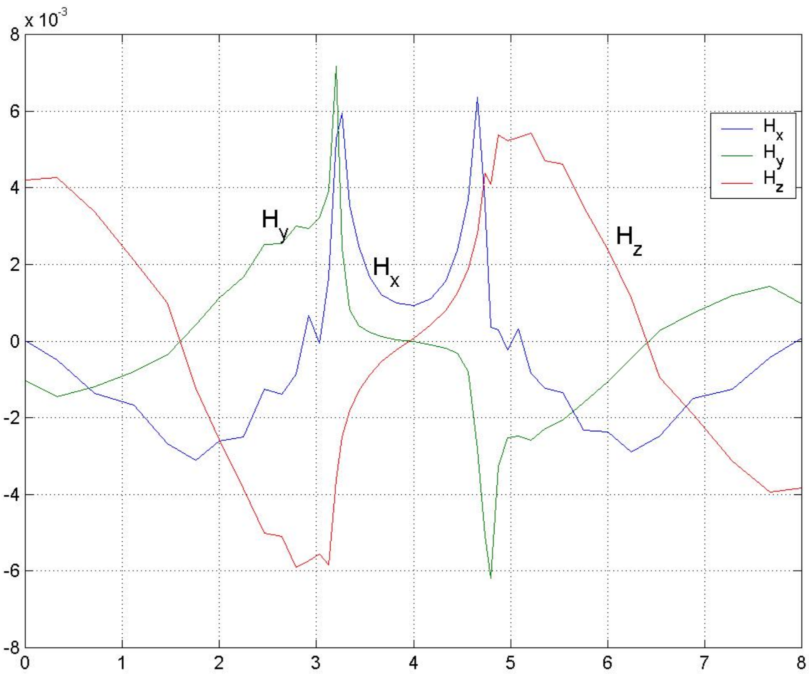


Figure 2.7: Relative magnitudes of the magnetic fields along dielectric-air interface for microstrip structure under analysis in this section.

entire dielectric-air and conductor-air interface (top side) for the boxed structure shown in Figure 2.8. The microstrip is centered in the region from 3.2 to 4.8 in the $x$ dimension. For the quasi-TEM approximation where the wavelength of the signal is relatively large compared to the strip dimensions, one would expect that mostly longitudinal currents to exist along the strip. For the simulations and microstrip structure modeled herein, the wavelength is numerically computed to be 4.6 cm with the strip width being 1.6 cm. Thus, the structure is approaching electrical lengths on the order of the geometry of the strip width. However, for analytical purposes, one may still use the previous static assumptions to get a relative understanding of the fields along the interface. Assuming primarily longitudinal currents along the strip, the tangential magnetic fields ($x$-$z$) will be discontinuous across the strip and for a PEC (*perfect electric conductor*), the normal component $y$ will approach zero. It may be seen in the figure that the normal component of the magnetic fields $H_y$ are close to zero along the strip top surface, which is consistent with the *quasi-static* theoretical approximation for the electromagnetic field patterns. As expected, though, the field density approaches infinity (or a large value in the case of the numerical analysis) in the limit at the corners and shows a very large spike in all cases. If the direction of current is only in the positive $z$ direction one would expect - from using the right-hand rule - that the vector field intensities for $H_x$ and $H_y$ to be *positive* and *negative* respectively close to the strip on the

RHS of the structure as previously predicted 2.3; for an elliptical closed loop field path. As shown in the Figure, this is indeed the case. Additionally, the LHS shows field intensities that indicate currents flowing in the *positive* $z$ direction where $H_x$ and $H_y$ are both *positive*. Thus, $H_x$ is symmetric across the strip and $H_y$ is *anti-symmetric*. This is consistent with longitudinal currents flowing into the page on the top side of the strip in the positive $Z$ direction. Thus, it is clear that the proper eigenvalue for the $EH_0$ mode has been found and is consistent with Wharton's results. The only subtle differences in the curves are due to the differences in the geometries of the structure. For the most part, the relative shape of the field magnitudes are remarkably similar. Wharton [55] also reported corroboration of his results using a YIG sphere which confirmed his numerical analyses which is further evidence that the code has correctly extracted the correct eigenvalues for the $EH_0$ mode.

### 2.5.2 Comparative Analyses

As part of the validation process, the results from the FEM code were compared against closed form expressions for unshielded microstrip structures. Though the results will not be exact this is a necessary step towards verifying the accuracy of the approach. Because of the capacitive coupling to the shield walls, it is expected that in the *quasi-static* regime the value for $\epsilon_{eff}(f)$ should be lower for the shielded microstrip than for the *open* structure. An illustration of this coupling effect on $\epsilon_{eff}(f)$ is given in the next section and comparisons are made with closed-form expressions for $\epsilon_{eff}(f)$.

#### 2.5.2.1 Variations in Shielded Microstrip Structures

The frequency dependent permittivity $\epsilon_{eff}(f)$ can vary as a function of the shield dimensions. From a modal perspective, a microstrip placed in a shielded enclosure is similar to the partially-filled dielectric waveguide, except that it does not support pure *LSE* or *LSM* modes due to the coupling of the two modes at the microstrip trace. Currents flowing longitudinally along the strip tend to couple these two modes making the final mode hybrid. As described in section 2.5.1, the lowest order mode in lower frequency band (e.g. *quasi-TEM*) has a zero cutoff frequency and is the main propagation mode of interest for this analysis and thus we are interested in plots of $\epsilon_{eff}(f)$ as a function of frequency.

The computed frequency components (eigenvalues) will have associated *z-directed* electric and magnetic fields (eigenvectors) which may be used to determine the correct eigenvalues. The results should indicate a concentration of field density distribution underneath the strip as the frequency in the microstrip waveguide increases.

Figure 2.8 shows a cross-section of the structure (triangle elements also shown) which was used to analyze a somewhat smaller microstrip structure than what

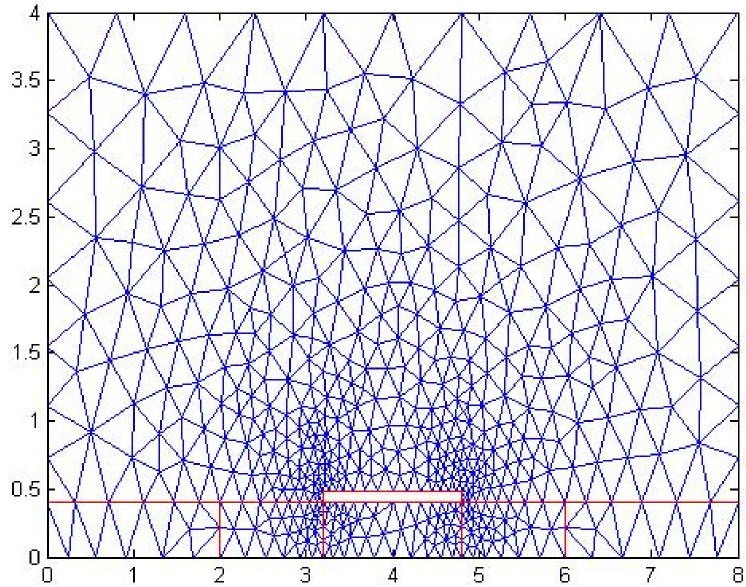


Figure 2.8: Cross-section of mesh structure (924 triangle elements) for 'small' microstrip structure.

was analyzed for the *step-graded* structure. The *frequency-dependent* permittivity $\epsilon_{eff}(f)$ - which is our $FOM$[5] - may be determined from the phase velocity of the signal [10, chapter 4, equation 4.1],

$$v_p = \frac{v_c}{\sqrt{\epsilon_{eff}(f)}} \Rightarrow \epsilon_{eff}(f) = \left(\frac{v_c}{v_p}\right)^2 \tag{2.53}$$

where $v_c$ is the speed of light in air and $v_p$ is the phase velocity of the wave. As previously discussed, the frequency dependent permittivity $\epsilon_{eff}(f)$ will asymptote to the *quasi-static* effective permittivity $\epsilon_{ef0}$ at lower frequencies. This asymptotic value may be approximated either through examination of the finite element code results in the lower frequency regime (using a closed form expression such as one found in Edwards [10]) or through numerical analysis with the method outlined in section A.1. Using a mathematical expression for computing $\epsilon_{ef0}$ [10], this value was determined to be approximately 9.3 with the given geometry and the dielectric constant value $\epsilon_r$ of 12.0 in the dielectric region. Using an FEA program developed for this computation the value was determined to be slightly less than 9.0. As predicted, the reason for the disparity is mostly due to the closed-form expression being derived empirically for an 'open' rather than a 'closed' structure where the capacitive coupling to walls contributes to the lower value of $\epsilon_{ef0}$.

It is possible now to plot $\epsilon_{eff}(f)$ for different sized structures to determine the effects of changing the shield dimensions. Figure 2.9 shows $\epsilon_{eff}(f)$ for two different

[5]Figure of Merit

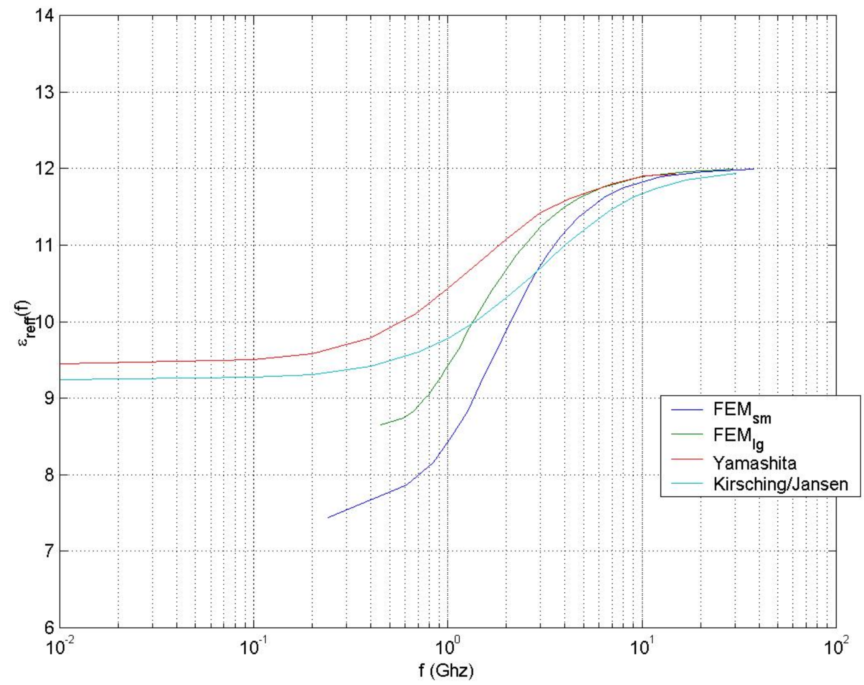


Figure 2.9: *Frequency-dependent* permittivity $\epsilon_{eff}(f)$ as a function of frequency plotted for two different microstrip 'box' sizes ($FEM_{735}$-large box, $FEM_{507}$-small box) and for two closed form expressions (Yamashita and Kirsching & Jansen).

box sizes using the same mesh growth rates (1.18)[6] as well as two well known closed form expressions (the closed-form expressions will be discussed shortly). It is intrinsic to the modeling that the larger box structure should have $\epsilon_{eff}(f)$ *quasi-static* values which will be closer to the open structure. Note that the lower frequency values tend to an asymptotic value which is closer to the predicted *open* microstrip quasi-static value for the larger boxed structure. Thus, as expected, the larger the box size (all else being equal), the more closely the results will approach an *open* structure. This indicates that the code is predicting accurately the trend that we expected - this being, the larger the shield dimensions, the closer $\epsilon_{eff}(f)$ will asymptote to the value for an open microstrip structure.

The two closed-form expressions chosen herein were based upon work by Edwards [10] who did a thorough study of the accuracy of these methods. Both expressions were coded up in Mathcad for ease in computing and then the results plotted in Figure 2.9. Edwards indicated that the formula derived by Yamashita is somewhat inaccurate in the lower frequency regimes. Using a separate expression [10] to compute the asymptotic value of $\epsilon_{ef0}$ it appears that the Yamashita expression indeed in this regime is slightly less accurate than the expression from Kirsching & Jansen [21]. The computed value for $\epsilon_{ef0}$ was around 9.0 whereas the

[6]The growth rate dictates the size of the mesh in the regions of the structure and thus will help to minimize comparative errors due to triangle mesh size differences in critical areas around the microstrip which can affect the numerical results in both the eigenvector and eigenvalue computations. Section 2.4 explains the methodology used for mesh generation.

Yamashita [56] formula (shown in *red*) asymptotes to around 9.5. Note that both of the FEA curves tend to be lower in the asymptotic range than the closed-form expressions - also as predicted. However, all of the methods accurately predict $\epsilon_{eff}(f)$ asymptoting to the dielectric region permittivity $\epsilon_r$ value of 12.0. In the dispersive and higher frequency regions, there appears to be more variability between the methods. The electric field coupling from the strip to the shield walls will have a tendency to *reduce* the solution for the eigenvalues (frequencies) solved for in the equation for a given phase velocity. Thus, for the dispersive portion of the curves, we would expect that for a given permittivity, the actual frequency component should be *lower* for a shielded microstrip. When comparing the FEA results (for the larger structure) against Kirsching & Jansen's empirical formula, this appears to be the case for much of curve. However, it is somewhat difficult to analyze all of these artifacts based upon the curves in Figure 2.9 due to the number of factors involved; mesh size of FEA runs, geometry, etc. Nonetheless, the data does indicate that the code is yielding reasonable results. The next section discusses more details concerning the accuracy of the method and the convergence thereof.

#### 2.5.2.2 Discussion of Wavevector $k_z$ for $EH_0$ mode

The purpose of this section is to briefly discuss the shape of the wave vector for the $EH_0$ mode for the microstrip waveguide. As in the previous sections, direct comparison's with previous work from other authors is difficult due to geometrical and material differences. However, basic shapes and trends still apply since the comparisons are with actual microstrip structures. The wavevector $k_z$ for the lowest order mode is a common figure of merit used by many authors in the discussion of dispersion for microstrip structures. It is typically plotted in a normalized fashion over a defined linear frequency band as in Bagby [4] and is normally flat in the higher regime. As shown in in the top plot in Figure 2.10 this trend is evident as well. The frequency band of interest for the analytical domain corresponds roughly to within the 5 GHz regime. This is shown in the middle plot of Figure 2.10. Note the small inflection in this region which according to Bagby is evident due to the smaller wavevector near the *quasi-static* region of the frequency band.

Though the above figure has not been compared against similar structures the plotted data is indicative of what we would expect for this mode. We expect the wavevector $k_z$ to tend towards zero as the frequency also goes to zero. This may be seen in the dispersion relation below.

$$f_c = \frac{c}{2\pi}\sqrt{\frac{(k_{xod})^2 + (k_{yod})^2}{\epsilon_r - 1}} \tag{2.54}$$

where $c$ is the speed of light, $k_{xod}^2 = (k_{xo}^2 + k_{xd}^2)$ and $k_{yod}^2 = (k_{yo}^2 + k_{yd}^2)$ - the phase constants orthogonal to the direction of propagation. The phase constants in the $x, y$ directions may be different due to the field quantities being different in the modal solution.

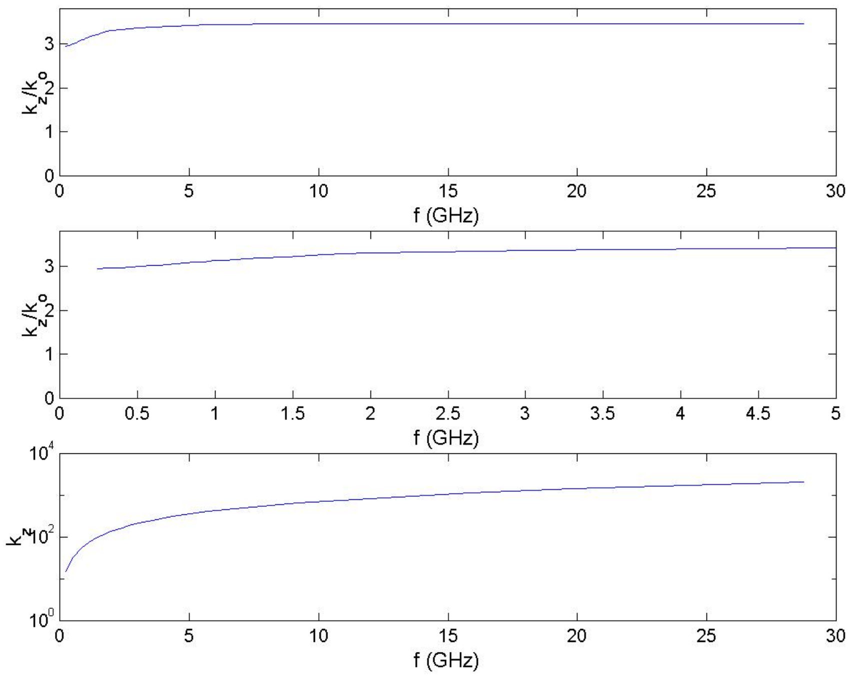


Figure 2.10: Plots of wavevector $k_z$ for 2700 node microstrip structure ($\epsilon_r = 12$). Normalized $k_z$ full frequency band (top plot), frequency band of interest (middle plot), Un-normalized $k_z$ (middle plot).

The solution to the equation 2.1 and 2.2 obviously cannot be solved for in closed form. However, examination of the field plots show that in both the $x$ and $y$ directions it is fairly sinusoidal in nature indicating the modal nature of the solutions. Thus, as frequency tends toward the *quasi-static* regime, the $z-directed$ phase constants tend to zero. Thus, for the hybrid mode $EH_0$ we see that the cutoff frequency should also tend to zero. The bottom plot of Figure 2.10 illustrates this.

### 2.5.3 Convergence of Finite Element Code

The convergence analysis involved the examination of the dispersion of the microstrip problem for different mesh sizes. As the dispersion curves get closer and closer together, the solutions should tend to converge. Because of the large computational time required by the analysis it is important to be able to determine the convergence of the code to reduce this time.

Figure 2.11 shows 5 dispersion curves for 5 different mesh sizes for the same geometric microstrip structure. It is clear that as the mesh size increases, for a given $\epsilon_{eff}(f)$, the frequency components tend to move downward. The question is, has the data converged? To determine this we plot the error between the curves as a function of inverse mesh size.

$$\Delta_{ferr} = f[\epsilon_{eff}(f)]^{M_n} - f[\epsilon_{eff}(f)]^{M_{n+1}} \tag{2.55}$$

where $\Delta_{ferr}$ is the difference between the two dispersion curves at a give frequency.

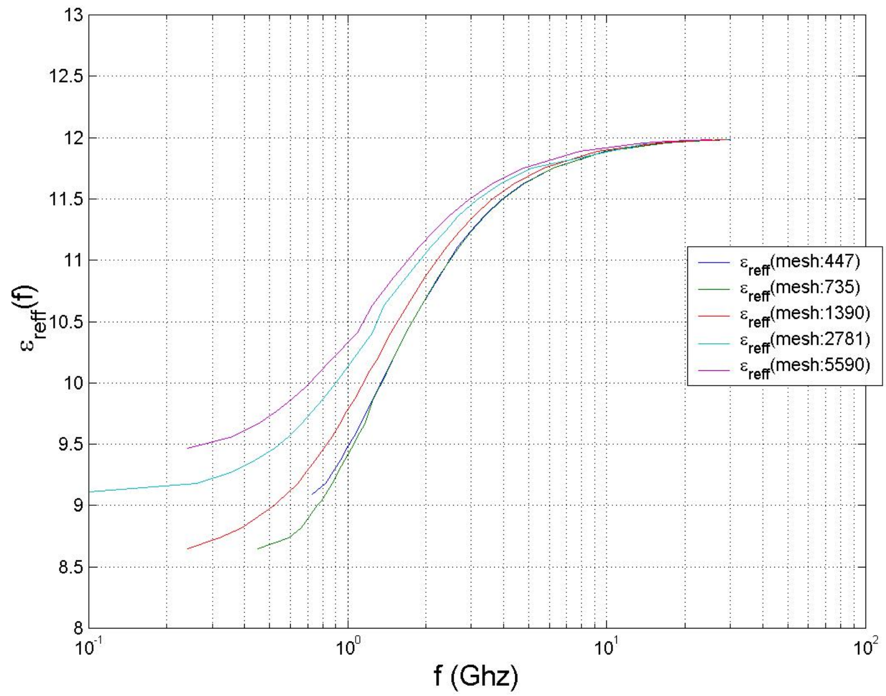


Figure 2.11: Dispersion curves for fundamental *hybrid* mode in a microstrip waveguide for increasing mesh sizes.

And where $M_n$ is the inverse normalized mesh size. Our objective is to determine if the analysis is converging for a given mesh size. Figure 2.12 illustrates the method with actual data.

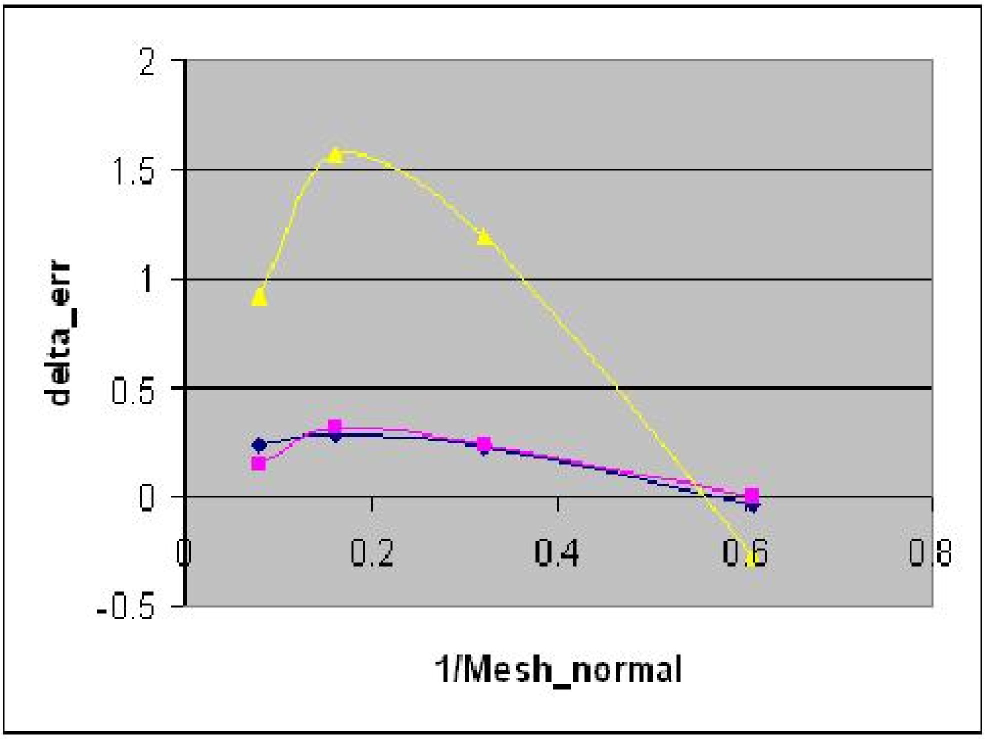


Figure 2.12: $\Delta_{err}$ as a function of inverse normalized mesh size for three corresponding values of $\epsilon_{eff}(f)$.

In examining the results in Figure 2.11, it is clear that two things are occurring: First, that all of curves, the quasi-static limit regions appear to be lower but increasing steadily upwards with mesh size, and second, that simultaneously the dispersion portion of the curves are shifting to the left. However, the main question is does the code converge on a solution for a given mesh size? To answer that, we examine Figure 2.12 which plots three of data points for a given $\epsilon_{eff}(f)$ using equation 2.55. Note that all three curves indicate that the error is decreasing relative to the previous error. The last data points were compiled using a 5590 mesh node size which took approximately 8 days to run. It is clear from this analysis that the code is definitely converging. We can also use this method to determine an extrapolated result should it be necessary. However, this would require at least one more data point at a higher mesh count in order to estimate the *rate* at which the code is converging which would allow us to extrapolate where the error intercepted the x-axis and thus allow us to extrapolate a final dispersion curve for $\epsilon_{eff}(f)$. For now, it is clear that the results indicate the code is relatively accurate from the previous section and that we may conclude that it is converging on a solution.

# Chapter 3

# Results and Analysis

## 3.1 Preliminaries

This chapter deals with the results and analysis of the step-graded microstrip structure. Chapter 2 was a discussion of the method for analyzing the step-graded structure along with validation of the method and code through comparisons with known methods and results. This chapter focuses on how dispersion characteristics may be changed using different permittivity values for the *domains* within a dielectric region for a microstrip. The shielded microstrip structure is used as a baseline and the field plots for different eigenvalues for the $EH_0$ mode along with the analysis of the frequency dependent permittivity $\epsilon_{eff}(f)$ are given as comparisons to the results from the step-graded structures. The first part of the chapter discusses parametric analyses of some step-graded structures and analyzes the frequency dependent permittivity for different cases from the baseline. A discussion on *averaging* effects in the quasi-static regime is discussed along with dispersion shifting. The next part discusses more dramatic changes in the domain regions and shows some simple formulae for computing the effects of dispersion shifting from a quantifiable perspective. From these analyses some general conclusions will be drawn on the efficacy of the dispersion compensation approach and a method for optimizing will be discussed.

## 3.2 Step-Graded Microstrip Analysis

As mentioned previously, the purpose of step-grading the microstrip in the dielectric region is to force the electromagnetic fields into specific regions of the dielectric in an attempt to change the phase-velocity of various frequency components within the frequency band of interest. For the $EH_0$ mode, this means that for signal propagation that the intent is to somewhat align the phase velocity of a *wave packet* of signals to prevent or limit dispersion. From examination of the frequency dependent permittivity of such a structure, this would translate to either a shifting of the curve upwards in frequency - thus limiting the onset of dispersion to a higher frequency band - or changing the effective slope of the $\epsilon_{eff}(f)$ curve. Most of the analyses will show that the dominant effect of changing the domain permittivity values will result in *shifting* of the dispersion the curves rather than changing the slope.

It should be noted that the numerical analyses were run on the same code that was used to develop the dispersion curves in the previous section. For efficiency reasons, the mesh size was reduced to enable generating the large amount of data necessary to create the dispersion curves. Thus, some loss in accuracy from the exact solution is assumed. However, since it was intended to achieve more *relative* accuracy between the curves, this sacrifice in overall accuracy was deemed acceptable.

### 3.2.1 Parametric Analysis of Step-Graded Structures

We first discuss the parametric analysis of a simple step-graded geometry. The dielectric region is broken up into 5 domains each of which may be assigned a different dielectric constant value. The intent is to keep the quasi-static limit the same in all cases of the parametric analysis but at the same time to affect the dispersion portion of the curve. A discussion of the characteristics of the domains in general will be shown later in this chapter.

Figure 3.1 shows the structure under analysis for a crude mesh for clarity. Each *domain* region is assigned a *domain number*. Within each domain the value of the permitivity is forced to vary depending upon the parameterization of the structure. The height of each domain is 0.4 cm. The width of each domain is as follows; domains 1 & 5 (4 cm), domains 2 & 4 (2.25 cm), domain 3 (3.5 cm).

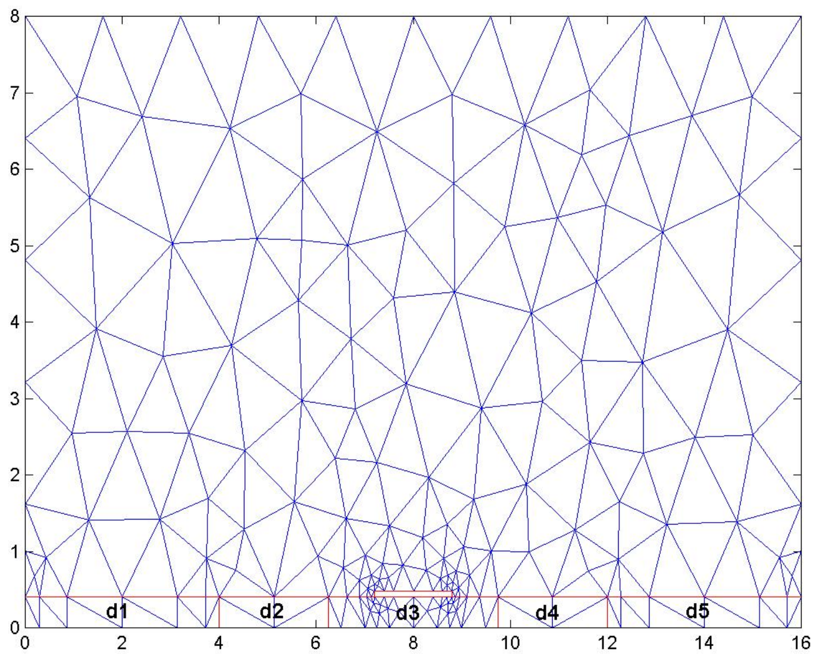


Figure 3.1: Microstrip structure showing domain assignment for analysis.

Because of the symmetry there are only three *domains* that can truly vary; the center (domain 3), middle (domains 2 & 4), and ends (domains 1 & 5). This results in 6 possible combinations to parameterize. The first parameterization of the domain region is shown in Figure 3.2. We first parameterize the center region by varying it from our baseline permittivity of 12 (e.g. $\epsilon_r = 12$ for all domains) to as high as 14. This is illustrated in Figure 3.2. The function $\epsilon_r(d)$ is the value of the permittivity in the domain regions as a function of domain number $d$. The value of the permittivity is constant throughout the region. The baseline structure is the trivial one which would be a straight line function and is not shown for clarity. The first function parameterized is $\epsilon_{r1}(d)$ which increases the permittivity in the center domain (d3) by 0.5 to 12.5 and correspondingly decreases the outer domains (d1 and d5) by 0.5 to 11.5. The middle regions, d2 and d4, are kept constant at the permittivity value of 12.0. Thus, as shown in the figure, this results in a stair-step like function over the dielectric domain region which varies from 11.5 to 12.5. The next function $\epsilon_{r2}(d)$ increments each region that is changing by another 0.5 factor in permittivity and so on until the final function which results in the greatest variation from permittivity of 10.0 to 14.0. The simulation results of this parameterization is shown in Figure 3.3.

The first curve on the graph in Figure 3.3 is the baseline where the permittivity in the dielectric domain regions are held constant at 12.0. The subsequent curves are a result of the changes in the dielectric regions as defined by the parameterization curves in Figure 3.2. All of the curves tend to asymptote towards the same *quasi-static* limit. This is due to the *averaging* affect of the permittivity values in each domain. The average value for the permittivity across the domains is kept approximately at 12.0. This results in the quasi-static permittivity remaining at a consistent value across the parameterized curves as expected. This is due the fields existing throughout the domain regions. Conversely, though, as the

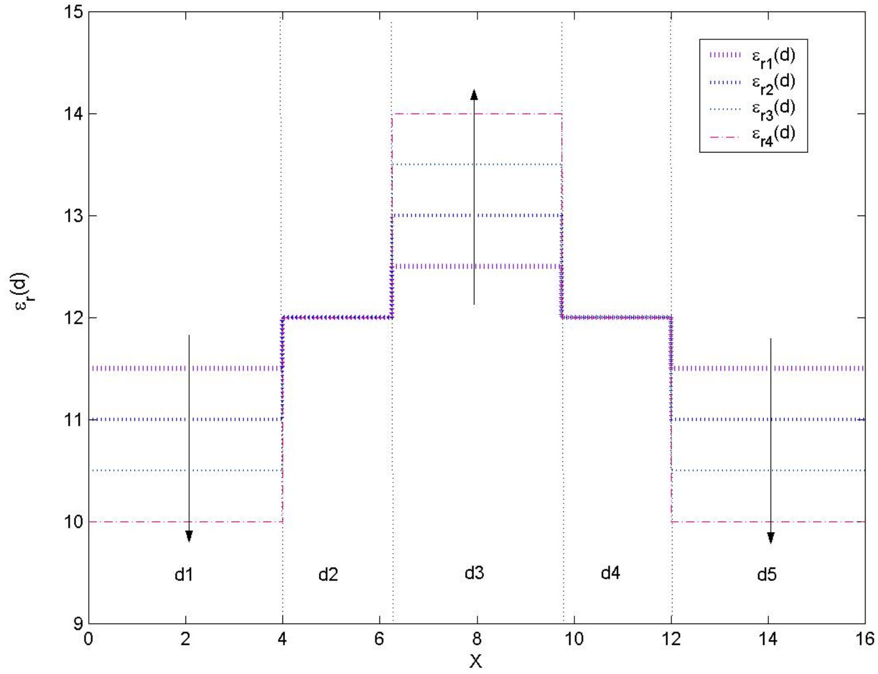


Figure 3.2: Parameterization of dielectric region for analysis of simple step-graded dielectric structure.

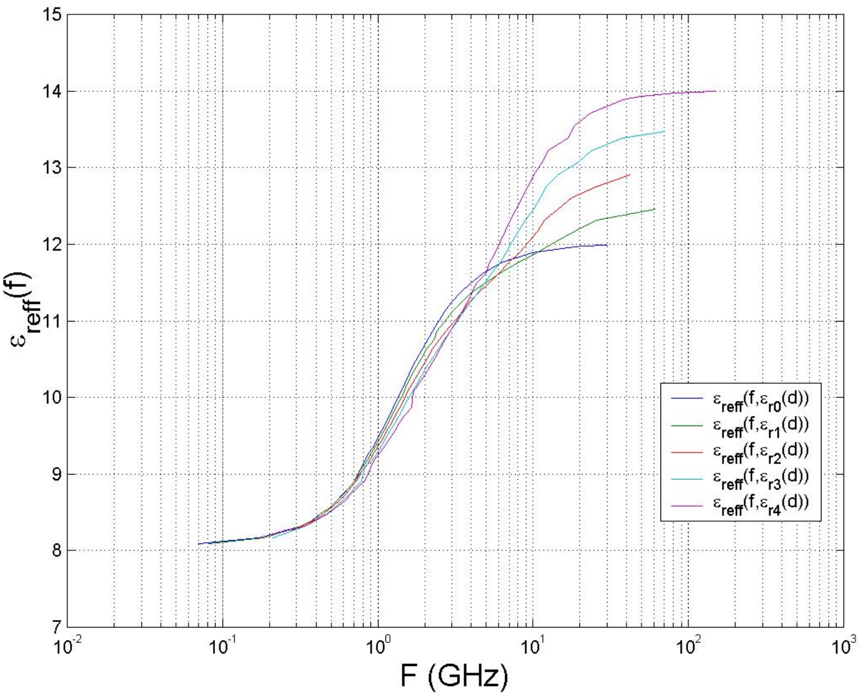


Figure 3.3: $\epsilon_{eff}(f)$ for step-graded dielectric parameterization in Figure 3.2.

frequency increases the fields tend to coalesce or *focus* into the dielectric region of highest permittivity due to that being the region of lowest energy state. Thus, we would expect the asymptotic limit for the plots of $\epsilon_{eff}(f)$ for the $EH_0$ mode to tend towards the domain with the highest permittivity. As shown in Figure 3.3, this indeed appears to be the case. It is clear that all of the curves asymptote towards the highest domain permittivity. The next question is do the fields actually merge into the higher permittivity regions as indicated by the dispersion curves in Figure 3.3?

Figure 3.4 shows a series of $H_z$ plots for the function $\epsilon_{reff}(\epsilon_r(d2), f)$ with select eigenvalues for a portion of two of the curves from figure 3.3. The red circles in the permittivity curve correspond to the magnetic field plots moving from the bottom to the top which are adjacent to the curve. We first note how the magnetic fields in the lower frequency bands tend to exist in most of the dielectric region. However, as the frequency and $\epsilon_{eff}(f)$ increases, it is clear that the fields begin to coalesce inside the regions of highest permittivity as the top plot of $H_z$ illustrates. This is consistent with our prediction that the fields will focus into the regions of highest permittivity.

Figure 3.5 shows results of three different parameterizations where each domain is shifted upwards relative to the others. As shown in the Figure, the other domain values are reduced to balance out the *effective* permittivity or equalize the *quasi-*

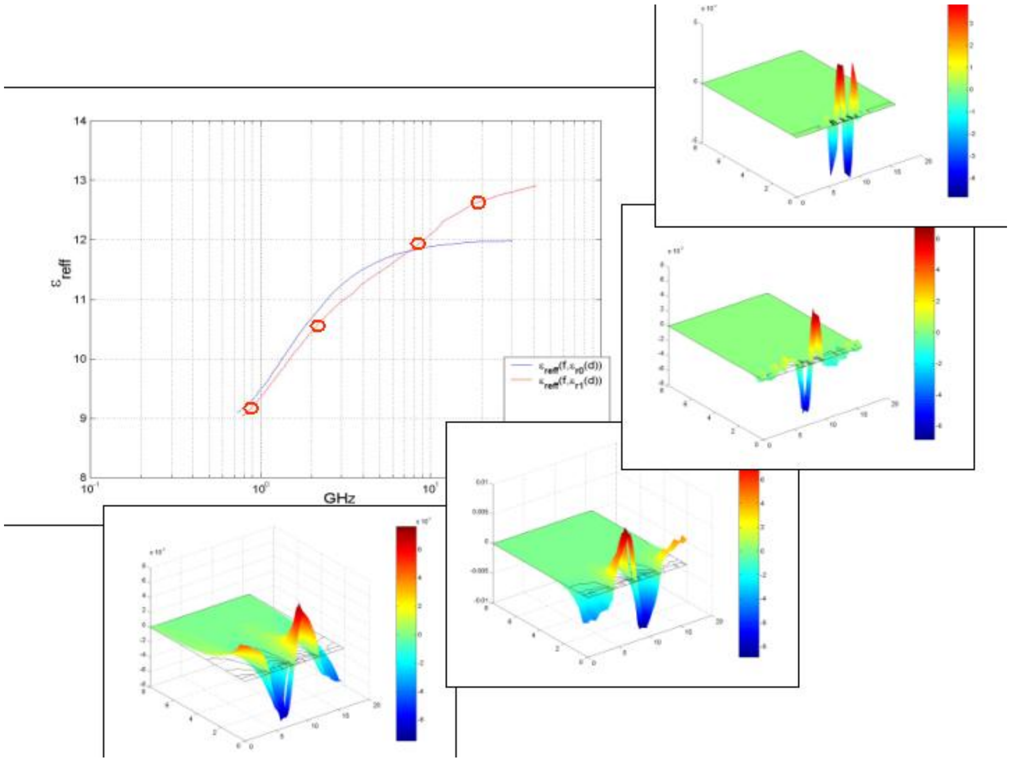

Figure 3.4: $\epsilon_{eff}(f)$ for $\epsilon_{reff}(\epsilon_r(d2), f)$ step-graded dielectric parameterization in Figure 3.2 and select $H_z$ field plots.

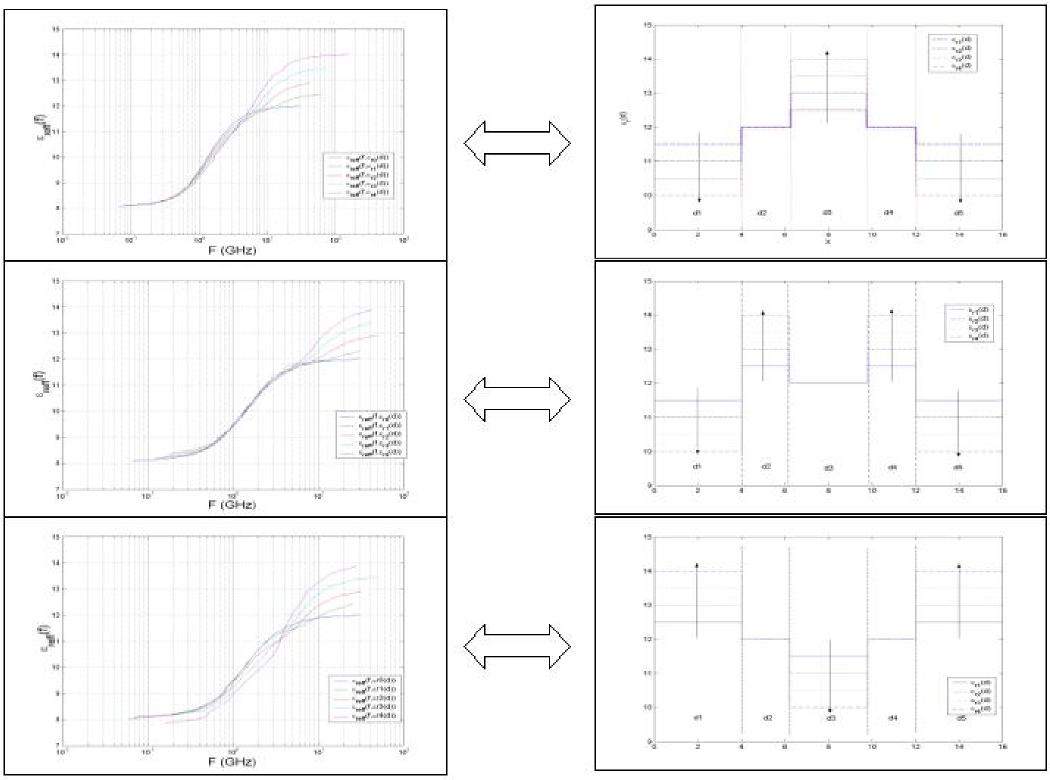


Figure 3.5: $\epsilon_{eff}(f)$ for three different parameterizations of $\epsilon_{reff}(\epsilon_r(d), f)$ step-graded dielectric parameterization where the center, middle, and end domains are parameterized step-wise in a positive direction as the arrows show. Also shown are the domain parameterizations $\epsilon_r(d)$ on the right-hand side of the Figure.

*static* limit. All scales are equivalent for ease in comparing one plot against the other.

There are a few interesting notes to point out in the Figure. First, in the higher frequency regimes, all of the plots asymptote towards the highest value of $\epsilon_r(d)$ for the region which contains this dielectric. This is because as the frequency increases, the waves tend to reflect inside the dielectric region with the highest permittivity - similar to that of a dielectric or copper cladded dielectric waveguide - and most of the real energy is focused towards the direction of propagation; the $z$ direction. Unlike a dielectric waveguide however, the microstrip waveguide has a zero cutoff mode. The strip in the middle forces the existence of a *quasi-static* mode and thus the signal may propagate down to zero frequency across the strip. However, at some frequency, the angle of the wave vector $\vec{k}$, reaches the *critical angle* and full internal reflection is achieved. This is due to the magnitude of $k_z$ increasing relative to $k_x$ and $k_y$ with increasing frequency and thus forcing the angle of the vector to steepen towards the $z$ axis. Moreover, the fields couple into the region of highest permittivity in the high frequency band regardless of the presence of the strip for this mode. This will become more evident in the next section.

Second, in the top plot in Figure 3.5 - which is identical to the plot in Figure 3.3 - note that the portion of the parameterized curves lying below the inflection region (approximately mid-way downward) tend to lie fairly close to each other for parameterizations close to the baseline ($\epsilon_{r0}(d)$), but as the domain region values for $\epsilon_r(d)$ increase the curves begin to slightly *skew* away from each other towards higher frequencies. In the middle plot, where the parameterization takes place in the domains between the center and edge domains, there is virtually no difference in the fields within the inflection region. However, in the third plot, a fairly large difference exists in the parameterization as the curves in the lower inflection region tend to move further to the right. Some of this may be attributable to *averaging* not being perfect for each parameterization in this analysis. That is, the *quasi-static* effective permittivity $\epsilon_{ef0}$, may be lower for one or more of the plots which would delay the onset of dispersion somewhat [43, Chapter 8]. However, this would not explain large shifts in the dispersion from one structure to the next. Figure 3.6 shows this in more detail. This shows a potential for the method to allow for dispersion compensation by *shifting* the dispersion curves towards the right into the higher frequency band allowing for higher signal propagation before the onset of dispersion for a microstrip structure using domain permittivity changes.

Another fascinating effect is the visibility of two slopes in the frequency dependent permittivity curves for the third parameterization. In the larger parameterizations there is clear evidence of two slopes on the dispersion curve where the inflection region is separated - Figure 3.6. These slope changes occur in all cases near the lowest value of permittivity in a domain. This effect is believed to be due

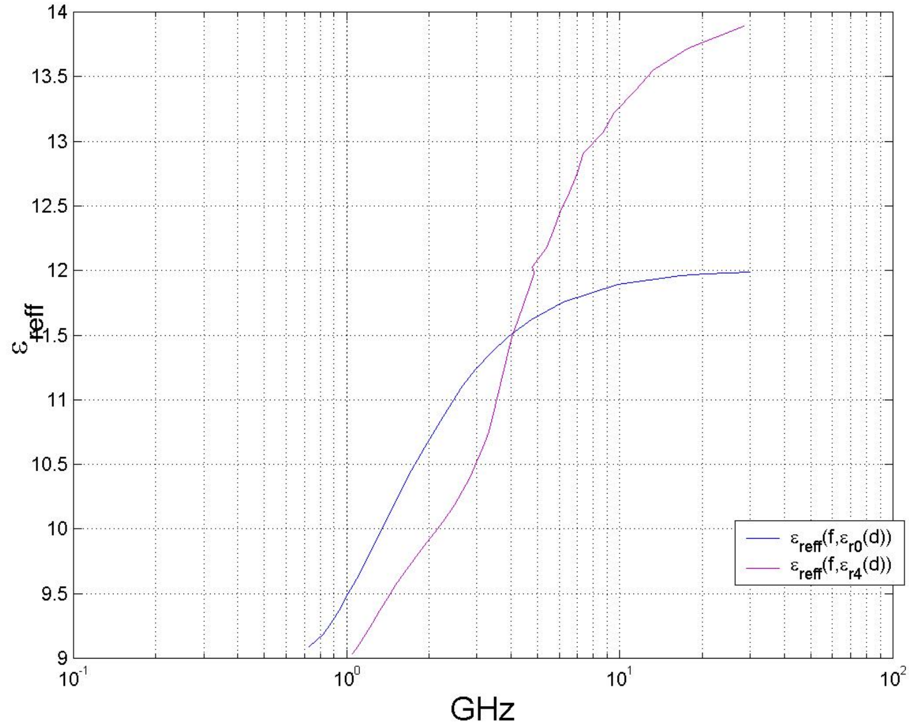


Figure 3.6: $\epsilon_{eff}(f)$ for the first and last curves in Figure 3.5 for the end domain parameterization emphasizing the *dual-slope* effect on step-grading and the shifting of the curve towards higher frequencies below the inflection portion of the curve.

to fields reflecting into the higher permittivity regions at this point and thus an almost *step-change* in the phase velocity occurs in this region of the curve.

A preliminary conclusion appears that by varying the dielectric under the strip towards a lower value but also increasing the outer regions to balance the quasi-static permittivity $\epsilon_{ef0}$, it may be possible to delay the onset of dispersion further and shift the dispersion curves further to the right. The next section analyzes the effects of shifting the dispersion curves outward with larger variations between the dielectric regions.

#### 3.2.1.1 Analysis of Electric & Magnetic Field Plots

From the previous section it was clear that the fields appear to be focusing into the regions of highest permittivity for the first parameterization as shown in Figure 3.4 where the highest permittivity exists underneath the microstrip trace. For completeness, we show plots of the z-directed electric and magnetic fields for select eigenvalues for the other two parameterized cases.

Figure 3.7 shows the electric and magnetic z-directed fields for the *middle* parameterized step-graded case for parameterization $\epsilon_{r2}(d)$ where the variation in domain permittivity from the left-hand side to the center domain is 11-13-12. For the low $\epsilon_{eff}(f)$ case - close to the quasi-static limit - we note that the electric and magnetic fields resemble that for the baseline case (12-12-12). This is to be expected from the previous results in Chapter 2 where the baseline case showed that

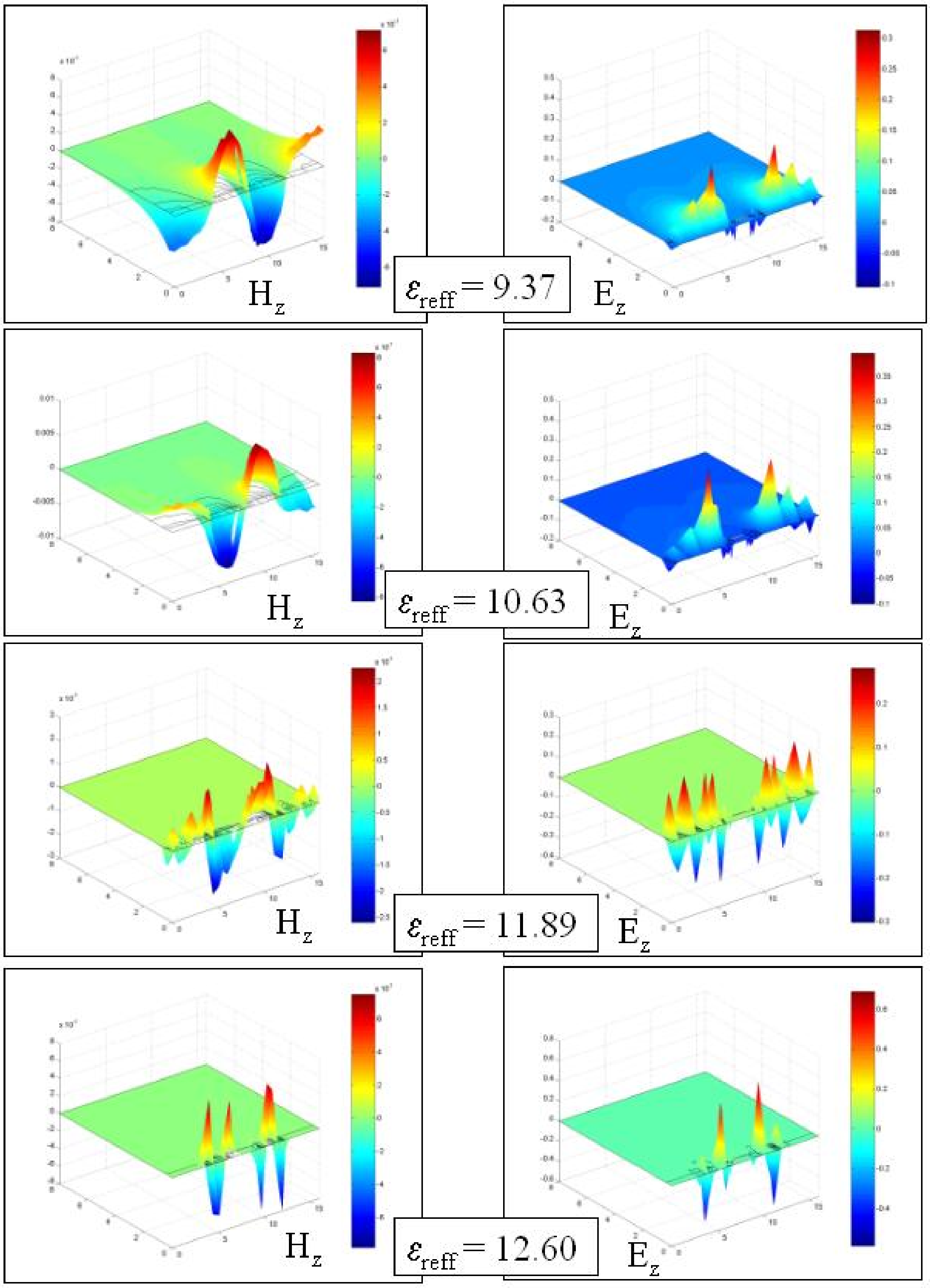


Figure 3.7: $H_z$ and $E_z$ for *middle* parameterized step-graded case for 4 selected eigenvalues with parameterization $\epsilon_{r2}(d)$.

the fields for the $EH_0$ mode revealed a very similar sinusoidal variation. However, as the frequencies increase the eigenmodes for the parameterized case at hand shows that the fields begin to focus into the region of highest permittivity as in the previous section in Figure 3.4, and not under the strip. It is clear for $\epsilon_{eff}(f)$=11.89 the fields are focusing into the middle domain regions and decaying or *evanescent* in the regions outside of this domain. Finally, as the value for $\epsilon_{eff}(f)$=12.60 we see that the fields are almost exclusively in the highest permittivity region - the middle domain regions.

Figure 3.8 shows similar results to Figure 3.7 except the fields are now focused in the end regions where the permittivity is highest. It should be noted that a few of the plots appear to have some anomalies in them particularly for the $\epsilon_{eff}(f)$=11.89 for Figure 3.7 and $\epsilon_{eff}(f)$=9.27 for Figure 3.8. These are due to numerical errors in the modeling due to relatively low mesh density and are believed to be irrelevant.

The high frequency field solutions in Figure 3.7 and Figure 3.8 indicate that due to the coalescing of the fields into the high permittivity regions, the $EH_0$ mode may be supporting other higher order *split* modes where the fields are split on either side. To see this we may solve for the magnetic field solutions for a dielectric filled waveguide where the three sides of the waveguide are perfect magnetic conductors *PMC*, and the bottom is a perfect electric conductor *PEC*. We also give the new waveguide the same dimensions and dielectric characteristics as

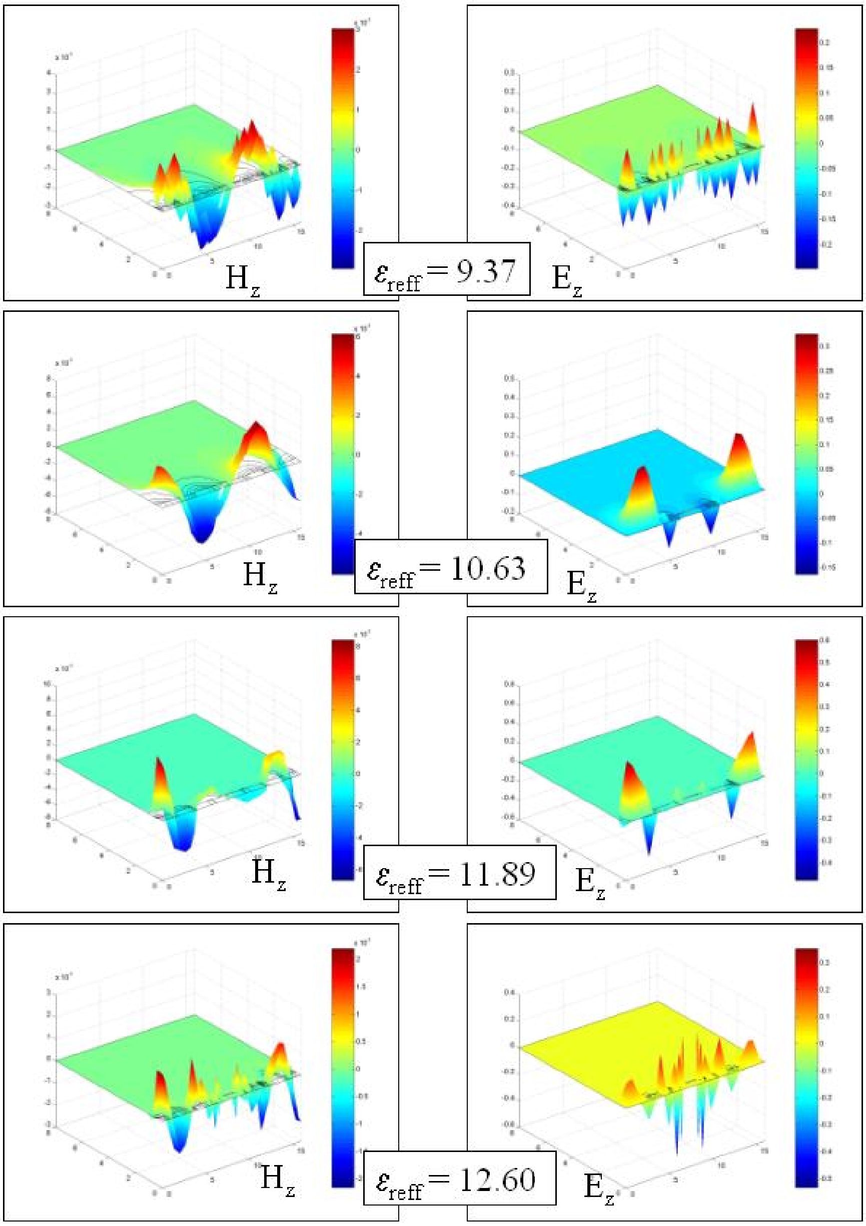


Figure 3.8: $H_z$ and $E_z$ for *end* parameterized step-graded case for 4 selected eigenvalues with parameterization $\epsilon_{r2}(d)$.

that the domain region in Figure 3.7 for the plots in the lower left portion of the Figure. If the supposition is true, we should see that the field solutions for the high frequency step-graded structure should resemble that of a certain mode for the dielectric waveguide. The solution to the *z-directed* magnetic fields for the dielectric waveguide described is given in equation 3.1.

$$H_z = \frac{-jC_3}{\omega\mu\epsilon}\left(k^2 - {k_z}^2\right) sin\left(\frac{n\pi x}{a}\right) cos\left(\frac{m\pi y}{b}\right) \tag{3.1}$$

where $C_3$ is a constant to be determined. Figures 3.9 and 3.10 show the plots of the zoomed in region for the lower left plot in Figure 3.7 and the $LSE^y_{31}$ mode for the dielectric waveguide in question respectively. Note that the field plots are virtually identical in shape. As predicted, the $EH_0$ mode splits into two field solutions which are supported *waveguide* modes at the higher frequencies for the step-grade structure - in this case, the $LSE^y_{31}$ mode is the eventual mode for the dielectric domain regions.

This result indicates that there is fundamental limit to the approach in step-grading the dielectric since the mode is effectively changed in the high frequency regime. However, since this occurs in a region which is far beyond the *quasi-static* limit and even beyond the *inflection* region of the dispersion curve, the approach will still be valid up to very high frequencies.

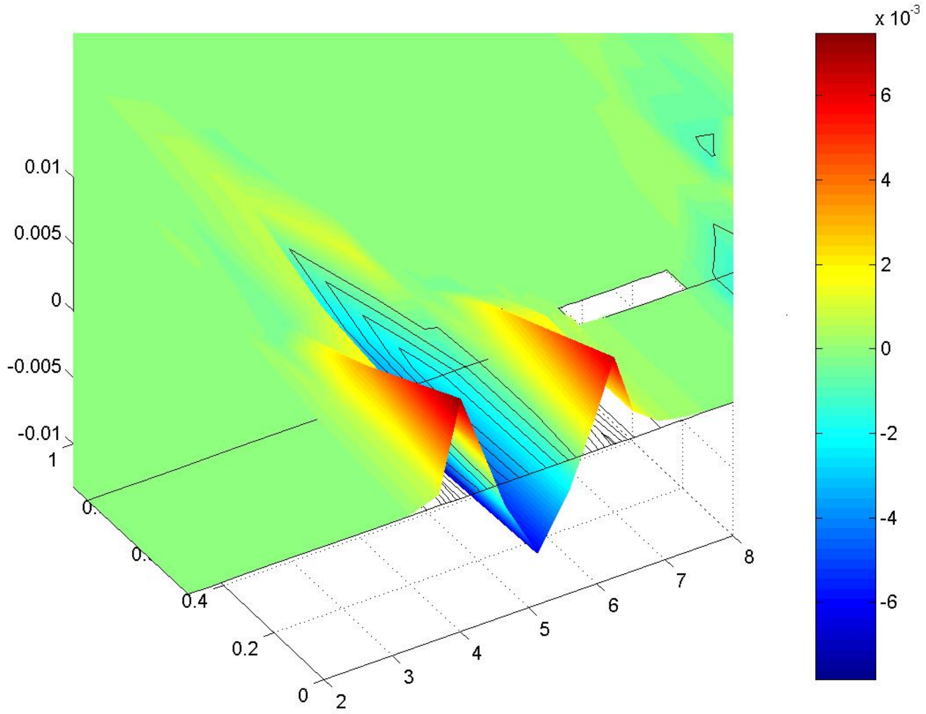


Figure 3.9: Enlargement of left hand section of lower left hand plot in Figure 3.7 for $H_z$.

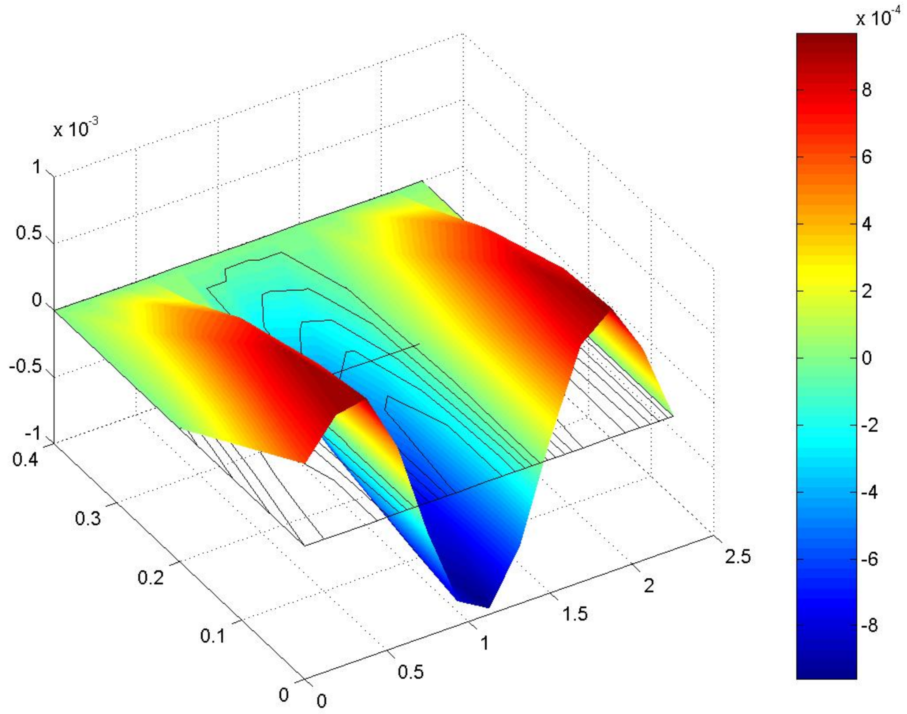


Figure 3.10: $LSE^y_{31}$ mode for $H_z$ for dielectric waveguide.

### 3.2.2 Wide Varying Step-Graded Structures and Analysis

One of the objectives of keeping the *average* of the dielectric domains to be the same was to allow for values of $\epsilon_{ef0}$ to be kept close to that for the standard microstrip with a constant domain permittivity. This would help in communications such as digital signal propagation across a very wide band - from DC to the onset of dispersion - and allow the designer to send signals at frequencies in a higher band across a printed circuit board. Thus, one would be able to use static analysis for much of the design and compute the characteristics of the line from basic empirical equations (such as the impedance of the transmission line) which could be used as well for the step-graded structure. If the average values are different this can create a lower or higher quasi-static permittivity which would change the characteristics making it more difficult to control its behavior.

Thus, in this analysis, to determine the effect from wide domain variations in permittivity, the average values were kept close to the baseline as much as possible. Figure 3.11 shows the variations or *shift* in the dispersion due to wide variations in the domain regions. The domain region under the strip (domain 3) is kept at a value of 8.0. However, the other regions vary from 12.0 to 16.0. Note that there is a fairly large shift between the baseline curve and the other curves from the onset of dispersion. We may assume that dispersion for the baseline begins to become substantial around the 2nd data point or close to 200 Mhz. However, for the black

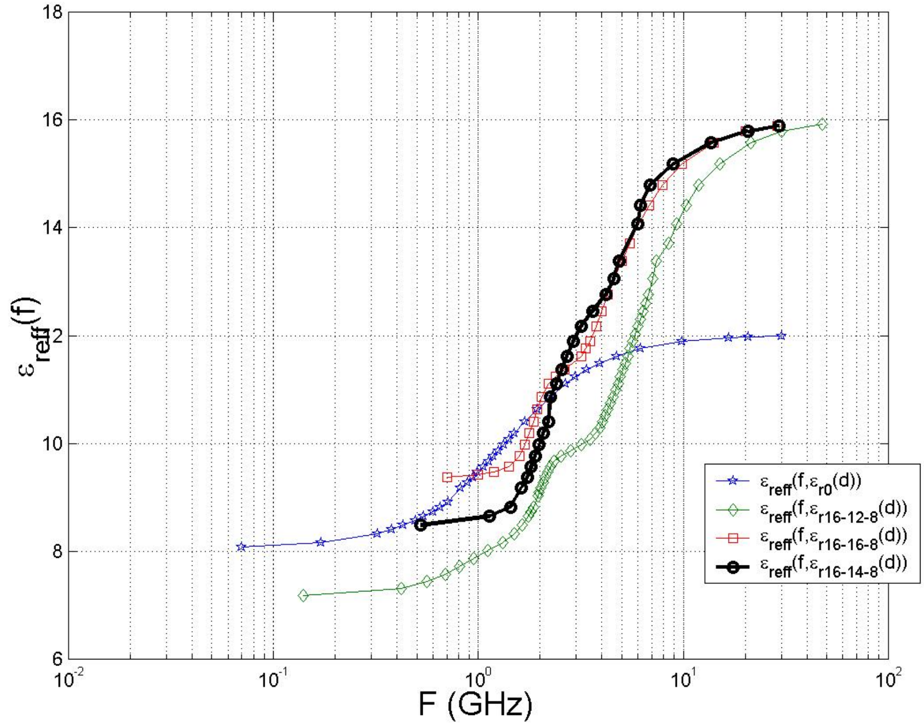


Figure 3.11: Wide variation for $\epsilon_{eff}$ (f)for three dispersion curves where the variation in $\epsilon_r(d)$ is 16-16-8, 16-14-8, and 16-12-8 moving from the ends to the center domain underneath the strip.

curve with domain static permittivity values stepping from end to center of 16-14-8 respectively, the onset of dispersion does not occur until nearly 1.5 GHz! Note that this curve has a similar *quasi-static* permittivity value $\epsilon_{ef0}$ as to that of the baseline whereas the other two are higher and lower respectively. This is due to the lack of perfect *averaging* of the static permittivity in the domain regions. In fact, the process of achieving the 16-14-8 curve was thru an iterative process which honed in on this curve for the quasi-static value. Additionally, we see that in the higher frequency regimes, the curves have more than one inflection region. This was also evident in the smaller variation analyses [1] and in the previous sections but was much less pronounced. These effects appear to be due to reflections in the dielectric domain regions of the electromagnetic fields where large variations between one region and the other occur. The result is a phase velocity shift in the propagating wave which results in a smaller than normal $\epsilon_{eff}(f)$ change due the boundary. The effects due to domain sizing are discussed in more detail in 4.

We can now estimate a *figure of merit* for this affect and get a relationship between the domain variations and the dispersion shift. Using data from Figure 3.5 and Figure 3.11 we estimate the dispersion shift as a function of this variation. Figure 3.12 shows the results of this analysis. The graph shows a plot of the *dispersive shift* as a function of *maximum domain variation*. The graph is nearly

[1] In other words, the ones where the variations between the domain regions was less. For example, all of the analyzes had domain 3 values which were 8.0. In one case though, the 2nd region had a value of 12.0 whereas in another the value was 16.0

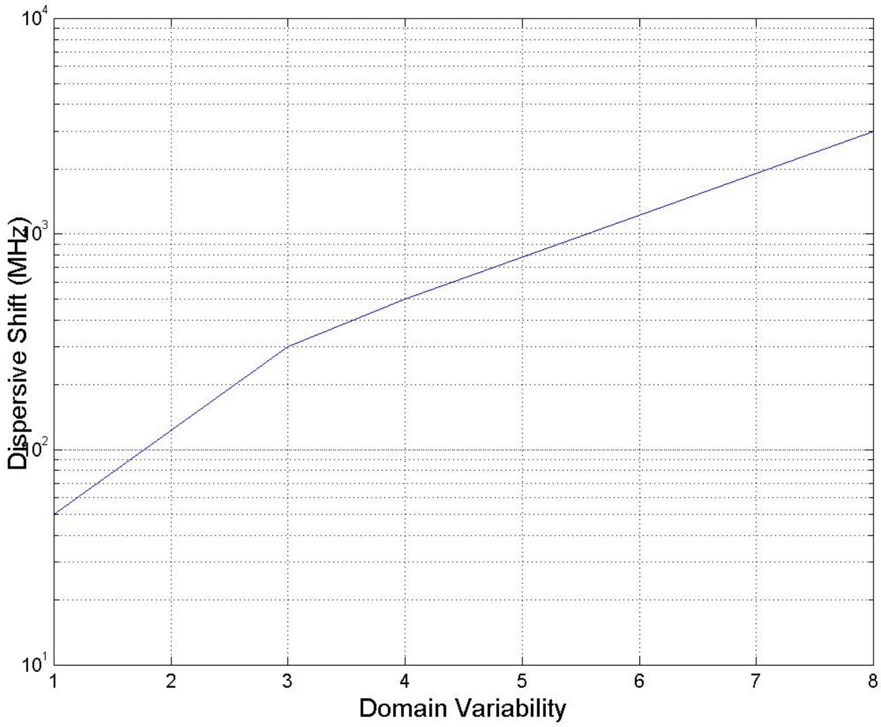


Figure 3.12: *Figure of Merit* analysis for dispersion shift as a function of maximum domain variation. The measurements are made near the inflection points for the curves and are approximations.

log-linear and gives an approximate slope of 1/5 - or 0.2 orders of magnitude for every 1 maximum delta in domain shift. Equation 3.2 describes this dispersion curve shift where $I$ is the frequency at which the inflection point on the baseline curve exists, $\delta$ is the maximum differential between domain static permittivity values and *shift* is the curve shift in MHz from its initial point.

$$Shift = (I)^{0.2\delta} \tag{3.2}$$

The estimate for the formulation would change for different domain sizes and positions but for this structure it appears to be reasonable. A more complex formula would be needed to describe the behavior for these additional affects.

#### 3.2.2.1 Characteristics of Dielectric Domain Regions

Though it will be discussed in some detail in the final chapter 4 as a future research topic a brief discussion of the characteristics of the domains themselves is warranted here. It is clear from this research that the size, placement, and quantity of the domains along with the permittivity assigned to each domain plays an important role in the dispersion characteristics for the step-graded microstrip as a whole. The research herein has been focused primarily on a particular structure - that being 5 domains with the dimensions and position given previously. The reason for focusing the research on just this structure was primarily due to time. It was determined that there were many variations to explore which would affect the dispersion. The quantity, size and position in the *x-dimension* were just a few. Other effects which would need exploring would be $y$ and $z$ variations and also non-discrete domains, that is, *continuous* variations across domains. These are a few of the areas where research is likely warranted. The other affect is quantity - 5 domains were chosen over less or more due to simplicity. A larger number of domains would yield more variations but would also limit the scope of what could be researched due to the number of parametric studies that would need to be examined.

However, just changing the size of the domains yields interesting affects. For completeness then, we show the change in the overall characteristics by simply adjusting the size of the domains on a wide-varying permittivity construction - that being, the 16-14-8 construction. Here we have kept the overall size of the region but have adjusted the $x$ dimensions of the domain regions.

Figure 3.13 shows the microstrip physical change to the domain regions where the one on the left is the old construction. Note that the size of domain region 3 is shown in the black box underneath the domain region for clarity. On the right-hand side is the new construction. Domain 3 has been shrunk relative to the other domains. In fact, the only change is to Domains 2,3, and 4; the outside domains 1 and 5 have remained the same size. We would expect that if the domain permittivities were kept the same, one effect on the dispersion curve would be to

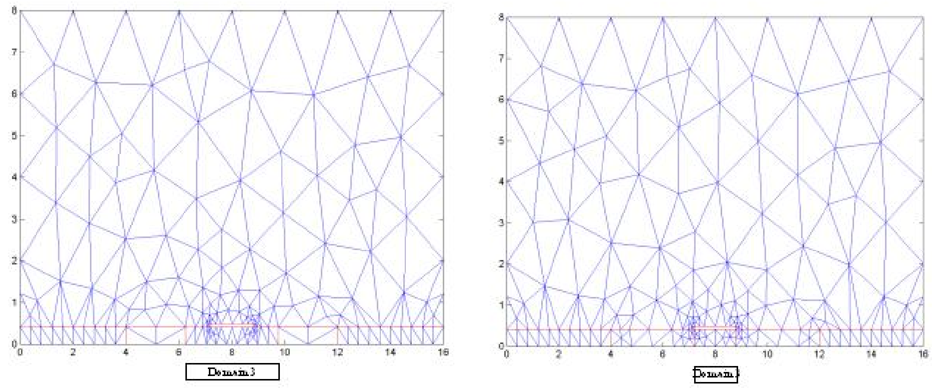

Figure 3.13: Region change between 'old' and 'new' step-graded structures. Note the size change of the domain region 3 underneath the strip. The much smaller region will have the effect (all else being equal) of raising the *averaging* effects in the quasi-static limit as well as shifting the dispersion curve.

change the *averaging* of the domain regions and affect the quasi-static limit. This is indeed the case as shown in Figure 3.14.

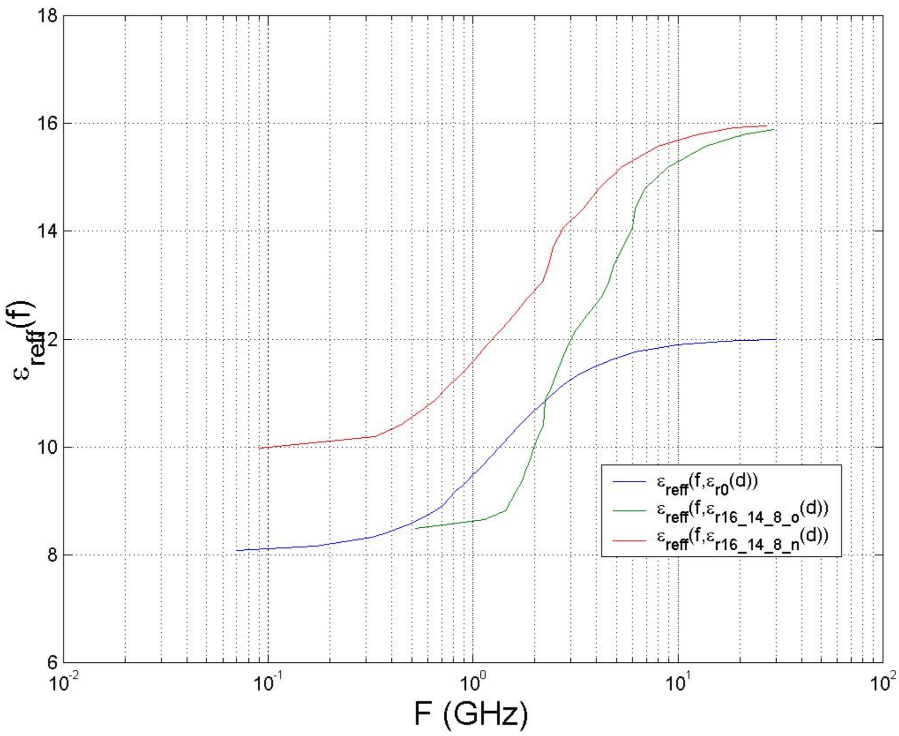


Figure 3.14: $\epsilon_{eff}(f)$ for 16-14-8 domain region permittivities as shown from Figure 3.13 with different domain sizes and comparison with baseline. Note the large change in shift of the curve due from the 'old' to the 'new' domain construction.

The dispersion curves for $\epsilon_{eff}(f)$ show that the new curve has a quasi-static limit much higher than the old curve for the 16-14-8 domain dielectric construction. Moreover, the dispersion curve has been shifted back towards the left which increases the onset of dispersion. Thus, we have gained an additional insight into the effects of dispersion which will help us in the discussion for the next section.

## 3.3 Optimization Considerations

We may now explore the possibility of optimizing the *dispersive shift* behavior by adjusting the domain parameters for the given structure. It is clear that this is a complex procedure due to the number of different variables that are involved. However, if we assume that we start with a fixed number of domains and that these only vary in size in one dimension then a reasonable algorithm may be developed. Figure 3.15 shows a simplified flow-chart of the process.

At the beginning of the process we wish to input three main parameters into the algorithm. First, we want to input the characteristics of the transmission line behavior which will also be the baseline structure from which we start. This will give us our quasi-static or *QS* goal for the model. Second, we want to input our boundary conditions *BC's* for the domains in the dielectric region. There are typically practical limits to the permittivity boundaries as well as the $x$ dimensions for the domains. Thus, these adjustments will need to have boundary conditions to them which will limit the dispersive shift attainable. Third, there needs to be a dispersive shift *DS* goal in mind similar to what may be calculated using equation 3.2. This will allow the algorithm to end once the appropriate *DS* value

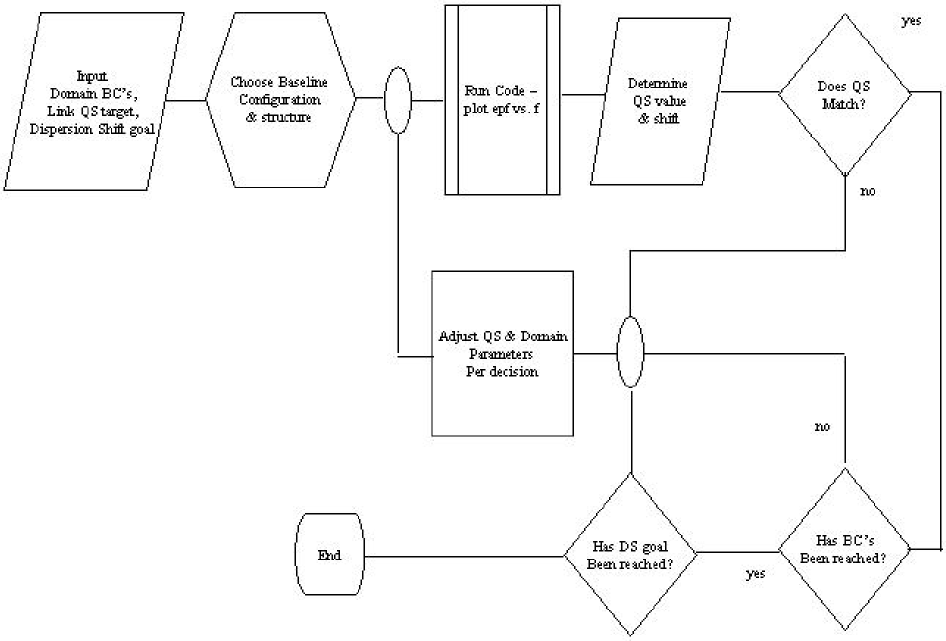


Figure 3.15: Simple optimization flow-chart for creating dispersive shift construction using domain physical and domain permittivity changes.

has been achieved.

The algorithm will need to check at each point whether or not the objectives are being met. After computing and plotting $\epsilon_{eff}(f)$ from the first given inputs, the algorithm will check whether or not the $QS$ limit has been achieved. If not, the domain parameters will be adjusted to fix this. This will be true for the $DS$ parameter where the measurement from the inflection regions of both curves is checked to determine the size and direction of the dispersive shift. An important consideration is that both permittivity and domain size play a significant role in the $DS$ factor. Thus, both will likely need to be adjusted for every iteration until either the BC's are reached or the dispersive shift goal has been reached. An algorithm which may accomplish the above is a *genetic algorithm*. Koledintseva [24] discusses the use of a genetic algorithm for modeling dielectric mixture changes using FDTD for a particular electromagnetic problem. The genetic algorithm runs its course until either self-imposed limits are achieved or it reaches its pre-intended outcome. A similar genetic algorithm may be developed to model the previously described problem.

# Chapter 4

# Future Topics for Research

## 4.1 Preliminaries

This chapter discusses future topics for research into step-graded or other gradient structures and speculates on these constructions. The first part discusses the construction of a demonstration vehicle and how this would be accomplished and the test method that might be used to experimentally validate some of the results in Chapter 3. The next part of the chapter discusses different types of constructions that might be analyzed for future research - particularly $x$ and $y$ graded structures and continuously graded structures. The last part of this chapter summarizes these methods and speculates on their value and future research.

## 4.2 Test Vehicle Considerations

To validate the results discussed in chapter 3 will require a test vehicle. The question is, can such a vehicle be fabricated? One method to construct such a vehicle is to abut dielectric sections of different permittivities together and then laminate both sides with a copper cladding. One side could then be etched to create the actual microstrip trace. The material of choice would likely be FR-4 of some variant of the *fiberglass-re-enforced* standard. There are many varieties of FR based dielectric materials [19] that could give a reasonable range to the construction of the test vehicle. However, most of these materials have a lot smaller permittivity than that which was analyzed. Thus, some additional runs with the code would be warranted to validate the new construction. The plot of $\epsilon_{eff}(f)$ would obviously be shifted much higher in frequency relative to the data in Chapters 2 and 3 however the form of the curves should be consistent.

Another more interesting method towards constructing a test vehicle which is shown in Figure 4.1. This has the advantage of using one single type of dielectric material and then creating air-pockets in the lamination. The construction of a typical printed circuit board or *PCB* starts with a *core* dielectric which is laminated on 0, 1, or 2 sides with copper foil. These cores may be etched first and then placed together to create a *stackup* construction of a multi-layered PCB. To build the construction in Figure 4.1 one would take a non-copper laminated core and then sandwich it between two single copper laminated cores - one with the etched trace and the other with the ground plane side as shown. The three structures are epoxied together and then placed under high pressures and temperatures to cure the laminates and the epoxy resins. The key would be to prevent the regions where the air pockets were to not collapse. One method is to actually embed or *impact* small features into the regions prior to lamination to 1) create the air-pocket shape and 2) create a *bridged* type structure where along the length of the microstrip some support actually existed such that not the entire region was a complete air-void. Then, when the structure was put under pressure, this region would not collapse. The result would be a dielectric region where the *average* permittivity value in the region was made to the *domain* value which was desired.

## 4.3 Alternative Graded Structures

There were a few different graded structures which were considered during this research which appeared to have merit in controlling or changing dispersion. One was obviously the $x$ step-graded structure which was chosen for analysis. Another, was an $x$ and $y$ graded structure. This was chosen mainly as an alternative to the *continuously* graded structure which will be discussed in a moment. The $x$ and $y$ graded structure was a construction where domains existed in more then one $y$ dimension as in Figure 4.2.

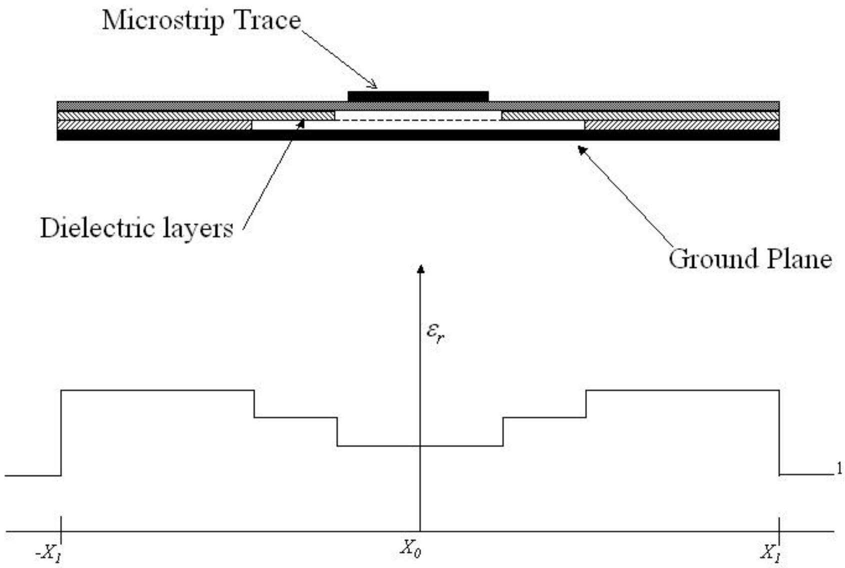


Figure 4.1: Example construction of manufacturable step-graded printed circuit board.

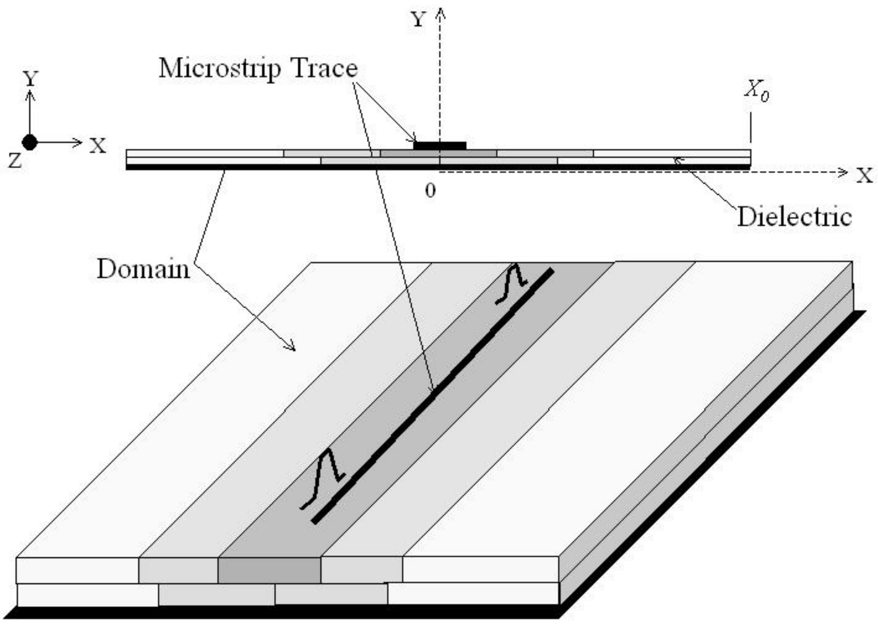


Figure 4.2: Alternative step-graded structure in $x$ and $y$ dimensions. Note the domains are still constant throughout the $z$ dimension.

The potential advantage of this structure is finer *potential* control over the changes in dispersive *shifting* due to the larger number of dielectric domains and the ability to change the field distribution in the $y$ dimension. However, it is unclear that the changes in the $y$ dimension will have a significant impact due to the smaller dimensional changes relative to the wavelengths of the signals. It is speculated that the main effect will be to again *average* the permittivity in the vertical region of the dielectric as was seen in the analysis in chapter 3.

The continuously graded structure is shown in Figure 4.3. The curved colored bands represent continuously changing dielectric permittivity in the shape shown which is somewhat elliptical. The intended affect on the fields or *eigen-vectors* would be that as shown in Figure 4.3. The continuously graded structure would force the fields to *steer* towards a given direction dependent upon the gradient value or change to the dielectric permittivity in that region. Thus, as the frequencies increased, the fields would attempt to coalesce underneath the strip and in the dielectric region for a constant permittivity. The gradient would attempt to move the fields away from the strip and thus shift the phase velocity of the given frequency component of the propagated wave of interest. Because the analysis has shown that this indeed does happen in the step-graded structures, it is likely to have a similar effect for a continuously graded structure as well.

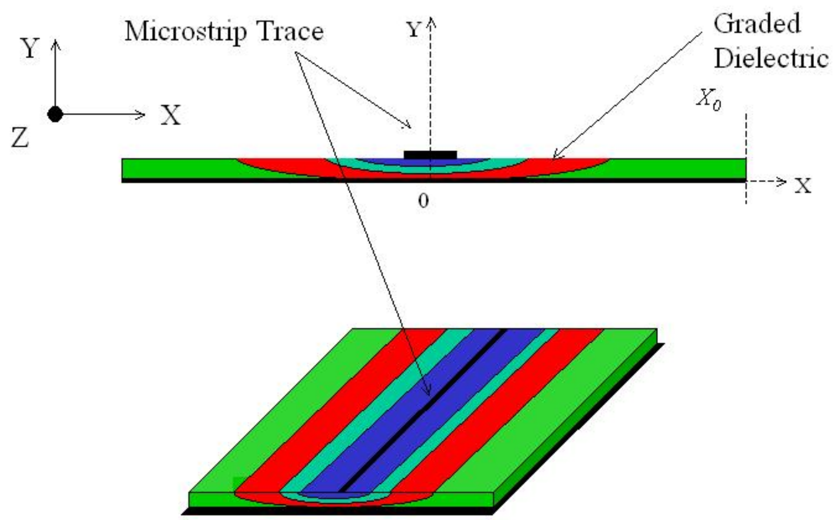


Figure 4.3: Alternative *continuously* graded dielectric structure in $x$ and $y$ dimensions. Note again the domains are still constant throughout the $z$ dimension.

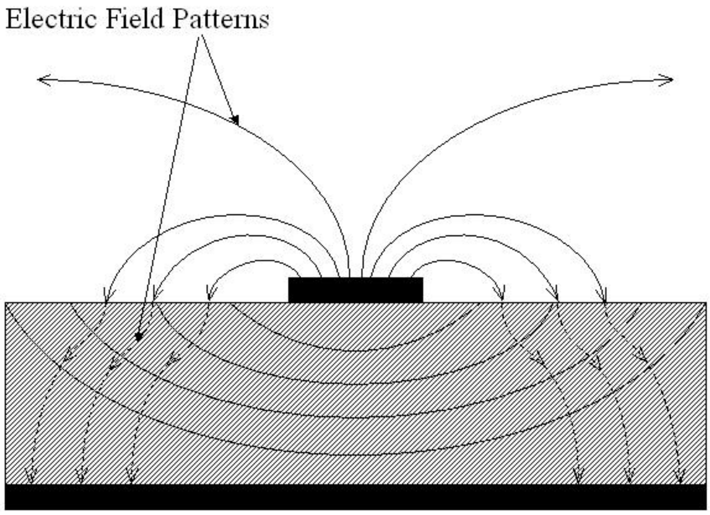


Figure 4.4: Speculated electric field patterns for *continuously* graded dielectric structure in $x$ and $y$ dimensions as shown in Figure 4.3.

### 4.3.1 Alternative Graded Structure Modeling

A number of the aforementioned alternative graded structures may be modeled with the current code. For example, any of the structures where the dielectric grading is not *continuous* may be modeled by the existing step-graded finite element code used herein. This is because the code was written to handle large number of domains and to solve the wave equation within these domains under the constraints of the boundary conditions. Both Figure 4.1 and Figure 4.2 are examples of step-graded structures that may be solved using the existing code. Other possible structures where the domains have a *constant* permittivity value across the entire domain may also be solved for. However, the more complex the structure (e.g. number of domains and finite elements), the longer the solution time will take. As an example, it took approximately 14 days to accumulate 16 data points for a dispersion curve for a 10,000 mesh structure on 8 dual-processor 2.5 GHz Intel Pentium Xeon servers. Typically, to generate one curve takes about twice the amount of data points. Because of very long time it takes to generate the data, choosing a structure to analyze must be judicious. The *continuously* graded structures, such as in Figure 4.4 would require a fairly substantial change to the code since the gradient would be essentially element by element. Section 4.3.2.1 discusses the mathematics behind this problem in some detail. The methodology behind solving this problem is considered beyond the scope of the dissertation since the algorithm would require a more in-depth analysis than was presented in Chapter 2.

### 4.3.2 Considerations for the Graded Dielectric Domain

The *PDE Toolbox* in Matlab was not equipped to handle the boundary conditions which are internal to the waveguide structures. Moreover, the PDE Toolbox is only structured to handle certain types of standard PDE's, such as standard elliptic and hyperbolic equations. Thus, the numerical solution to the inhomogeneous waveguide problems had to be accomplished through a separate code which was developed for solving the step-graded problem. However, the Matlab based code that was constructed made use of the mesh generation tool and the *exporting* capabilities of the toolbox for assemblage of the coefficient matrices. This simplified the development of the code and the solution overall.

It has been the hypothesis of this research to ask the key question of how *grading* the dielectric region effects the wave vector in the $z$-direction. To expedite the solution and determine if the approach of grading the dielectric was viable, a code was developed which *step-graded* the dielectric rather than continuously graded it.[1] This had the advantage of using a known method for solving the microstrip problem which made use of solving a simpler problem; namely, the homogeneous Helmholtz

[1] The initial speculation was that a *continuously* graded structure would be required to achieve the desired result in changing the dispersive properties. The step-graded approach was arrived at some time into the research.

equation. Because each region in the structure is homogeneous, the solution to the Helmholtz equation may be found in each region while simultaneously applying the boundary conditions between them. Additionally, the elegance of the method described in Chapter 2 showed that the internal boundaries between dielectric regions are handled through the boundary integral formulation which was easily programmed.

The basis though for the research into this method was as follows. The function $\epsilon(x, y)$ is unknown. Thus, our goal is to find the optimal grading function $\epsilon(x, y)$ for the microstrip structure chosen, *should it become necessary.* If we assume for the moment that there is only a variation in the gradient of the function $\epsilon(x, y)$ in the $x$ dimension (e.g. $\epsilon_x$), and if we *guess* this function to be some simple form (e.g. exponential, linear, etc.), a good approximation of the function may be to create homogeneous segments that piece-wise approximate the shape of the functional grading in $x$. That is, we may segment the dielectric region into rectangular regions which are homogeneous in $\epsilon_r$ but change from region to region as one moves in the x-dimension. Figure 4.5 illustrates the concept assuming the gradient function is a natural log function.

We begin by assuming that the *average* value of $\epsilon_r$ is 4.2 (as an example). Then, we generate an approximation to this average value over the dielectric region in $x$ with a natural log function as shown in Figure 4.5. If we wish to change

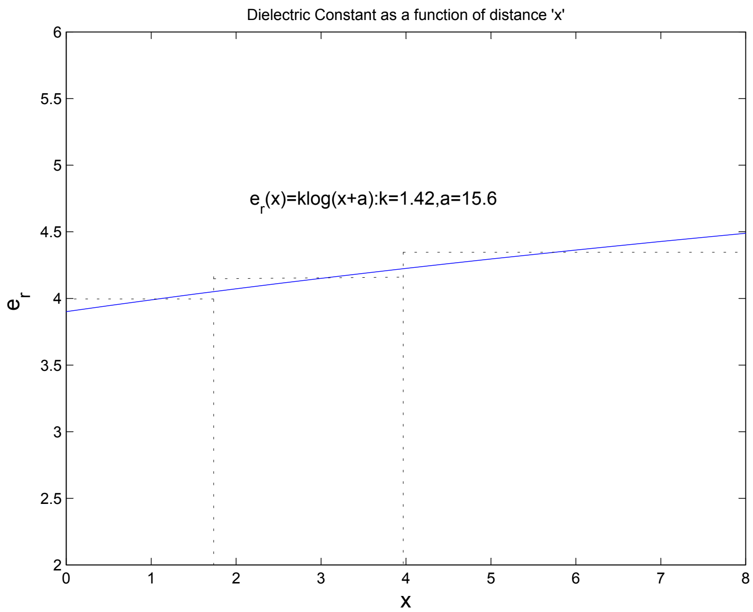


Figure 4.5: Piece-wise Approximation to Grading Function using natural log function.

the dispersive characteristics of a standard microstrip we need to increase the phase velocity of the waves nearest the microstrip and then decrease them further away from the strip. The hypothesis being that fields tend to concentrate near the microstrip trace itself as the frequencies increase and thus the phase velocity is lower with increasing frequency. Thus, it is speculated that by lowering the dielectric constant in the region closest to the strip, the phase velocity of the wave should increase generating a less dispersive electromagnetic wave in the microstrip waveguide and thus reducing the amount of phase distortion to the signal which propagates down the microstrip waveguide.

By approximating the function with a piece-wise step function of a natural log function (as an example) the FEM code was easily generated to solve the standard microstrip problem was then easily adapted to solve for the eigenvalues in a *step-graded* microstrip structure. The *average* of the steps will be made to equal the dielectric constant of a homogeneous dielectric region ($\epsilon_r = 4.2$ in this example) which we saw in the previous chapter to *average* out the *quasi-static* limit in $\epsilon_{\mathit{eff}}(f)$.

Some of the mathematics behind the *continuously* graded structure is given in the next section.

#### 4.3.2.1 Generalized PDE for Continuously Graded Structures

The functional of the PDE for the homogeneous case, where the permitivity of the dielectric is constant throughout the region, is well known and is easily derived

[47, Chapter 4, Section 4.4]. The functional for the inhomogeneous case where there are two separate regions, but where each region (i.e. air and dielectric under the microstrip trace) is itself homogeneous, is a bit more complex and a derivation may be found in [9] and provided in chapter 2. If further complexity is necessary to solve the *inhomogeneous* Helmholtz equation numerically it is first necessary to derive the PDE where one of the regions of the structure has a domain which is inhomogeneous or *continuous*. The PDE for this case (e.g. the microstrip dielectric region) is a function of $x$ and/or $y$ and results in a coupled set of inhomogeneous Helmholtz equations. To see this, we start from Maxwell's equations and assume sinusoidal variation in the positive $z$ direction and in time as was done previously for the *homogeneous* Helmholtz equation.

$$\nabla \times \vec{\mathbf{E}} = j\omega\mu\vec{\mathbf{H}} \tag{4.1}$$

$$\nabla \times \vec{\mathbf{H}} = -j\omega\epsilon\vec{\mathbf{H}} \tag{4.2}$$

Taking the curl of both sides of equation 4.1 and using a vector identity yields

$$\nabla^2\vec{\mathbf{E}} - \nabla(\nabla \cdot \vec{\mathbf{E}}) - k_d^2\vec{\mathbf{E}} = 0 \tag{4.3}$$

Where $k_d$ is the wavevector in the domain $d$. Using the divergence relation for the electric flux density we can simplify the middle term in equation 4.3

$$\nabla \cdot \vec{\mathbf{D}} = \nabla \cdot (\epsilon\vec{\mathbf{E}}) = \epsilon\nabla \cdot \vec{\mathbf{E}} + \vec{\mathbf{E}} \cdot \nabla\epsilon = 0 \Rightarrow \nabla \cdot \vec{\mathbf{E}} = -\vec{\mathbf{E}} \cdot \frac{\nabla\epsilon}{\epsilon} \tag{4.4}$$

which yields the generalized inhomogeneous Helmholtz wave equation for the electric field

$$\nabla^2\vec{\mathbf{E}} - \nabla(\vec{\mathbf{E}} \cdot \frac{\nabla\epsilon}{\epsilon}) - {k_d}^2\vec{\mathbf{E}} = 0 \tag{4.5}$$

A similar derivation can be made for the magnetic field which results in equation 4.6

$$\nabla^2\vec{\mathbf{H}} - j\omega(\nabla\epsilon \times \vec{\mathbf{E}}) - {k_d}^2\vec{\mathbf{H}} = 0 \tag{4.6}$$

We can expand equations 4.5 and 4.6 to get six scalar wave equations in terms of the electric and magnetic fields $(E_x, E_y, E_z)$ and $(H_x, H_y, H_z)$. The electric field scalar equations in terms of the previous field quantities are

$$\begin{gathered}\nabla_{\perp}^2 E_x + \left\{\frac{1}{\epsilon}\frac{\partial E_x}{\partial x}\frac{\partial \epsilon}{\partial x} + \frac{E_x}{\epsilon}\left(\frac{\partial^2 \epsilon}{\partial x^2} - \frac{1}{\epsilon}\left(\frac{\partial \epsilon}{\partial x}\right)^2\right)\right\} + \\ \left\{\frac{1}{\epsilon}\frac{\partial E_x}{\partial y}\frac{\partial \epsilon}{\partial x} + \frac{E_x}{\epsilon}\left(\frac{\partial^2 \epsilon}{\partial x \partial y} - \frac{1}{\epsilon}\frac{\partial \epsilon}{\partial y}\frac{\partial \epsilon}{\partial x}\right)\right\} - jk_z E_x \frac{\partial \epsilon}{\partial x}\frac{1}{\epsilon} - \left({k_d}^2 + k_z^2\right) E_x = 0\end{gathered} \tag{4.7}$$

$$\begin{gathered}\nabla_{\perp}^2 E_y + \left\{\frac{1}{\epsilon}\frac{\partial E_y}{\partial x}\frac{\partial \epsilon}{\partial y} + \frac{E_y}{\epsilon}\left(\frac{\partial^2 \epsilon}{\partial x \partial y} - \frac{1}{\epsilon}\frac{\partial \epsilon}{\partial y}\frac{\partial \epsilon}{\partial x}\right)\right\} + \\ \left\{\frac{1}{\epsilon}\frac{\partial E_y}{\partial y}\frac{\partial \epsilon}{\partial y} + \frac{E_x}{\epsilon}\left(\frac{\partial^2 \epsilon}{\partial y^2} - \frac{1}{\epsilon}\frac{\partial \epsilon}{\partial y}\left(\frac{\partial \epsilon}{\partial y}\right)^2\right)\right\} \\ -jk_z E_y \frac{\partial \epsilon}{\partial y}\frac{1}{\epsilon} - \left({k_d}^2 + k_z^2\right) E_y = 0\end{gathered} \tag{4.8}$$

$$\nabla_{\perp}^2 E_z - \left({k_d}^2 + k_z^2\right) E_z = 0 \tag{4.9}$$

And for the magnetic field quantities

$$\nabla_{\perp}^2 H_x + j\omega\frac{\partial \epsilon}{\partial y} E_z - \left({k_d}^2 + k_z^2\right) H_x = 0 \tag{4.10}$$

$$\nabla_{\perp}^{2} H_y + j\omega \frac{\partial \epsilon}{\partial x} E_z - \left( {k_d}^2 + k_z^2 \right) H_y = 0 \tag{4.11}$$

$$\nabla_{\perp}^{2} H_z + j\omega \left( \frac{\partial \epsilon}{\partial x} E_y - \frac{\partial \epsilon}{\partial y} E_x \right) - \left( {k_d}^2 + k_z^2 \right) H_z = 0 \tag{4.12}$$

where

$$\nabla_{\perp}^{2} = \frac{\partial^2}{\partial x^2} + \frac{\partial^2}{\partial y^2} \tag{4.13}$$

Note there is no $\partial\epsilon/\partial z$ term because it is assumed that there will be no variation in $\epsilon$ in the $z$ direction of the dielectric. Again, if we assume that $\epsilon$ is constant in the dielectric region, then the previous scalar equations become homogeneous Helmholz equations. The next step would be to generate the functional for these *inhomogeneous* Helmholtz equations. As previously stated, this is beyond the scope of this dissertation and will be left to other research.

# Chapter 5

# Summary

Microstrip transmission lines are used extensively in many applications ranging from microwave frequencies in the *X-Band* and higher to simple interconnect structures for low frequency DC level signals. In today's engineering world where higher bandwidth and lower cost are essential there has been and still remains a very strong need to push the limits of technology in order to satisfy these requirements. However, the physics of the problem still remain.

In Chapter 1 it was shown that for digital communications across printed circuit boards the characteristics of the line could be bounded such that transmission across the link at 40 Gigabits per second on a single microstrip over a 12 inch length would be achievable. The main limitation in this case would be dispersion of the microstrip dielectric-air interface. The attenuation due to surface roughness and skin-effect resulted in an attenuation of approximately 16 dB at 23 GHz. Not including the parasitics of the package from the silicon this provided a reasonable bound for the interconnect losses. Transmitter and receiver technologies today can switch at these high frequencies but in the presence of noise and with low gain only. Dispersion still remains a problem and it was shown that the onset of dispersion for this line occurred at around 7.65 GHz. Additionally, it was found that a 60 degree phase shift occurred at 10 GHz for this microstrip structure alone thus indicating a strong need for dispersion compensation.

The next step was to determine the method for analyzing the microstrip structure. The Finite Difference Time Domain method was first examined in some detail. This was found to work very well for most electromagnetic problems except that near the edges of the strip convergence problems existed and thus the FDTD method was abandoned. Conformal mapping techniques were also examined and found to be lacking in the mesh density area and also had issues with convergence. Finally, though more complex to code and understand, the Finite Element Method (FEM) was chosen due to availability of tools, accuracy, convergence, and synergy with the research.

Csendes [9] and Ahmed [2] proposed a very interesting approach to solving waveguide problems with the FEM method whereby two matrix equations were combined to essentially one coupled scalar equation which solved for $E_z$ and $H_z$

simultaneously. The method was outlined in detail in Chapter 2. Nonetheless, the authors likely did not anticipate the usage for their approach and a number of modifications were necessary in order to solve the *step-graded* microstrip problem. Some of these changes included expansion of the boundary surface integral and adaptation of code to the Matlab PDE Toolbox for the Rayleigh-Ritz method. Once these modifications were made a modular code was written to solve very generic electromagnetic waveguide and microstrip problems allowing for checks on the efficacy of the code at every step of the development. Both accuracy and convergence were analyzed for the approach and a method for determining the proper eigenvalues for the lowest order $EH_0$ microstrip mode was determined. This allowed for taking the next step which was an analysis of step-graded microstrip structures.

In Chapter 3, various step-graded structures were analyzed. It was found thru parametric analysis of various step-graded configurations that the structure that forced the largest *shift* in the dispersion curve was the one where the permittivity underneath the strip was the lowest. Though in one case this was consistent with the original supposition that the fields would *coalesce* underneath the strip as the frequency increased it was found that the fields tended to coalese into the regions of highest permittivity and thus the phase velocity of the wave would be dominated by the dielectric in this region. It was also seen that an *averaging* effect took place at the lower frequencies of interest or *quasi-static* regime where the values in the *domains* of the dielectric region averaged out the quasi-static effective permittivity $\epsilon_{ef0}$ allowing one to design for certain transmission line parameters in this region. The other important observation was that the slope of the dispersion curve appeared to not be affected by step-grading the microstrip structures however the frequency band of the dispersion curve was definitely affected by the grading. A figure of merit was observed for quantifying this *shift* with the equation 5.1 below.

$$Shift = (I)^{0.2\delta} \tag{5.1}$$

where $I$ is the frequency at which the inflection point on the baseline curve exists, $\delta$ is the maximum differential between domain static permittivity values and *shift* is the curve shift in MHz from its initial point. It was also shown that at very high frequencies other dielectric modes existed due to the reflection of the waves at the boundaries of the dielectric regions. It was observed that one such mode was the $TE^z_{31}$ mode was observed in the dielectric region for a rectangular waveguide. These resultant new modes or *waveguide* modes coming into play in the higher region of the dispersion curve indicated a fundamental limit to the approach, though this occurs beyond the *inflection region* of the curve beyond the quasi-static limits. Finally, an optimization algorithm was proposed for optimizing the dispersive *shift* for the step-graded microstrip problem where the onset of dispersion could be somewhat controlled thru grading the dielectric structures.

Other possible gradient methods and structures were proposed in Chapter 4 along with a method for fabricating the step-graded structure but were not simulated in this thesis. Using the current code however, some of these structures could be analyzed as well. An $x$ and $y$ domain gradient structure was proposed where more than one dielectric layer existed in the dielectric domain. A continuously graded structure was also proposed though this would require a new FEM code to analyze. A fabrication method whereby laminates were adjoined to each other on a printed circuit board was proposed which would allow a test vehicle to be developed to verify experimentally the results in this dissertation. Such a structure could be tested with a Vector Network Analyzer (VNA) up to a reasonably high frequency to determine the efficacy of the approach.

This thesis has discussed the facets of using step-graded dielectric structures for affecting dispersion in a microstrip in some fashion for propagation of the $EH_0$ mode. It has been shown that grading the dielectric in this way does indeed change the dispersive characteristics of the waveguide microstrip. Other methods of grading this structure have been discussed which may also be able to make similar changes to the dispersive properties in microstrips. Further research is likely warranted given the results herein on these and possibly other structures which may enable a method to passively affect dispersion for applied applications such as high speed communications in the future.

# Appendix A

# Static Numerical Analyses

## A.1 Quasi-Static Parameter Extraction

To solve the microstrip problem with the finite element method it helps that it be broken down into simpler sub-problems. To prove the efficacy of the approach in *grading* the dielectric structure it is simpler and more efficient to simplify the numerical and analytical method by making approximations which allow the use of a 2D code. To begin with, we will solve for the static parameters of the structure. These, in turn, may be used to compare with the *non-static* results when we solve for the wavevector $k_z$ and the frequency dependent permitivity $\epsilon_{\mathit{eff}}(f)$. The method, analysis, and results are outlined in the following sections of this appendix.

### A.1.1 Generation of Static Parameters

Using the finite element method in two-dimensional space we can extract the capacitance, impedance, and phase velocity for the input parameters to be used in our *pseudo* three-dimensional analysis. The mesh for the structure is generated using Matlab's *Partial Differential Equation Toolbox* [29] which is a two-dimensional PDE solver with a graphical user interface linked to numerous subroutines. The toolbox has a 2D finite element mesh generator which uses a *Delauny* triangulation method to generate the mesh. It also has an electrostatics solver which solves Laplace's equation for the potential in the structure. By solving for the electric field $\vec{E} = -\nabla V$ one can use the static field to launch the pulse into the waveguide. Figure A.1 shows the mesh generated for the computational space. Note that the microstrip was centered along the *y-axis* as shown in Figure 1.7, and in Figure A.1 only the right-half side of the waveguide region is gridded. This was done for computational efficiency.

As is evident in the lower corners of Figure A.1 the algorithm for the mesh generator generates a fine mesh in the regions where large variations in the solution occur and generates a more coarse mesh in the other regions. The mesh is generated with the '.m' file *initmesh.m* in the PDE Toolbox. The boundary on the vertical *y-axis* is set as a *Neumann* boundary since the structure is perfectly symmetrical and therefore the solution will not change across the *y-axis*. The other boundaries

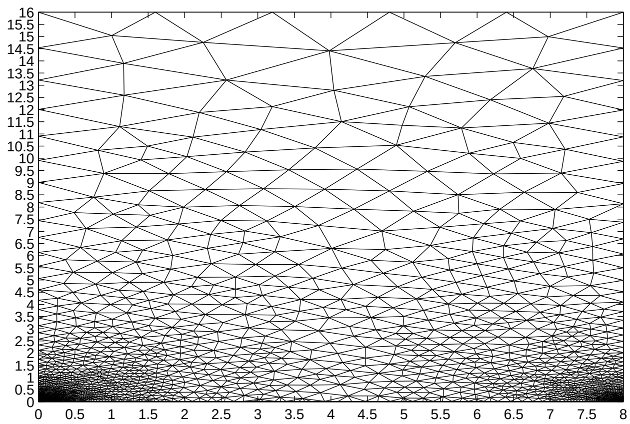


Figure A.1: Mesh generation of microstrip half-space.

are *Dirichlet* and have zero potential except the microstrip itself which is set to 1V for simplicity in computation [1]. Using the PDE Toolbox, the potential in the region can be computed. This is shown in Figure A.2 where the solution was computed and plotted over a finite region using Matlab's PDE Toolbox graphing functions.

Using the *export* facility in the PDE Toolbox allows one to export the FEM mesh matrices and the solution vector $V$ to the Matlab workspace. Then, using the computed results from the PDE Toolbox we may determine the static elements, $C_d, C_0, Z$, and $v_p$. This is illustrated in the next two sections through two different

[1]In the future, other boundary conditions will likely be used to limit the size of the solution space and improve the accuracy of the solution. As as example, an absorbing boundary on the top and right sides may be used to better model the actual microstrip in an 'open' space rather than in boxed or closed space as done here. The reason for not defining such boundaries now was mostly due to expediency. Also, *Neumann* boundaries, by definition, do not decay and previous attempts to model the other two boundaries as *Neumann* boundaries gave erroneous results.

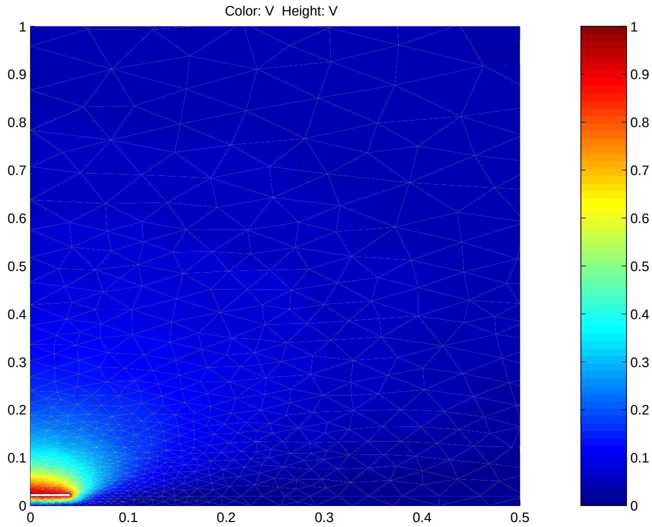


Figure A.2: Potential Distribution of Enlarged lower left section of Mesh in Figure A.1

methods.

#### A.1.1.1 Computation of Static Parameters - Method I

Extraction of the capacitance from an FEM generated solution is more difficult than from a finite difference solution. However, the fundamental equations are the same. Using the approach outlined in [47, chapter 3.7] we can compute the capacitance of the structure. The capacitance may be found from Gauss' law,

$$Q_{enclosed} = VC_d = \oint D \cdot dl = \oint \varepsilon E_n \cdot dl \tag{A.1}$$

where $Q_{enclosed}$ is the total charge enclosed on the microstrip trace, $V$ is the potential on the conductor, $C_d$ is the capacitance per-unit-length with the dielectric in place, and $E_n$ is the electric field normal to the line of integration. The objective is compute the capacitance with and without the dielectric in place. This may accomplished by solving the dual problem for $C_0$ with the dielectric constant $\epsilon_r$ in the region set to 1. To accomplish this we integrate around the loop region shown in Figure A.3 over each of the line segments *C1-C3* shown. The actual path of integration was done along the border of the microstrip for ease in determining each triangle location and node. Note that since we are only computing in half the waveguide region the resulting capacitance will be half of the actual capacitance. Therefore, the result will need to be doubled to compute the actual capacitance of the microstrip circuit.

Numerically, we determine the *node* locations on the microstrip trace and compute the electric field from $\vec{E} = -\nabla V$. Since we are using linear interpolation functions inside each element, the electric field is constant within a particular triangular element. This allows us to compute the electric field directly from the coefficients of the voltage equations for each finite element. A finite element program computes the capacitance and the static parameters of the microstrip structure. The results of the computations are also shown in Table A.1.

The method and coding was difficult since it was required to find each triangle,

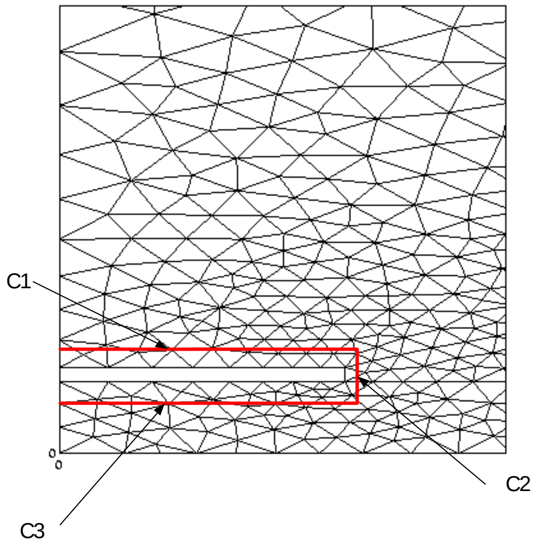


Figure A.3: Enlarged lower left section of mesh in Figure A.1 denoting integration path.

node, and potential at each node in the loop on the microstrip border and then integrate around that loop. This process was performed manually and was a bit cumbersome. The proper way to find each node would be to automate this process. This was not done for expediency sake but may be done at a later date. An alternative method, illustrated in the next section, computes the static parameters using a more efficient process.

#### A.1.1.2 Computation of Static Parameters - Method II

Another, and more elegant, way to compute the static parameters is by computing the energy from the functional directly. We start by solving Laplace's equation, which is in a particular form of an elliptic equation

$$-\nabla \cdot (c\nabla V) = 0 \tag{A.2}$$

subject to the boundary conditions

$$\vec{n} \cdot (c\nabla V) + qV = g \tag{A.3}$$

where $\vec{n}$ is the vector normal to the boundary surface and $c, q$ and $g$ are coefficients for the PDE and boundary conditions. The boundary conditions in equation A.3 are *Generalized Neumann* [29, section 4]. The elements of the coefficient matrix or scalar $c$ is determined from the dielectric constant $\epsilon_r$ in a particular region of the waveguide structure. Using a similar method to that in [29] we now multiply equation A.2 by a test function $v$ and then integrate over the domain $S$ of the waveguide region which was previously defined in Table 1.5 and Figure 1.7.

$$-\int_S \nabla \cdot (c\nabla V) v dS = 0 \tag{A.4}$$

We now integrate by parts in equation A.4 and use *Green's Theorem* to simplify [13, Chapter 2, Vol.1].

$$-\int_S \nabla \cdot (c\nabla V) v dS = \int_S (c\nabla V) \cdot \nabla v dS - \int_C (c\nabla V) v dl = 0 \tag{A.5}$$

$$\implies \quad \int_S (c\nabla V) \cdot \nabla v dS - \int_C (g - qV) v dl = 0 \qquad \forall \mathbf{V} \tag{A.6}$$

where $C$ is the boundary for the two dimensional space, and $v, V \in \mathbf{V}$ which is defined as some function space. Equation A.6 is the variational or *weak* form of the solution. Note also that we substituted for $c\nabla V$ from equation A.3 into equation A.6. We now replace the solution $V$ and the test function $v$ with a set of basis functions $(\phi_i, \phi_j)$ and substitute into equation A.6 where the basis functions $\phi \in \mathbf{V}_{N_\mathrm{p}}$ in an $N_\mathrm{p}$ dimensional space.[2]

$$\sum_{j=1}^{N_p} \left( \int_S (c\nabla\phi_j) \cdot \nabla\phi_i - \int_C q\phi_j\phi_i \right) V_j = \int_C g\phi_i dl, \qquad i = 1 \ldots, N_p \tag{A.7}$$

Using the definitions from [29] we get the following matrices

$$K_{i,j} = \int_S (c\nabla\phi_j) \cdot \nabla\phi_i dS \tag{A.8}$$

$$Q_{i,j} = \int_C q\phi_j\phi_i dS \tag{A.9}$$

[2] $\mathbf{V}_{N_\mathrm{p}} \subset \mathbf{V}$ where $\lim\limits_{N_\mathrm{p}\to\infty} \mathbf{V}_{N_\mathrm{p}} = \mathbf{V}$.

$$G_i = \int_C g\phi_i dl \tag{A.10}$$

where the matrix equation now becomes $(K+Q)V = G$. The m-file *assempde* assembles the matrices and also solves for the solution $V$ if desired. Because the boundary elements may be included in the solution the voltage in the *total* region is now available. The solution vector $V$ may be solved for by exporting the matrices $K, Q$ and $G$ to the *Matlab* workspace.[3]

We may now determine the capacitance using the method outlined in [47, chapter 6.2.2]. The energy of the structure is found from

$$W = \frac{1}{2}\int \epsilon \left|\mathbf{E}\right|^2 dS = \frac{1}{2}\int \epsilon \left|\nabla V\right|^2 dS \tag{A.11}$$

where $W$ is the total energy *per-unit-length* in the waveguide and $V$ is the voltage throughout the region which has been previously solved for. If we replace the integral in A.11 with a summation and use the results from equation A.7 we get the following simplified matrix equation

$$W = \frac{1}{2}\epsilon V^t K^p V \tag{A.12}$$

Where $K^p$ is the matrix of the functional defined in [47][4] and is the assemblage of $K+Q$. Equation A.12 is computed directly through exporting the parameters

[3]Because of the two regions in the microstrip structure (with and without the dielectric) often the solution must be broken up into at least two solution spaces with a boundary between them. However, the m-file *assempde* can assemble the elements of all of the defined regions of the solution space and boundaries and can simplify the matrix equations so that the total solution may be easily solved for. Alternatively, one may separate out the boundary conditions and the separate regions if needed through various function calls to *assempde*.

[4]the equation defined in [47] assumed homogeneous boundary conditions which is different from the actual boundary conditions which is where the $G$ and $Q$ matrices comes from.

of the mesh and PDE coefficients to the Matlab workspace. By using another program we then compute the energy in the microstrip structure and extract the static parameters. The capacitance may be computed from the energy relation in the system using equation A.13

$$W = \frac{1}{2}CV^2 \tag{A.13}$$

or equivalently,

$$C = \frac{2W}{V^2} \tag{A.14}$$

where $C$ is capacitance in the system (either with or without the dielectric in place), $V$ is voltage potential on the microstrip conductor, and $W$ is energy computed previously using equation A.12. Because only half of the waveguide is used for the computational domain, the actual energy will be twice that given in equation A.13. To determine the static effective dielectric constant $\epsilon_{reff}$ we need to compute the dual problem where no dielectric is present in the structure. Thus, once the capacitance is determined the effective dielectric constant may be computed from the phase velocity in the structure,

$$v_p = \frac{1}{\sqrt{\epsilon_0 \epsilon_r eff \mu_0}} = \frac{v_0}{\sqrt{\epsilon_r eff}} = \frac{1}{\sqrt{LC_d}} \tag{A.15}$$

which results in,

$$\epsilon_{reff} = \frac{LC_d}{\mu\epsilon_0} = \frac{C_d}{C_0} \tag{A.16}$$

Using the same program we compute the static parameters of the structure. Table A.1 summarizes the static parameters computed using data from closed-form Mathcad equations and the Matlab programs created herein.

Table A.1: Computation of the static parameters using Mathcad and Matlab programs.

| Static Parameter | Mstrip.mcd | Capinite.m | Capinitg.m |
|---|---|---|---|
| $C_0 \quad (pF)$ | 60 | 61 | 37 |
| $C_d \quad (pF)$ | 200 | 205 | 230 |
| $Z \quad (\Omega)$ | 30.4 | 29.8 | 36 |
| $v_p \quad (10^8 m/s)$ | 1.64 | 1.64 | 1.21 |
| $\epsilon_{reff}$ | 3.33 | 3.36 | 6.22 |

The results in Table A.1 show that the computation of the static parameters using the energy of the system and the finite element method is very close to a known closed-form equation. Thus, we may assume that this check verifies that the results are very likely to be correct. The results using the method outlined in section A.1.1.1 is less accurate which may be due to the lack of data points used to compute the capacitances. Note also in the appendices the size differences in the codes to compute the same capacitances. The energy functional method in section A.1.1.2 is obviously superior in this case.

# Appendix B

# Waveguide Analysis

## B.1 Eigenvalue Computations for Waveguide

The eigenvalues for a homogeneous waveguide and an inhomogeneous (half-dielectric filled) waveguide are computed in this section with the data compared with results obtained from other literature (for the cases where it was available). The computations of the eigenvalues and eigenvectors for each structure use, essentially, the same Matlab routines for both structures with only variations in usage of the routines by the main code created for each. Unlike the computations for the static parameters in the previous section, a separate set of Matlab code was developed to solve the waveguide problems. This was due to inability of the PDE Toolbox to solve inhomogeneous problems such as a partially-filled dielectric waveguide or microstrip. The following sections discuss, in brief, the problems and methodologies followed to solve the aforementioned waveguide structures.

### B.1.1 Homogeneous Square Waveguide: $\mathrm{TM}_{11}$ Mode

A cross-sectional view of a square waveguide from the PDE Toolbox GUI is shown with the nodes and triangle element numbers labeled as shown in Figure B.1. The mesh was initially made coarse to ease in debugging the matrix assembly subroutines. The Matlab PDE Toolbox has an *export* function which ports the mesh data to the Matlab workspace for processing. The program *wghomodh.m* computes the cutoff wave numbers of a homogeneous waveguide and compares the results with those found in Sadiku [47, Table 6.5a]. The purpose of modeling a known problem such as a homogeneous waveguide was to insure the code was operating correctly.

The PDE for the solution to the cutoff wave numbers for a homogeneous square waveguide is found from the *Helmholtz* equation B.1.

$$\nabla^2\phi - k^2\phi = 0 \tag{B.1}$$

Where $\phi$ is either the electric or magnetic field. We assume that at cutoff $k_z = 0$; thus, solving for $k^2$ is the same as solving for the eigenvalues in equation B.1 with $k = k_c$, the cutoff wavenumber. The exact computation may be found from equation B.2.

$$k_c = \sqrt{(m\pi/a)^2 + n\pi/b)^2} \tag{B.2}$$

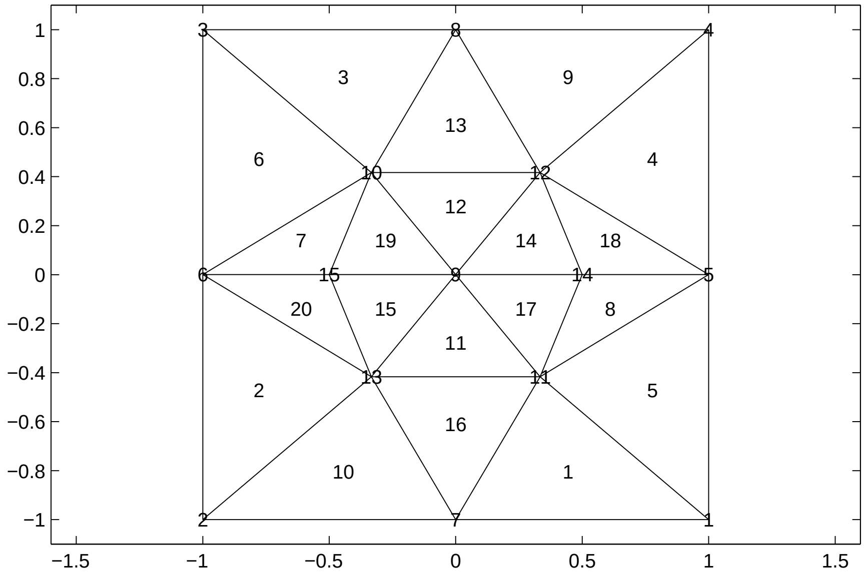


Figure B.1: Cross-section of Square Waveguide with Coarse Mesh.

Where $m$ and $n$ are the waveguide *cutoff* mode numbers. The results of the simulations for computing the waveguide cutoff wavenumber $k_c$ for the $TM_{11}$ mode are shown in Table B.1.

The results show that excellent accuracy is achieved with the Finite Element Method - even with a small number of mesh elements. The code runs fairly efficiently as well. The approximate CPU times are given in Table B.1 in the last column, where the code was run on an 800 MHz Pentium IV laptop computer. Since the PDE Toolbox can also solve this problem directly, comparisons were made with the program and the PDE Toolbox which resulted in the exact results obtained in Table B.1. A plot of the $TM_{11}$ mode using 1280 elements is shown in

Table B.1: Computation of cutoff wavenumber $k_c$ for $TM_{11}$ mode in homogeneous waveguide (exact value is 2.2214).

| No. Elements | $k_c^{11}$ | Percent Error | $\approx$ CPU time (sec) |
|---|---|---|---|
| 20 | 2.4117 | 7.89 | $< 1$ |
| 80 | 2.2747 | 2.34 | 2 |
| 320 | 2.234 | 0.61 | 33 |
| 1280 | 2.225 | 0.15 | 880 |

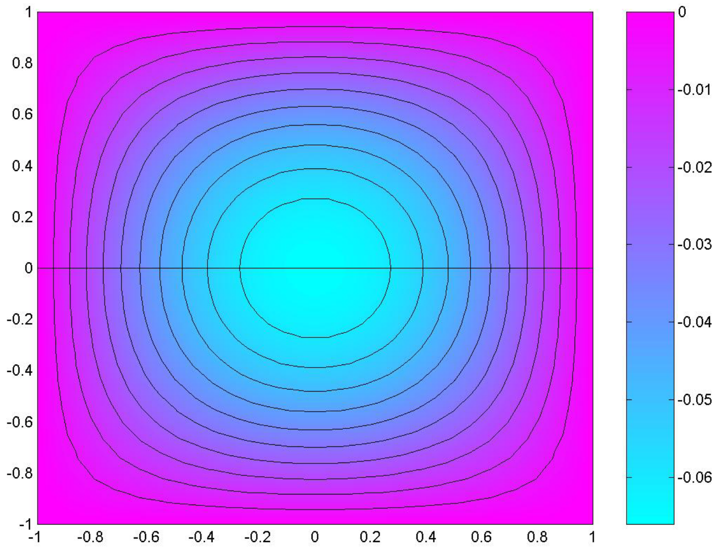


Figure B.2: Plot of $TM_{11}$ mode magnetic field contours for air-filled rectangular waveguide (1280 elements).

Figure B.2. As expected, the contours in the plot closely match the field contours for the $TM_{11}$ mode in Balanis [6, Figure 8-4].

### B.1.2 Partially-Filled Dielectric Waveguide

This section analyses a partially-filled dielectric waveguide. Specifically, the cutoff frequencies of a partially-filled dielectric waveguide are determined along with selected field plots. The waveguide in Figure B.3 shows a cross section of the waveguide with the mesh structure. The section below the red line in the Figure is the dielectric region. The dimensions and properties are the same as those described in [6, Chapter 8]. The objective is to solve numerically for the solutions of the fields and compare them with the analytical results in [6].

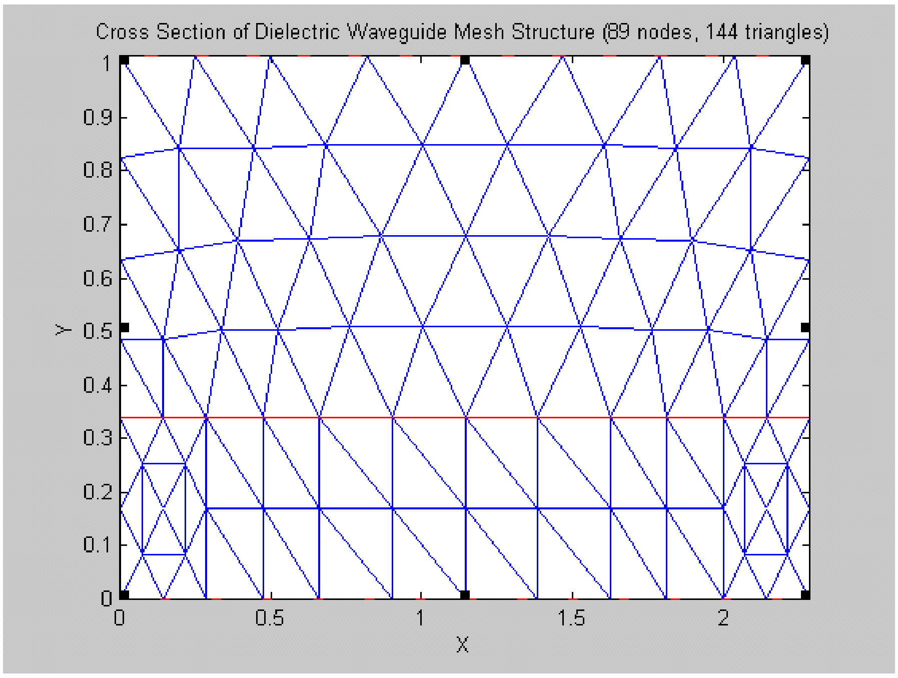


Figure B.3: Cross-section of partially-filled waveguide.

The first step is to examine the analytical results given in Balanis [6]. In order to analyze the field solutions the cutoff frequencies must be determined first. The cutoff frequencies may be found by solving the dispersion relation for the waveguide mode of interest. *Balanis* provides solutions for both the $TE^y_{0n}$ and $TM^y_{1n}$ modes for the first 3 cutoff frequencies for both of the $TE$ and $TM$ modes. Because the *z-directed* electric and magnetic fields are identically zero for all $TE^y_{0n}$ modes and the *z-directed* electric fields are zero for the $TM^y_{1n}$ modes at cutoff, we will examine only the magnetic fields for the $TM^y_{1n}$ modes at specific cutoff frequencies. This will allow us to visualize the field solutions as well as compare the results of the numerically derived cutoff frequencies with the analytical solution. The transcendental equation for the solution of the $TM^y_{1n}$ mode cutoff frequencies was given in [6, Chapter 8, equation 8-130] and is repeated here in equation B.3 for reference.

$$\begin{aligned}&\frac{\epsilon_d}{\epsilon_0}\sqrt{{\omega_c}^2\mu_0\epsilon_0 - \left(\frac{\pi}{a}\right)^2}\tan\left[(b-h)\sqrt{{\omega_c}^2\mu_0\epsilon_0 - \frac{\pi}{a}^2}\right]\\ &= -\sqrt{{\omega_c}^2\mu_d\epsilon_d - \frac{\pi}{a}^2}\tan\left[h\sqrt{{\omega_c}^2\mu_d\epsilon_d - \frac{\pi}{a}^2}\right]\end{aligned} \tag{B.3}$$

where $b$ is the width of the waveguide in the $y$ dimension and $h$ is the height of the dielectric region in the same direction. Equation B.3 was solved using a program written in Matlab and utilizing the *Symbolic Math Toolbox*. A plot of the first four cutoff frequencies are shown in Figure B.4. The zero-cross over points correspond to the cutoff frequencies of the waveguide. By estimating visually the value at cutoff and choosing this value for a starting point (for each zero crossover point), we can then use *Newton's Method* to solve for the exact solution iteratively. Because the solutions to the first three cutoff frequencies were previously found by *Balanis* we may check the results using [6]. The results for the first three frequencies show excellent correlation to the results in *Balanis* as shown in Table B.2. Thus, for the $TM^y_{1n}$ modes one may assume that the analytical solution to the cutoff frequencies using the Matlab code is quite accurate.

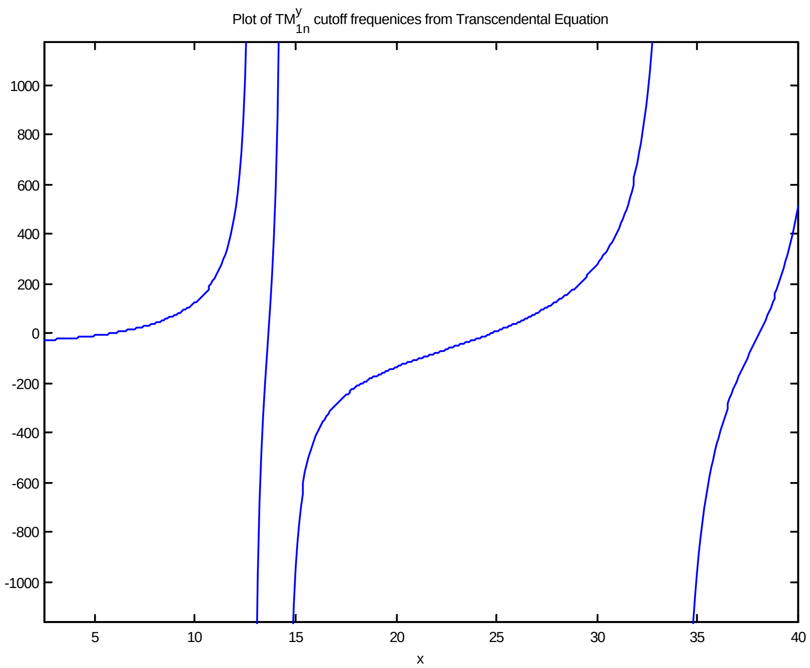


Figure B.4: Plot of transcendental equation for first 4 cutoff frequencies of the $TM_{1n}$ modes given in equation B.3. Frequencies are found when function crosses $y = 0$ axis.

The next step is to examine the magnetic field plots at the derived cutoff frequencies. The magnetic fields are computed from the *magnetic vector potentials* for each of the two regions of the waveguide. Using the method outlined in Balanis, we solve for the magnetic fields in both the dielectric and air regions.

$$H_z^0 = \frac{1}{\mu}\frac{\partial A_y^0}{\partial x} = \frac{B_{mn}^0 \pi}{\mu a}\cos\left(\beta_{x0} x\right)\cos\left[\beta_{y0}(b-y)\right] \tag{B.4}$$

$$H_z^d = \frac{1}{\mu}\frac{\partial A_y^d}{\partial x} = \frac{B_{mn}^d \pi}{\mu a}\cos\left(\beta_{xd} x\right)\cos\left(\beta_{yd} y\right) \tag{B.5}$$

where, at cutoff, $\beta_{x0} = \pi/a$ for the $TM_{1n}$ modes and $\beta_{y0}, \beta_{yd}$ and are computed from the dispersion relations discussed previously. A plot of the *normalized* magnetic fields for the first three $TM_{1n}$ modes using *Maple* is given below in Figure B.5. Examination of the plot for the $TM_{10}$ mode in Figure B.5 reveals that the magnetic fields go through a 180 degree phase shift in the x-dimension, as x increases from zero - thus, the change in magnitude from positive to negative from the cosine function in 'x'. As the fields increase in the y-dimension (from zero), because of the dielectric boundary, the gradient of the magnetic fields changes sign (e.g. from positive to negative). This is consistent with equations B.4 and B.5 for the $TM_{10}$ modal solution. Another interesting note is that the arguments for the cosine functions in $y$ for the first two cutoff frequencies are complex. This results in an exponential function that is real.

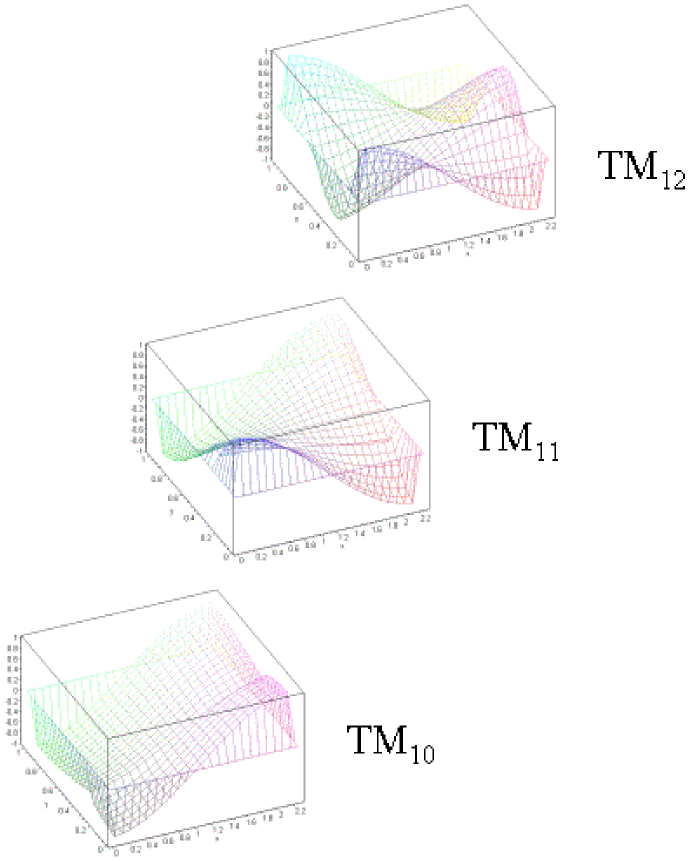


Figure B.5: Surface plots of magnetic fields for first three $TM^y_{1n}$ modes using analytical based code.

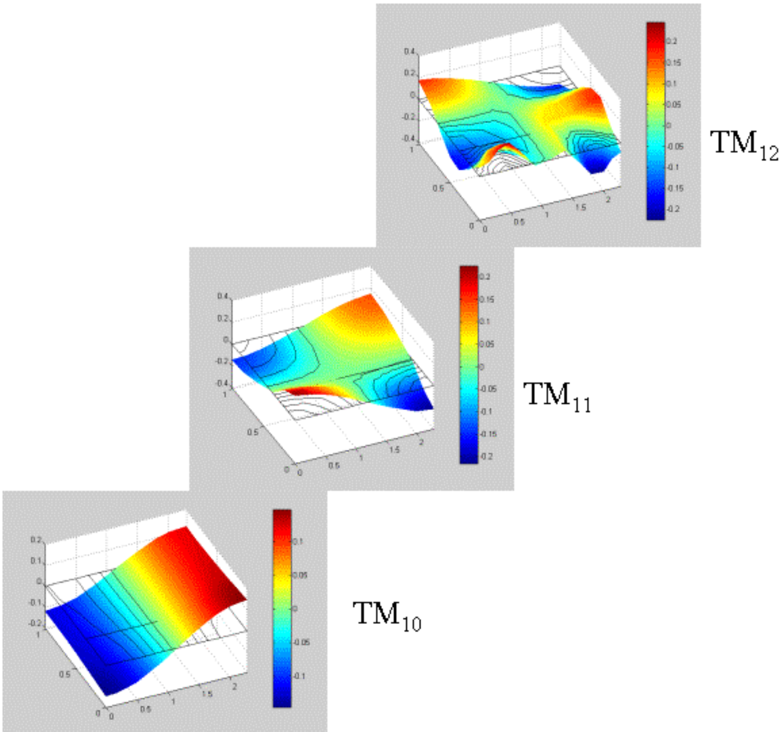


Figure B.6: Surface plots of magnetic fields at cutoff for the first three $TM_{1n}$ modes using numerical based code.

#### B.1.2.1 Numerical Method for Computing Cutoff Frequencies

The setup of the finite element problem is similar to that described in section 2.2 for the computation of the wave numbers for the inhomogeneous waveguide with the exception that the off diagonal matrix elements are zero (e.g. the $W$ elements are zero). This simplifies the computations considerably. The results of the computations of a the first three cutoff frequencies are compared in Table B.2 with those in [6]. Note that very good agreement is achieved as compared to the results documented in Balanis [6]. As expected, the results become more accurate with

Table B.2: Computation of first three cutoff frequencies $f_c$ for $TM^y_{1n}$ waveguide modes.

| Modes | $f_c$ Balanis | $f_c$ Matlab Code | $f_c$ FEM (36 elm) | $f_c$ FEM (144 elm) |
|---|---|---|---|---|
| $TM_{10}$ | 5.79 | 5.79 | 5.87 | 5.81 |
| $TM_{11}$ | 13.68 | 13.67 | 14.73 | 13.96 |
| $TM_{12}$ | 24.75 | 24.72 | 27.8 | 25.81 |

an increase in the number of finite elements used in the solution. We next examine the field plots using the numerical results. A finite element code set was developed to solve for both the cutoff frequencies and the field plots for the solution of the inhomogeneous waveguide. Figure B.6 shows magnetic field plots of the first three cutoff modes. Note the similarity in the field solutions as compared with the analytical results from Figure B.5. The numerical results of the field plots show the same trends as the analytical results; the sinusoidal nature of the fields in the $y$ direction increase with an increase in the cutoff mode. Also note the contours of the fields shown in the $z = 0$ plane which help to illustrate the gradient changes in the field plots.

### B.1.3 In-Homogeneous Waveguide: Dispersion Analysis

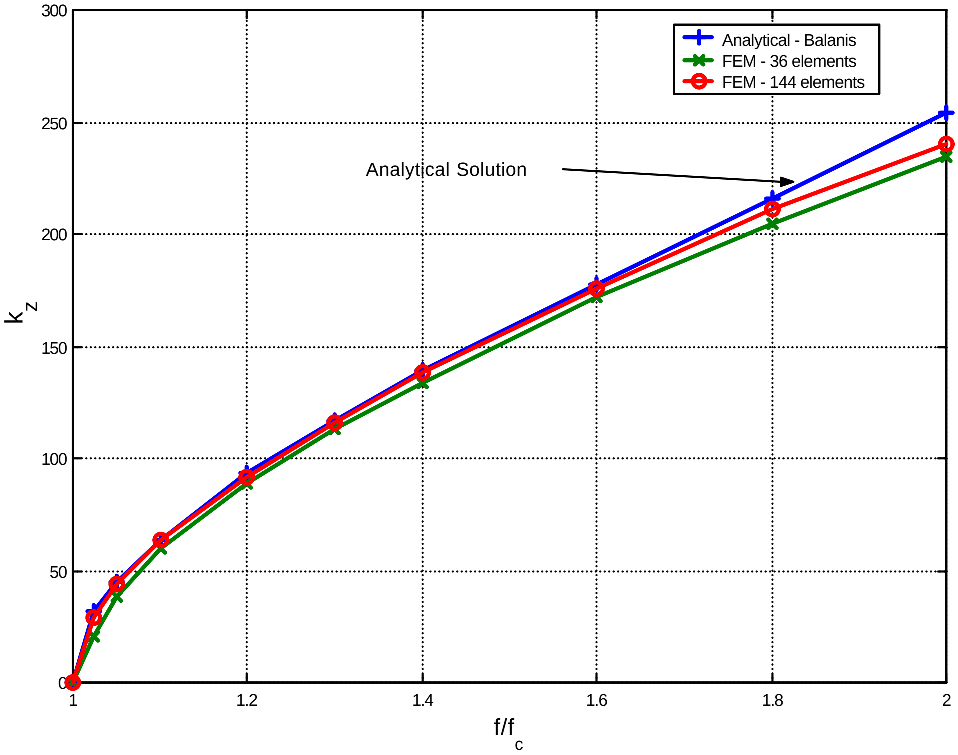


Figure B.7: Dispersion curves for $TM_{10}$ mode for partially filled waveguide.

For the in-homogeneous partially-filled waveguide described in the previous section we now compute the wavevector $k_z$ for a particular mode and determine how it correlates with the results in Balanis [6] for the same construction. The code to compute the dispersion effects for this waveguide is slightly modified from the code in the previous section B.1.2. For the full dispersion analysis, the diagonal elements are no longer zero; thus, an additional subroutine to compute the matrices for this portion of the PDE is required. A subroutine assembles the boundary elements for the waveguide.

The method for determining the frequency and corresponding wavevector for the particular mode of interest is somewhat tedious, as discussed in [9]. It requires examination of the fields for each particular mode and then examining the associated frequency, phase velocity, and wavevector which makes up that particular mode. The procedure is to vary the phase velocity $v_p$, compute the eigenvalues or *frequencies* from the phase velocity, and plot the fields for each eigenvalue found. For the correct eigenvalue and associated wavevector, the fields should agree reasonably well with the field plots for the given mode at cutoff. In this case, the fields associated with the $TM_{10}$ mode. It is clear that the fields will change somewhat with changing frequency - even for a given mode. Fortunately, the solutions to the eigenvalues are fairly discrete in the given problem and determining which mode and which eigenvalue is relatively straightforward. Figures B.5 and B.6 act as references for the particular field plots of interest when examining the field solutions for the given eigenvalues.

Table B.3 shows the results for the lowest order $TM_{10}$ mode using two different mesh sizes. The data is presented with normalized frequency $f/f_c$ - as in Balanis [6, Figure 8-15] - and the phase velocity $v_p$ at the given frequency. The results are compared against the analytical solution in Balanis using a simple Maple program that solved the transcendental equation for this mode. Once the *Dirichlet* boundary conditions were inserted into the program, determining the proper eigenvalues for the dispersion characteristics was very straightforward. The results using two different mesh sizes were very close to each other. The numerical results also matched up very well with the analytical results up to the higher $k_z$ values as evident in Figure B.7. The analytical data presented in *Balanis* was virtually identical to the Maple analytical solution shown in the Figure B.7. The slight discrepancy between the numerical data for the higher wavevector values at the higher

Table B.3: Comparison of Wave-numbers $k_z$ for partially filled dielectric waveguide.

| $f/f_c$ | $k_z$ [6] | $k_z$ 36 Elements | $k_z$ 144 elements | $\approx v_p 10^8 m/s$ |
|---|---|---|---|---|
| 1.0 | 0 | 0 | 0 | $> 10^3$ |
| 1.025 | 32 | 21 | 29 | 13 |
| 1.05 | 45 | 38 | 44 | 9.0 |
| 1.1 | 64 | 60 | 64 | 6.5 |
| 1.2 | 93 | 89 | 92 | 4.7 |
| 1.3 | 117 | 113 | 116 | 4.1 |
| 1.4 | 139 | 134 | 138 | 3.7 |
| 1.6 | 178 | 172 | 176 | 3.3 |
| 1.8 | 216 | 205 | 211 | 3.10 |
| 2.0 | 254 | 235 | 240 | 3.03 |

normalized frequencies is speculated to be due to numerical error. The last column in Table B.3 shows that the phase velocity is tending towards the speed of light in the air region. This problem was pointed out in Czendes [9] as well. Numerically, this means that the matrix coefficient in equation 2.49 tends to become very large and thus may increase the numerical error. However, as the number of elements increase, this error tends to be less as may be seen in the differences in columns 3 and 4 in Table B.3. Overall the numerical error appears to be acceptable.

# Bibliography


[1] R. Ahmad and M. H. Capstick. Efficient Equalization of Signal Shaping Filters. In *High Frequency Postgraduate Student Colloquium*, pages 23–26, February 1996. 1.4.1

[2] S. Ahmed and P. Daly. Finite Element Methods for Inhomogeneous Waveguides. In *IEE Proceedings*, volume 116, pages 1661–1664, October 1969. 1.5, 2.2.2, 2.3, 5

[3] H. A. Atwater. Tests of Microstrip Dispersion Formulas. In *IEEE Transactions on Microwave Theory and Techniques*, volume 36, pages 619–621, March 1988. 1.4.1

[4] J. S. Bagby, C. H. Lee, D. P. Nyquist, and Y. Yuan. Identification of Propagation Regimes on Integrated Microstrip Transmission Lines. In *IEEE Transactions on Microwave Theory and Techniques*, volume 41, pages 1887–1893, November 1993. 2.5.2.2

[5] M. E. Baginski, L. S. Riggs, F. J. German, and G. W. J. Jr. Finite Element Analysis of Microstrip Systems in the Vicinity of a Substrate Edge and Approximate Formulas for Capacitance. In *IEEE Transactions on Electomagnetic Compatibility*, volume 36, pages 404–408, November 1994. 1.5

[6] C. A. Balanis. *Advanced Engineering Electromagnetics*. John Wiley and Sons, New York, first edition, 1989. 1.4.3.1, 1.5, 2.4.1, 2.5, B.1.1, B.1.2, B.1.2, B.1.2, B.1.2.1, B.1.3, B.3

[7] V. Betz and R. Mittra. A Boundary Condition to Absorb Both Propagating and Evanescent Waves in a Finite-Difference Time Domain Simulation. In *IEEE Microwave and Guided Wave Letters*, volume 3, pages 182–184, June 1993. 1.5

[8] V. J. Brankovic, D. V. Krupezevic, and F. Arndt. An Efficient Two-Dimensional Graded Mesh Finite-Difference Time-Domain Algorithm for Shielded or Open Waveguide Structures. In *IEEE Transactions on Microwave Theory and Techniques*, volume 40, pages 2272–2277, December 1992. 1.5

[9] Z. J. Csendes and P. Silvester. Numerical Solution of Dielectric Loaded Waveguides:I - Finite-Element Analysis. In *IEEE Transactions on Microwave Theory and Techniques*, volume 18, pages 1124–1131, December 1970. 1.5, 2.2.1, 2.2.1, 2.2.1, 2.2.2, 2.2.2.1, 2.3, 2.3, 4.3.2.1, 5, B.1.3, B.1.3

[10] T. Edwards. *Foundations for Microstrip Circuit Design*. John Wiley and Sons, second edition, 1992. 1.3, 1.3, 4, 1.4.2.1, 1.5, 2.4.1, 2.5.2.1, 2.5.2.1, 2.5.2.1

[11] T. C. Edwards and R. P. Owens. 2-18 GHz Dispersion Measurements on 10-100 ohm Microstrip Lines on Sapphire. In *IEEE Transactions on Microwave Theory and Techniques*, volume 24, pages 505–513, 1976. 1.3

[12] J. Fang. Absorbing Boundary Conditions Applied to Model Wave Propagation in Microwave Integrated-Circuits. In *IEEE Transactions on Microwave Theory and Techniques*, volume 42, pages 1506–1512, August 1994. 1.5

[13] J. Fredrick W. Byron and R. W. Fuller. *Mathematics of Classical and Quantum Physics*. Dover Publications, first edition, 1992. A.1.1.2

[14] F. Gardiol. *Microstrip Circuits*. John Wiley and Sons, second edition, 1994. 1.4.2.2

[15] W. J. Getsinger. Microstrip Dispersion Model. In *IEEE Transactions on Microwave Theory and Techniques*, volume 21, pages 34–39, 1973. 1.3

[16] J. M. Gil and J. Zapata. Efficient Singular Element for Finite Element Analysis of Quasi-TEM Transmission Lines and Waveguides with Sharp Metal Edges. In *IEEE Transactions on Microwave Theory and Techniques*, volume 42, pages 92–98, January 1994. 1.5

[17] S. Hall, T. Liang, H. Heck, and D. Shykind. Modeling Requirements for Transmission Lines in Multi-Gigabit Systems. In *Electrical Performance of Electronic Packaging*, pages 67–70, 2004. 1.4.1

[18] M. Hano. Finite Element Analysis of Dielectric Loaded Waveguides. In *IEEE Transactions on Microwave Theory and Techniques*, volume 32, pages 1275–1279, October 1984. 1.5

[19] M. W. Jawitz. *Printed Circuit Board Materials Handbook*. McGraw-Hill Book Company, second edition, 1997. 1.4.2.1, 4.2

[20] S. Kapoor and J. B. Schneider. Characterization of Microstrip Discontinuities Using Conformal Mapping and the Finite Difference Time-Domain Method. In *IEEE Transactions on Microwave Theory and Techniques*, volume 43, pages 2636–2639, November 1995. 1.5

[21] M. Kirschning and R. Jansen. Accurate Wide-Range Design Equations for the Frequency-Dependent Characteristic of Parallel Coupled Microstrip Lines. In *IEEE Transactions on Microwave Theory and Techniques*, volume 32, pages 83–90, 1984. 1.3, 2.5.2.1

[22] J. L. Knighten, N. W. Smith, J. Fan, and J. T. D. II. Common-Mode Current Harmonics on Differential Pair Cable Shields Operating in a Regime as High as 2.125 Gb/s. In *IEEE International Symposium on Electromagnetic Compatibility*, volume 1, pages 47–51, 2001. 1.4.2.2

[23] M. Kobayashi. Frequency Dependent Characteristics of Microstrips on Anisotropic Substrates. In *IEEE Transactions on Microwave Theory and Techniques*, volume 30, pages 2054–2057, 1982. 1.3

[24] M. Y. Koledintseva, J. Wu, H. Zhang, J. L. Drewniak, and K. N. Rozanov. Representation of Permittivity for Mulitiphase Dielectric Mixtures in FDTD Modeling. In *IEEE International Symposium on Electromagnetic Compatibility*, volume 1, pages 309–304, August 2004. 3.3

[25] B. Kwark, D. S. Ma, H. Seo, K. Ham, and M. S. Park. Low Cost ALGaAs/GaAs HBT Multi-Gigabit Limiting Amplifier Packaged with a New Plastic Air Tight Cavity Encapsulation Process. In *IEEE Transactions on Components, Packaging, and Manufacturing Technology*, volume 21, pages 309–313, August 1998. 1.4.1

[26] C. T. Lee and M. L. Wu. Combination of Conformal Mapping and Finite-Difference Methods for Analysis of Supported Coplanar Waveguides. In *Microwave and Optical Technology Letters*, volume 15, pages 273–277, August 1997. 1.5

[27] J. F. Lee, R. Palandech, and R. Mittra. Modeling Three-Dimensional Discontinuities in Waveguides Using Non-Orthogonal FDTD Algorithm. In *IEEE Transactions on Microwave Theory and Techniques*, volume 40, pages 346–352, February 1992. 1.5

[28] Y. C. Leong and S. Weinreb. Novel Technique of Phase Velocity Equalization for Microstrip Coupled-Line Phase Shifters. In *High Frequency Postgraduate Student Colloquium*, pages 1453–1456, June 2000. 1.4.1

[29] MathWorks. *Partial Differential Equation Toolbox - User's Guide*, first edition, February 1996. A.1.1, A.1.1.2, A.1.1.2

[30] F. Mesa and M. Horno. Application of the Spectral Domain Method for the Study of Surface Slow Waves in Nonreciprocal Planar Structures with a Multilayered Gyroelectric Substrate. In *IEE Proceedings on Microwaves, Antennas and Propagation*, volume 140, pages 193–200, June 1993. 1.4.1

[31] G. Mur. Absorbing Boundary Conditions for the Finite-Difference Approximation of the Time-Domain Electromagnetic-Field Equations. In *IEEE Transactions on Microwave Theory and Techniques*, volume 23, pages 377–382, November 1981. 1.5

[32] G. W. Pan, D. H. Cheng, and B. K. Gilbert. 2D FDTD Modeling of objects with Curved Boundaries, Using Embedded Boundary Orthogonal Grids. In *IEE Proc, Microwave Attennas Propagation*, volume 147, pages 399–405, October 2000. 1.5

[33] C. Pelard, E. Gebara, A. J. Kim, M. G. Vrazel, F. Bien, Y. Hur, M. Maeng, S. Chandramouli, C. Chun, S. Bajekal, S. E. Ralph, B. Schmukler, V. M. Hietala, and J. Laskar. Realization of Multigigabit Channel Equalization and Crosstalk Cancellation Integrated Circuits. In *IEEE Journal of Solid-State Circuits*, pages 1659–1670, October 2004. 1.4.1

[34] I. P. Polichronakis and S. S. Kouris. Higher Order Modes in Suspended Substrate Microstrip Lines. In *IEEE Transactions on Microwave Theory and Techniques*, volume 41, pages 1449–1454, August 1993. 2.4.1

[35] C. Pozrikidis. *Numerical Computation in Science and Engineering.* Oxford University Press, first edition, 1998. 2.2.3

[36] C. Pozrikidis. *A Practical Introduction to the Finite-Element Method with Matlab.* University of California San Diego, draft edition, 2003. 2.4.2.2

[37] P. Pramanick and P. Bhartia. An Accurate Description of Dispersion in Microstrip. In *Microwave Journal*, volume 0, pages 89–96, 1983. 1.3

[38] C. Railton and J. P. McGeehan. Analysis of Microstrip Discontinuities Using the Finite Difference Time Domain Technique. In *IEEE MTT-S Digest*, pages 1009–1012, 1989. 1.5

[39] C. Railton and J. P. McGeehan. An Analysis of Microstrip with Rectangular and Trapezoidal Conductor Cross-Sections. In *IEEE Transactions on Microwave Theory and Techniques*, volume 38, pages 1017–1022, August 1990. 1.5

[40] C. Railton and J. P. McGeehan. Characterization of Microstrip Open-End with Rectangular and Trapezoidal Cross-Section. In *IEEE Electronic Letters*, volume 26, pages 685–687, May 1990. 1.5

[41] C. Railton, D. B. Shorthouse, and J. P. McGeehan. Modelling of Narrow Microstrip Lines Using Finite Difference Time Domain Method. In *IEEE Electronic Letters*, volume 28, pages 1168–1170, June 1992. 1.5

[42] C. J. Railton, E. M. Daniel, D. L. Paul, and J. P. McGeehan. Optimized Absorbing Boundary Conditions for the Analysis of Planar Circuits Using the Finite Difference Time Domain Method. In *IEEE Transactions on Microwave Theory and Techniques*, volume 41, pages 290–297, February 1993. 1.5

[43] S. Ramo, J. R. Whinnery, and T. V. Duzer. *Fields and Waves in Communication Electronics*. John Wiley and Sons, New York, second edition, 1984. 1.4.2.2, 1.4.2.3, 1.4.2.3, 3.2.1

[44] J. N. Reddy. *An Introduction to The Finite Element Method*. McGraw-Hill Book Company, first edition, 1984. 2.2.2, 2.3

[45] A. E. Ros and D. Pompei. Improvement of Performances of Microstrip Structures by Equalization of Phase Velocities. In *Microwave Symposium Digest*, volume 78, pages 41–43, June 1978. 1.4.1

[46] J. Ruppert. A Delaunay Refinement Algorithm for Quality 2-Dimensional Mesh Generation. In *Nasa Ames Research Center*, volume n/a, page n/a, n/a 1995. 1.5, 2.4.2.1

[47] M. N. Sadiku. *Numerical Techniques in Electromagnetics*. CRC, first edition, 1992. 1.5, 2.2.1, 2.2.2.1, 2.2.2.1, 2.3, 4.3.2.1, A.1.1.1, A.1.1.2, A.1.1.2, 4, B.1.1

[48] M. Salazar-Palma, T. K. Sarkar, L.-E. Garcia-Castillo, T. Roy, and A. Djordjevic. *Iterative and Self-Adaptive Finite-Elements in Electromagnetic Modeling*. Artech House, first edition, 1998. 2.2.1

[49] B. C. So, W. S. Hwang, and S. W. Kim. A Multi-Gigabit CMOS Serial Link Transceiver Using Jitter Tolerant Delay Locked Loop. In *IEEE Journal of Solid-State Circuits*, pages 171–174, December 2003. 1.4.1

[50] D. M. Sullivan. *Electromagnetic Simulation Using the FDTD Method*. IEEE Press, first edition, 2000. 1.5

[51] K. K. Thornber. High-Frequency, Transient Response of Microstrip Lines. In *IEEE Transactions on Electron Devices*, volume 37, pages 1763–1770, July 1990. 1.4.1

[52] D. Velickovic, B. Milovanovic, and Z. Mancic. New Approach for Equalizing Phase Velocities in Coupled Microstrip Lines. In *Electronic Letters*, volume 33, pages 1444–1445, August 1997. 1.4.1

[53] K. Vichienchom, M. Clements, and W. Liu. A Multi-Gigabit CMOS Data Recovery Circuit Using an Analog Parallel Sampling Technique. In *IEEE International Symposium on Circuits and Systems*, volume 4, pages 238–241, May 2001. 1.4.1

[54] Vitesse Semiconductor. G52162 Rev. 2.8 VSC7146 2.5 Gb/s Serial Transceiver Data Sheet. http://www.vitesse.com/products/www.vitesse.com, 2002. 1.4.2

[55] R. Wharton and G. Rodrigue. A Dominant Mode Analysis of Microstrip. In *IEEE Transactions on Microwave Theory and Techniques*, volume 0, pages 552–555, 1972. (document), 1.5, 2.5.1, 2.4, 2.5.1, 2.6

[56] E. Yamashita, K. Atsuki, and T. Ueda. An approximate dispersion formula of microstrip lines for computer aided design of microwave integrated circuits. In *IEEE Transactions on Microwave Theory and Techniques*, volume 27, pages 1036–1038, 1979. 1.3, 2.5.2.1

[57] R. A. York and R. C. Compton. Experimental Evaluation of Existing CAD Models for Microstrip Dispersion. In *IEEE Transactions on Microwave Theory and Techniques*, volume 38, pages 327–328, March 1990. 1.4.1